Fracture of Materials Undergoing Solid-Solid Phase Transformation.

Thesis by

Bharat Penmecha

In Partial Fulfilment of the Requirements

for the Degree of

Doctor of Philosophy

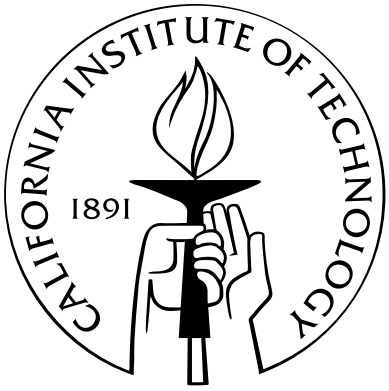

California Institute of Technology

Pasadena, California

2013

(Defended May 20, 2013)

To my parents

Acknowledgements

I couldn't thank Kaushik enough for believing in me and giving me an opportunity to work with him. It has been quite a journey since the summer of 2008 and I wouldn't have achieved whatever I have in my PhD without his unconditional support. I thank him most for giving me the room to explore and learn on my own and develop my research aptitude. His positive visage, emphasis on seeking insight without getting lost in finer details and boldness in looking at traditional ideas from a fresh perspective will stay with me for the rest of my life. I thank Prof. G. Ravichandran for all the advice and support he has extended over the years, especially for offering me support through Teaching Assistantship for Ae/ME 102 over many terms and serving on my thesis committee. I thank Prof. Michael Ortiz for agreeing to serve as my committee chair and offering feedback on my thesis. He has been a great source of inspiration for pursuing Mechanics. I thank Prof. Dennis Kochmann for serving on my committee and sharing his experience.

I have had some great colleagues at Caltech. I should start by thanking Dr. Phanish Suryanarayana, my office mate for three years for being the go-to guy on many a topic. It has been a wonderful experience to interact with the members of Kaushik's and Ravi's groups over the years - Andrew Richards, Dr. Zubaer Hossain, Dr. Saurabh Puri, Srivatsan Hulikal, Ha Jiang, Cindy Wang, Dr. Pierluigi Cesana, Farshid Roumi, Chris Kovalchik, Justin Brown, Jacob Notbohm, Aaron Stebner and Aaaron Albretch.

Life in the Thomas building has been made much easier and pleasant through the help of our wonderful administrative assistants who had it all covered on numerous occasions. I thank Leslie Ricoh, Chris Silva, Cheryl Geer, Carolina Oseguera, Lynn Seymour, Sylvie Gertmanian, Maria Koeper for all the help they have extended. I have had a wonderful time at ISP over the years. Its the people there - Laura Flower Kim, Daniel Yoder, Jim

Endrizzi - who make it special.

I have had the pleasure of making many friends outside work at Caltech which made the place even more special. I am lucky to have had some great room-mates - Prakhar Mehrotra, Navneet Narayanan, Ajay B.H, Manav Malhotra - during my memorable stay in the Catalina apartments. Nakul Reddy, Raviteja Sukhavasi, Naresh Satyan, Vahe Gabuchian, Jayakrishnan Unnikrishnan, Rangoli Sharan, Kaushik Sengupta, Dr. Sujit Nair have been great company.

I extend my gratitude to Amith Pinapala, my closest friend of many years, whose guidance and friendship has helped me steer through difficult times. I much appreciate him pointing me in a sensible direction whenever I was at a crossroads.

Special thanks to Piya Pal who has been a significant part of my life in the last few years for all the care, support and inspiration. She is a very special human being and I am grateful to destiny for making her a part of my life.

Above all I acknowledge the love, support and patience of my parents, grand parents and brother who have always given me the best. They will always be my biggest role-models for all the virtues they embody.

Abstract

A large number of technologically important materials undergo solid-solid phase transformations. Examples range from Ferroelectrics (transducers and memory devices), zirconia (Thermal Barrier Coatings) to nickel superalloys and (lithium) iron phosphate (Li-ion batteries). These transformations involve a change in the crystal structure either through diffusion of species or local rearrangement of atoms. This change of crystal structure leads to a macroscopic change of shape or volume or both and results in internal stresses during the transformation. In certain situations this stress field gives rise to cracks (tin, iron phosphate etc.) which continue to propagate as the transformation front traverses the material. In other materials the transformation modifies the stress field around cracks and effects crack growth behaviour (zirconia, ferroelectrics). These observations serve as our motivation to study cracks in solids undergoing phase transformations. Understanding these effects will help in improving the mechanical reliability of the devices employing these materials.

In this thesis we present work on two problems concerning the interplay between cracks and phase transformations. First, we consider the directional growth of a set of parallel edge cracks due to a solid-solid transformation. Assuming uniform material properties, we start by establishing a relationship between state of the stress jump due to the transformation and the resulting morphology of cracks expected. We focus on the case where the stress state due to a transformation initiating at the free edge of the specimen leads to the formation of parallel edge cracks. Subsequently, the problem is set up by invoking the dissipation principle and deriving the expressions for the driving forces. Assuming rate independent kinetic laws for cracks and the phase boundary propagation we study the interaction between the system of cracks and the phase boundary as it traverses across the geometry. The presence of the cracks doesn't effect the overall propagation of the phase boundary and

only distorts it from its mean straight shape. We then consider the stability of the parallel system of cracks against period doubling instability commonly seen in thermal cracking. After performing a linear stability analysis we conclude that the system of cracks is stable against this bifurcation. We go on to ascertain this conclusion by performing numerical simulations using finite elements. Finally, using arguments based on energy balance we derive an optimal spacing for the parallel system of cracks. From this analysis the following picture of crack growth emerges - for a given transformation strain parallel cracks initiate and assume a uniform spacing after a transient stage, grow all the way till their tips cross over the phase boundary and continue to grow as the phase boundary propagates at a uniform spacing without any instabilities.

Second, we model the effect of the semiconducting nature and dopants on fracture in ferroelectric perovskite materials, particularly barium titanate ($BaTiO_3$). Traditional approaches to model fracture in these materials have treated them as insulators. In reality, they are wide bandgap semiconductors with oxygen vacancies and trace impurities acting as dopants. We incorporate the space charge arising due the semiconducting effect and dopant ionization in a phase field model for the ferroelectric. We derive the governing equations by invoking the dissipation inequality over a ferroelectric domain containing a crack. This approach also yields the driving force acting on the crack. Our phase field simulations of polarization domain evolution around a crack show the accumulation of electronic charge on the crack surface making it more permeable than was previously believed so, as seen in recent experiments. We also discuss the effect the space charge has on domain formation and the crack driving force.

Contents

Acknowledgements iv

Abstract vi

1 Introduction 1

1.1 Solid-solid phase transformations . . . 1

1.2 Fracture and phase transformations . . . 2

1.3 Organization . . . 3

2 Directional Edge Crack Growth Due to a Phase Transformation 7

2.1 Introduction . . . 7

2.2 Overall setting . . . 11

2.2.1 Dissipation inequality and equilibrium . . . 11

2.2.2 Propagation laws . . . 14

2.2.3 Stability of a propagating system of cracks . . . 15

2.3 Stress analysis . . . 16

2.3.1 Stress due to a phase boundary . . . 16

2.3.2 Stress due to the interaction of cracks with a phase boundary . . . 19

2.4 Phase boundary . . . 22

2.5 Crack propagation . . . 24

2.5.1 Cracks with uniform spacing and length . . . 24

2.5.2 Stability against period doubling . . . 28

2.6 Numerical study . . . 29

2.7 Results . . . 32

2.7.1 One flaw in a unit cell . . . 32
2.7.1.1 Stationary phase boundary . . . 32
2.7.1.2 Moving phase boundary . . . 33
2.7.2 Multiple flaws in a unit cell . . . 34
2.8 Conclusions . . . 36
2.9 Future Directions . . . 36

3 Effect of Space Charges on Fracture in Ferroelectric Peroskites 38

3.1 Introduction . . . 38
3.2 Ferroelectric perovskites . . . 41
3.3 Fracture behaviour of ferroelectric perovskites . . . 44
3.3.1 Experiments on fracture of ferroeletrics . . . 45
3.3.2 Modelling and simulation . . . 47
3.4 Semiconducting nature of Ferroelectric perovskites . . . 50
3.4.1 Semiconductor physics . . . 50
3.4.2 Defects in perovskites . . . 53
3.5 Phase field model . . . 55
3.5.1 Kinematics . . . 56
3.5.2 Rate of dissipation . . . 56
3.5.3 Governing equations . . . 61
3.5.4 Crack surface boundary conditions . . . 62
3.6 Constitutive relations . . . 65
3.7 Implementation . . . 69
3.7.1 Finite element formulation . . . 72
3.8 Results . . . 75
3.8.1 No space charge, $\rho = 0$ . . . 77
3.8.2 n-type dopants . . . 78
3.8.3 p-type dopants . . . 79
3.8.4 Discussion . . . 79
3.9 One-dimensional model . . . 81

3.9.1 Results 81
3.10 Driving force on the crack : The J-integral 82
3.10.1 Results of J-integral 84
3.11 Summary and conclusions 84

A Appendices **92**

A.1 Stress field of a shallow phase boundary 92
A.2 Solution to the integral equations 94
A.3 Integral identities 97
A.4 Optimal orientation of phase boundary 98
A.5 Driving force on a phase boundary 100
A.6 Divergence free property of augmented energy momentum tensor 100
A.7 Domain integral for evaluating driving force, J 102

Bibliography **104**

List of Figures

1.1 Cubic to monoclinic transformation of Nitinol. Reproduced from [64] 2

1.2 Cracks resulting from phase transformation. (a) SEM micrographs of polished surfaces of CsH_2PO_4 above the phase transition temperature [65]. (b) SEM image of a partially delithiated $LiFePO_4$ single crystal [119].(c) Cracked single crystal $BaTiO_3$after subjecting to cyclic electric loading [16] 4

2.1 Directional crack growth seen in experiments: (a) Phase transformation induced cracks in $CsHSO_4$ [65]. (b) Parallel edge cracks in a glass plate due to a sharp thermal gradient [88]. (c) Edge cracks due to drying in a film of sol-gel [46] 8

2.2 A body with a crack and a phase boundary. 11

2.3 Geometry of the problem showing the phase boundary, free surface and cracks, and the partition into simpler problems used for stress analysis. 19

2.4 Unit cell of width $2b$ containing two cracks, chosen for the analysis 22

2.5 (a) Normalized driving force on the phase boundary due to the presence of the cracks over one unit cell containing a single crack. Negative values indicate force towards the cracks. The mean value over one unit cell is zero. (b) The equilibrium shape of the phase boundary. In both figures, we use $b = 10mm, h = h_1 = h_2 = 15mm, L = 15.2mm, 15.5mm, 16mm$. 23

2.6 The stress intensity factor experienced by the cracks of uniform length h and spacing b due to the phase transformation. (a) The variation of the stress intensity factor with crack length. The vertical dashed line indicates the position of the phase boundary ($b = 10mm, L = 15mm$). (b) The stress intensity factor for various crack-spacings ($L = 15mm$). (c) The normalized stress intensity factor for various crack-spacings ($L = 15mm$). (d) The normalized stress intensity factor for various positions of the phase boundary ($b = 10mm$). 25

2.7 Variation of the normalized stress intensity factors ($N = K/\sigma_0\sqrt{2\pi b}$) experienced by the two cracks when the length of one is varied while the that of the other is held fixed. Here, the phase boundary position is $L = 15mm$ indicated by the dotted vertical line while the crack spacing is $b = 10mm$. Crack #1 has a length $h_1 = 15.4mm$ while crack # 2 varies in the range $[14mm, 16mm]$. 28

2.8 Unitcell geometry and boundary conditions. 30

2.9 Traction-separation law with linear damage evolution. 31

2.10 Comparison between predictions of theory and numerical simulation. The red points represent the normalized critical stress intensity N_c and final crack length for various transformation strains computed numerically. The blue curve shows the normalized stress intensity as a function of normalized crack length. Note that cracks do not grow when $N_c > N\infty$ and grow to the phase boundary when $N < N_\infty$ showing consistence between theory and numerical simulation. ($b = 0.1mm, L = 0.15mm$). The cross-hair on the left indicates the initial flaw. 32

2.11 Crack growth with a moving phase boundary. Left: The crack length as a function of the phase boundary position for three different values of transformation strain (or equivalently ΔT). Right: Three snap-shots for $\varepsilon_o = 0.24\%$. ($b = 0.1mm$). 33

2.12 Crack growth with two cracks in a unit cell for varying transformation strains. (a) Three snap-shots with transformation strain of 0.16% shows neither crack grows. (b) Three snap-shots with transformation strain of 0.184% shows the one crack grows along with the phase boundary. (c) Three snap-shots with transformation strain of 0.22% shows the both cracks grow along the grows along with the phase boundary. The flaw spacing is $b = 0.1mm$ and the critical flaw spacing for crack growth at the applied strain based on N_{flaw} are: (a) ∞ (b) $0.17mm$ and (c) $0.056mm$ 34

2.13 Crack growth with four cracks in a unit cell at various transformation strains. Crack length vs interface position for (a) $\varepsilon_o = 0.16\%$ (b) $\varepsilon_o = 0.184\%$ (c) $\varepsilon_o = 0.22\%$. The flaw spacing is $b = 0.1mm$. 35

3.1 Cracks in piezoelectric actuators. (a) Multilayer actuator (b) Electric discharge 39

3.2 Perovskite structure of $BaTiO_3$ in the cubic and tetragonal state. Reproduced from [15]. 42

3.3 (a)Six variants of $BaTiO_3$. (b) Polarized light optical micrographs of domain patterns in $BaTiO_3$single crystal [16].(c) Domains of variants in a $BaTiO_3$crystal [48]. 43

3.4 Switching of $BaTiO_3$ unitcell under electromechnaical loading. Reproduced from http://www.ae.utexas.edu/ landis/Landis/Research.html. 44

3.5 Evolution of domain switching near a crack tip in poled PMN-PT(62-38) single crystal under negative electric fields. Reproduced from Jiang et.al. [51]. . . . 47

3.6 (a) Topographic image and (b) surface potential image of the indentation-pre-cracked $BaTiO_3$ single crystal. Reproduced from Sun et.al. [105]. 47

3.7 Band diagram of crystalline solids. 51

3.8 Band diagrams of extrinsic semiconductors. 52

3.9 Metal, n-type Semiconductor interface. (a) Before contact. (b) After contact showing the depletion layer and band bending. 53

3.10 Ferroelectric domain with a crack subject to tractions and external electric field. 55

3.11 Landau-Ginzburg multiwell potential, W_p. (a) Four-well structure, (b) Contour plot of the wells. 66

3.12 Variation of space charge density with electric potential at thermal equilibrium with n-type dopants, $T = 300K,\ N_d = 10^{24},\ N_a = 0, E_{fm} = -5.3eV$. 68

3.13 Variation of space charge density with electric potential at thermal equilibrium with p-type dopants, $T = 300K,\ N_a = 10^{24},\ N_d = 0, E_{fm} = -5.3eV$. 68

3.14 Mesh used for the simulations and boundary conditions. 76

3.15 Polarization evolution for $\sigma_o = 0,\ \phi_o = 0.1$. n represents the time step. . . . 86

3.16 Results for $\sigma_o = 0,\ \phi_o = 0.1$. (a) Polarization domains around the crack, (b) σ_{22}, (c) Electric potential, ϕ. 87

3.17 Results for n-type dopants at $\sigma_o = 0,\ \phi_o = 0.1,\ N_d = 10^{24}$ (a) Polarization domains around the crack, (b) σ_{22}, (c) Electric potential, ϕ, (d) Space Charge, ρ. 88

3.18 Results for p-type dopants at $\sigma_o = 0,\ \phi_o = 0.1,\ N_d = 10^{24}$. (a) Polarization domains around the crack, (b) σ_{22}, (c) electric potential, ϕ, (d) space charge, ρ. 89

3.19 Results from the 1-D model at different L. $N_d = 10^{24},\ N_a = 0$. Left columns shows $\mathbf{p}$ (blue) and ϕ (green). The right column shows ρ. 90

3.20 Variation of J with ϕ_o for different doping. $\sigma_o = 0$. 91

3.21 Variation of J with ϕ_o for different doping. $\sigma_o = 0 - 1$. 91

A.1 Geometry of perturbed interface and the sub-problems for superposition. . . 92

A.2 Notation for domain integral formulation to evaluate the driving force on a crack 103

Chapter 1

Introduction

1.1 Solid-solid phase transformations

Solid-solid transformations are phase transformations when a solid in a parent phase undergoes a transformation to another solid with a different crystal structure. A good example is the popular ferroelectric material barium titanate, $BaTiO_3$, used widely in transdcuing applications. Above its Curie temperature of, $T_c = 120^oC$, $BaTiO_3$exists in a state with a cubic unit cell. Upon cooling, the cubic unit cell transforms into tetragonal. Other popular examples are the Martensitic transformation of iron and shape memory alloys like nitinol (NiTi), transformation between iron phosphate and lithium iron phosphate upon insertion and removal of lithium ions, the protonic transformation of solid acid materials, and the transformation of zirconia.

Transformations which involve long range diffusion of species are termed diffusional. Transformations in which there is a change in lattice structure only through a local rearrangement of the species are termed diffusionless or martensitic transformations. These rearrangements are small, usually less than the interatomic distances, and the atoms maintain their relative relationships. A good example is the transformation of the popular shape memory alloy nitinol which undergoes a transformation from a cubic lattice to monoclinic, see Figure 1.1. The change in the lattice structure due to transformation is characterized by the transformation or Bain strain which represents the stress free strain of the transformed lattice of the material with respect to the parent lattice.

Solid-solid transformations have been the basis of numerous applications of technolog-

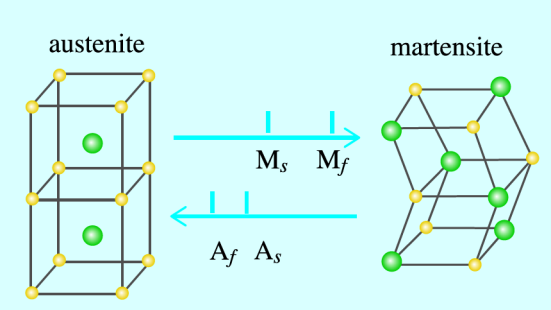

Figure 1.1: Cubic to monoclinic transformation of Nitinol. Reproduced from [64]

ical importance. The martensitic transformation of steel is responsible for producing steel of high strength. Shape memory alloys due to their superelasticty and shape memory properties have been the basis for high power density actuators in the aviation and automotive industries and numerous applications in the medical device industry ranging from dental braces to stent grafts for minimally invasive endovascular procedures. Rechargeable battery technology using lithium iron phosphate as the cathode material have been found to have greater life span, higher power density and safer to operate. This battery technology holds promise for use in hybrid vehicles and consumer electronics. Solid acid compound materials, cesium hydrogen phosphate and cesium hydrogen sulphate undergo a transformation into a phase with high proton conductivity which make them potential fuel cell electrolyte materials. Ferroelectric perovskite materials like $BaTiO_3$and PZT have long been used in sensing and actuating applications in their polar state. Through intelligent domain engineering high strain actuators are being developed which take advantage of the strain produced through domain switching.

1.2 Fracture and phase transformations

The change in the lattice structure during the transformation results in the macroscopic change in the shape or size of the transformed region. During the process, as the transformation front sweeps through a specimen, the macroscopic change in the transformed region could result in setting up internal stress. These internal stresses are typically relaxed through the formation of dislocations and twinning in ductile materials. However when the material is brittle these internal stresses lead to the formation and subsequent growth of

cracks as the transformation proceeds further.

Cracks arising out of phase transformations have been observed in several instances involving brittle materials. Figure (1.2) shows various instances where transformation leads to fracture. Cracks have been observed to initiate near the embedded electrodes in PZT multilayer piezoelectric actuators during the poling process and seen to grow subsequently ultimately leading to electric discharge. Electrodes used in Li-ion batteries have been known to develop cracks during the cyclic lithiation and de-lithiation which leads to fade in the capacity. Cycling of solid acid material, CsH_2PO_4, due to the incompatibility of transformation strain, leads to a network of microcracks which is undesirable for the functioning of the electrolyte.

Understanding the mechanics behind the growth of cracks arising out of phase transformations would help in improving the reliability of the promising technologies based on phase transforming materials. This serves as the motivation for this thesis. Typically in these materials there is other physics also at work. For example ferroelectric and piezoelectric materials involve a coupling between electrical and mechanical fields, Lithium iron phosphate based electrode involves diffusion of Li-ions , and solid acid materials involve proton transport. So the mechanics of cracks arising in these instances is coupled to the additional physics. As a result a holistic theory of the interplay between cracks and phase transformations is quite difficult to establish and so each case warrants a subjective analysis.

1.3 Organization

In this thesis we consider two problems which involve the interplay between fracture and phase transformation. First we consider the problem of directional edge crack growth arising due to a phase transformation in Chapter 2. This is motivated by observations of edge cracks arising in materials like Li-ion battery electrode particles as well as in thin films of materials having a sharp concentration or temperature gradient front which traverses along the film. The phase transformation or the sharp concentration or temperature gradient gives rise to a jump in the stress free strain across the front resulting in an internal stress which drives the cracks. Assuming uniform material properties, we start by establishing a relationship

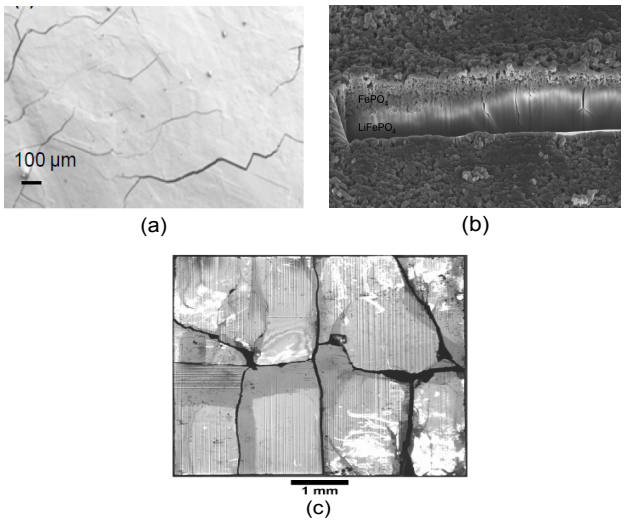

Figure 1.2: Cracks resulting from phase transformation. (a) SEM micrographs of polished surfaces of CsH_2PO_4 above the phase transition temperature [65]. (b) SEM image of a partially delithiated $LiFePO_4$ single crystal [119].(c) Cracked single crystal $BaTiO_3$after subjecting to cyclic electric loading [16]

between state of the stress jump due to the transformation and the resulting morphology of cracks expected. We focus on the case where the stress state due to a transformation initiating at the free edge of the specimen leads to the formation of parallel edge cracks. The governing equations of the models are obtained by invoking the dissipation inequality, deriving the expressions for the driving forces and assuming rate independent kinetic laws for cracks and the phase boundary propagation. We then study the interaction between the system of cracks and the phase boundary as it traverses across the geometry. We show that the presence of the cracks does not effect the overall propagation of the phase boundary and only distorts it from its mean straight shape. We then consider the stability of the parallel system of cracks against period doubling instability commonly seen in thermal cracking. After performing a linear stability analysis, we conclude that the system of cracks is stable against this bifurcation. We go on to ascertain this conclusion by performing numerical simulations using finite elements. Finally, using arguments based on energy balance, we derive an optimal spacing for the parallel system of cracks. From this analysis the following picture of crack growth emerges - for a given transformation strain parallel cracks initiate and assume a uniform spacing after a transient stage, grow all the way till their tips cross over the phase boundary and continue to grow as the phase boundary propagates at a

uniform spacing without any instabilities.

The second problem we address is the fracture of ferroelectric perovskite materials. The need to understand fracture in ferroelectrics is motivated from observations of sub critical crack growth in multilayer actuators, crack growth under a static electric field and crack growth anisotropy with poling direction. Traditional approaches to address fracture in ferroelectric perovskites have been based on linear piezoelectric fracture mechanics followed by incorporating micromechanics based constitutive laws to account for domain switching. To gain more accuracy mesoscale methods like phase field models were developed to simulate polarization domain formation around the crack tip. One of the pressing questions that needs to be addressed while performing these simulations is using physically accurate boundary conditions since the results from the simulations differ based on the boundary conditions used. The models till date also assume ferrolectric perovskites to be insulators and do not account for any space charge. However ferroelectric perovskites are wide band gap semiconductors and contain a large number of defects which act as ionized dopants. This chapter presents the first analysis that incorporates semiconducting physics and the effect of dopants while studying fracture in ferrolecetric perovskites. We do this by developing a phase field model with the traditional Ginzburg-Landau-Devonshire multiwell potential and introducing a new field variable, space charge density, ρ. We begin by deriving the governing equations through the dissipation inequality approach on a ferroelectric domain containing a crack. Along with giving us the governing equations, it also establishes the expression for the driving force on the crack. We implement the governing equations using the finite element discretization in a two dimensional square domain containing a center crack and calculate the polarization domain formation and space charge density distribution around the crack. We find that there is accumulation of electronic charge around the crack surface which leads us to believe that the crack becomes conducting. The observations from the two dimensional simulations are explained through a one-dimensional phase field model. We use the expression for the driving force derived earlier, write it in a form which is commonly used in literature and highlight its features due to the inclusion of the new variable, space charge density. Finally we evaluate the driving force on the crack in our two

dimensional simulations using a domain integral approach.

Since the two problems we study have their own rich background, we present a comprehensive introduction along with backgrounds and literature surveys in the chapters that follow.

Chapter 2

Directional Edge Crack Growth Due to a Phase Transformation

2.1 Introduction

Solid to solid phase transformations lie at the heart of a number of important technological applications. Such transformations are characterized by a change of crystal structure which manifests itself as a change of shape and volume as one phase transforms into another. Therefore, the process of transformation during which the two phases co-exist can give rise to stresses. These stresses in turn can lead to internal twinning, plasticity and incoherent interfaces, or fracture. Phase transformation induced fracture motivates the current work. Tin pest is a well-known example of such a phenomenon. Often, phase boundaries nucleate on a free surface and propagate into the body leaving a wake of fractured materials behind it. This is known as directional cracking or directional crack growth.

Directional crack growth is observed in a wide range of situations involving inhomogeneous shrinkage or expansion besides phase transformations, especially as a temperature or concentration gradient results in gradients of stress-free strain. Basalt columnar formations in solidifying and cooling lava [28], cracking in glass due to thermal shock [9] are two examples involving a temperature gradient. Cracks seen in mudflats [28], cracking of Li-ion battery anodes [38] are examples which involve concentration gradients.

One can broadly distinguish between two situations. The first is where one has a three dimensional network of cracks. Tin pest is an example of such a situation. The second is where one has a parallel array of cracks as shown in Figure 2.1 for phase transitions in

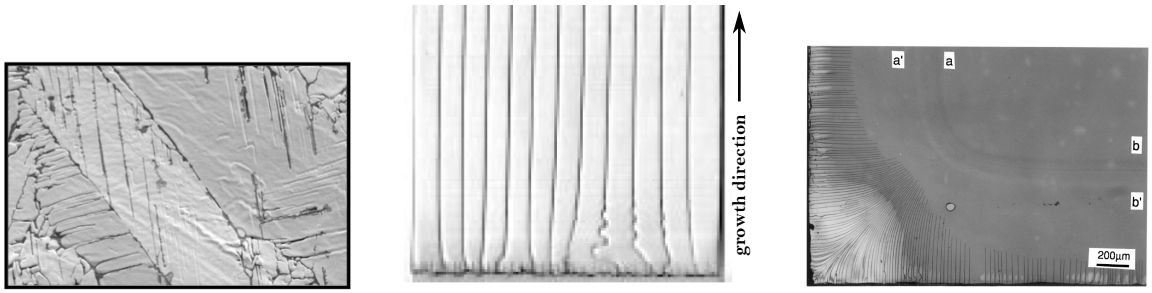

(a) (b) (c)

Figure 2.1: Directional crack growth seen in experiments: (a) Phase transformation induced cracks in $CsHSO_4$ [65]. (b) Parallel edge cracks in a glass plate due to a sharp thermal gradient [88]. (c) Edge cracks due to drying in a film of sol-gel [46]

.

$CsHSO_4$ [65], drying of aqueous sol-gel films [46], and thermal cracking of glass [88]. This can happen in both bulk ($CsHSO_4$) as well as in thin specimens (sol-gel films, glass).

Thermal cracking has motivated a number of systematic theoretical and experimental studies of directional crack growth in thin plates. In situations where the thermal gradient is small, one observes that a large number of equi-spaced cracks nucleate and propagate for some distance, but then every other crack arrests leading to a doubling of spacing. Bazant and coworkers [12, 13, 11] as well as Nemat-Nasser and coworkers [55, 73] have analysed the equilibrium and stability of a set of edge cracks growing due to a temperature gradient. Specifically, the special case of two cracks in the unit-cell of a periodic system has been considered in detail. It has been shown that at a certain depth this mode of growth is unstable with respect to period doubling. So every other crack stops growing and the rest of the cracks grow with the front. Further, at a certain point the cracks which stopped growing snap shut (i.e., are subjected to compressive stresses). The rest of the cracks keep growing and this cycle is repeated. Nemat-Nasser and collaborations [55] have extended the analysis to three cracks in the unit cell and obtain similar results. Bahr et.al [10] considered the coarsening behaviour of edge cracks observed in the thermal shock problem and the uniform spacing between tunnelling cracks seen in the directional drying of a thin layers. Using arguments based on fracture mechanics and scaling assumptions - based on the extent of unloading on the cracks in each case - they conclude that : 1) In the thermal shock case the spacing between the cracks scales with the crack length leading to a coarsening

behaviour 2) In the tunnelling cracks case the spacing scales with the film thickness and is weakly dependent of crack length.

However, no such instability is observed when the change of stress-free strain is sharp or occurs with a very high gradient. This was noted in Bazant et.al [13], where a finite element study of thermal cracks did not reveal a bifurcation for sharp temperature profiles. Shorlin et.al [97] studied shrinkage cracks that form when a thin layer of alumina/water slurry dries. A set of parallel cracks with uniform spacing form and grow in a directional manner with the sharp drying front. Once established, the spacing does not change. Allain and Limat [5] as well as Pauchard et.al [81] make similar observations with the drying of colloidal suspensions. Rosin and Perrin [88] drove a a thin glass plate at a constant velocity between two thermal baths at different temperatures, and observed stable crack growth when the velocity established a sharp gradient. They also point out the fact that the crack fronts in the middle of the plates had their tips at the same horizontal level establishing a uniform crack front.

A number of modelling approaches have been adopted to simulate the parallel crack patterns seen in thermal shock experiments [8, 40, 88] and drying films [5, 97]. Fracture mechanics combined with static crack finite element calculations were used in [73, 12, 13], the boundary element method in [10, 7], peridynamics in [56], a variational fracture approach [62] and spring network models [44]. Jagla [49] presents a theory based on energy minimization to explain the observations in thin drying layer of materials. He also presents arguments for cracks attaining a uniform spacing.

In the current work we investigate the growth of a set of parallel cracks due to a sharp change of stress-free strain caused either by a phase transformation or by a sharp gradient. We assume that the transformation strain (or jump in stress-free strain) remains essentially constant as the interface propagates. We first identify specific conditions on the transformation strain (or jump in stress-free strain) under which we expect parallel cracks. These include plane stress, but is not limited to it. There is a range of situations in bulk when only one principal strain is tensile. We then show that the presence of cracks may create local perturbations, but does not affect the overall propagation of the phase boundary. Finally we

show that cracks nucleate when the phase boundary has propagated a certain distance L_{cr} (see Figure 2.6) from the free edge. The cracks have uniform spacing $b^\star$ (see Eq. (2.5.3)), and nucleate with initial length slightly larger than $L_{\rm cr}$. Subsequently all the cracks propagate with the propagating phase boundary in such a manner that the spacing remains uniform and the tips reach just beyond the phase boundary. The choice for uniform spacing is based on the observations both in experiment [88, 82] and simulations [49, 62, 10, 56], where randomly spaced cracks, after a transient growth phase readjust the spacing between them and establish a uniform spacing either by merging with adjacent cracks or stopping to grow.

Our analysis is limited by a few important assumptions. First, we assume that the elastic modulus and fracture toughness of both phases are the same. This enables us to use superposition in our stress analysis and avoid the issues of crack propagation along the phase boundary and pinning typically associated with heterogeneous materials. The problems of cracks propagating normal to an interface separating heterogeneous media have been considered in [47]. We also assume that the modulus is isotropic. While these assumptions are reasonable in thermal/concentration gradient induced cracks, they may not be in phase transitions. Still we believe that the results we present are qualitatively meaningful. Second, we assume that the phase boundary is roughly parallel to the free edge. Again, this assumption is reasonable in thermal/concentration gradient induced cracks, it may not be in phase transitions. In the latter, the phase boundary is a very specific interface which may or may not coincide with the free edge. However, the situation analysed here constitutes the worst case scenario. Third, our analysis is limited to uniformly spaced potential cracks. Our analysis shows that there is a particular spacing that is preferred. Further, this preferred spacing is determined by the transformation strain alone, and that this spacing is stable against various instability. Therefore, we expect that the mode-II loading generated by the non-uniform spacing would result in crack deviation and merging eventually resulting in a uniform spacing.

The rest of the chapter is organized as follows. We describe the general setting and recall results from phase transitions and fracture mechanics in Section 2.2. We analyse in Section

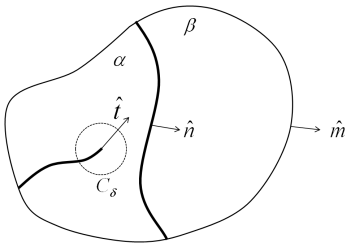

Figure 2.2: A body with a crack and a phase boundary.

2.3.1 the state of stress that can result from a phase transformation, and identify the specific conditions that cause a single tensile principal stress that in turn can lead to parallel cracks. We specialize to the problem of interest in Section 2.3.2. We consider a phase boundary roughly parallel to the free edge propagating into a solid and an array of parallel cracks perpendicular to the edge propagating into the solid in the wake of the phase boundary. Section 2.3.2 derives the resulting stresses. We study how the phase boundary propagation is affected by the cracks in Section 2.4. We show that cracks create local perturbations, but does not affect the overall propagation of the phase boundary.

The main analysis of crack propagation is presented in Section 2.5. We begin with the study of cracks of uniform spacing and length in Section 2.5.1, and then study cracks of uniform spacing but alternating length in Section 2.5.2. These allow us to draw the conclusions describe above. We confirm these conclusions through numerical simulation in Sections 2.6 and 2.7. We conclude in Section 2.8 and provide ideas for future work in Section 2.9.

2.2 Overall setting

2.2.1 Dissipation inequality and equilibrium

Consider a body Ω consisting of two phases α and β occupying complementary sub-regions Ω_α and Ω_β as shown in Figure 2.2. These phases are separated by a phase boundary $\mathcal{S}$, a smooth surface with normal $\hat{k}$. In anticipation of the situation we intend to study, we consider a crack Γ to be present in the α phase. To deal with the elastic singularity at the crack front, we remove a curved cylinder C_δ with axis following the crack front and radius

δ and consider only the region $\Omega_\delta = \Omega_\alpha \backslash C_\delta$. There is an external traction t_0 acting on a part Ω_t of the boundary of Ω, and displacement is specified on the rest of the boundary.

The total energy of the system is given by,

$$\Pi_\delta(u, \Gamma, \mathcal{S}) = \int_{\Omega_\delta} \psi_\alpha(\nabla u) dx + \int_{\Omega_\beta} \psi_\beta(\nabla u) dx - \int_{\Omega_t} t_o.u ds, \tag{2.2.1}$$

where

$$\begin{aligned} \psi_\alpha(\varepsilon) &= \frac{1}{2}(\varepsilon - \varepsilon^\star) \cdot \mathbb{C}(\varepsilon - \varepsilon^\star) + \omega, \\ \psi_\beta(\varepsilon) &= \frac{1}{2}\varepsilon \cdot \mathbb{C}, \varepsilon \end{aligned} \tag{2.2.2}$$

where $\mathbb{C}$ is the elastic modulus assumed to be uniform across the phases, $\varepsilon^\star$ is the transformation strain (stress-free strain or eigenstrain) and ω is the chemical potential. The assumption of equal elastic modulus is essential as it allows various applications of the principle of superposition in what follows. Further, we assume that this uniform modulus is isotropic and the transformation strain $\varepsilon^\star$ is diagonal (the latter is without loss of generality by a change of coordinates). We use the notation $\psi = \chi_\alpha \psi_\alpha + (1 - \chi_\alpha)\psi_\beta$, where χ_α represents the indicator function over Ω_α, to represent the elastic energy density of the body. We adopt the following notation going further, u is the particle displacement, $\mathbf{u}$ particle velocity, $\mathbf{a} = \dot{a}\hat{t}$ is the crack tip velocity, $\mathbf{v}$ is the phase boundary velocity, $v_n = \mathbf{v}.\hat{k}$ is the normal velocity of the phase boundary, $\hat{c}$ represents the normal to the curve Γ, the crack surface.

Above, we have neglected surface energy along the crack faces, and interfacial energy on phase boundary. We note that the former does not change the results since it can easily be accounted for in the crack propagation criterion. Regarding the latter, we are interested in situations where the elastic energy is significant so that the phase boundaries are almost planar.

We proceed by using the dissipaion inequality approach [4, 120] , but note that other approaches including variational[53, 61, 52] and configurational force balance [41] yield the same result. The derivation is provided for completeness. We begin by writing down the

dissipation in the body under the loading and the evolution of the phase boundary and the cracks.

$$\mathcal{D} = \mathcal{F} - \mathcal{E} \geq 0, \tag{2.2.3}$$

where F represents the rate of external work and E is the rate of change of energy of the body Ω. The rate of external work is given by

$$\mathcal{F} = \int_{\partial\Omega_t} t_o.\mathbf{u} ds, \tag{2.2.4}$$

the rate of change of energy of the body is

$$\mathcal{E} = \frac{d}{dt}\int_{\Omega_t} \psi dx. \tag{2.2.5}$$

Assuming no flux on the boundary $\partial\Omega_t$, the transport identity (A.3.3), leads to

$$\mathcal{E} = \int_{\Omega\setminus C_\delta} \dot{\psi} dx - \lim_{\delta\to 0}\int_{\partial C_\delta} \psi(\mathbf{a}.\hat{n}) ds - \int_{\mathcal{S}} [[\psi]] v_n ds. \tag{2.2.6}$$

Expanding the first term and using the divergence theorem (A.3.6) leads to

$$\begin{aligned}\mathcal{E} = &\int_{\partial\Omega_t} \frac{\partial\psi}{\partial\varepsilon}.\mathbf{u}.\hat{m} ds - \int_{\Omega_t} \nabla.\left(\frac{\partial\psi}{\partial\varepsilon}\right).\mathbf{u} dx - \lim_{\delta\to 0}\int_{\partial C_\delta}\left[\psi(\mathbf{a}.\hat{n}) + \frac{\partial\psi}{\partial\varepsilon}\mathbf{u}.\hat{n}\right] ds \\ &- \int_{\mathcal{S}} [[\psi]] v_n ds - \int_{\mathcal{S}} \left[\left[\frac{\partial\psi}{\partial\varepsilon}.\mathbf{u}\right]\right].\hat{k} ds - \int_{\Gamma}\left[\left[\frac{\partial\psi}{\partial\varepsilon}.\mathbf{u}\right]\right].\hat{c} ds.\end{aligned} \tag{2.2.7}$$

The above equation can be simplified further using the following

$$[[\alpha\beta]] = [[\alpha]]\langle\beta\rangle + [[\beta]]\langle\alpha\rangle, \qquad \sigma = \frac{\partial\psi}{\partial\varepsilon}, \tag{2.2.8a}$$

$$[[\mathbf{u}]] + v_n[[\nabla u^T]].\hat{k} = 0 \quad \text{on} \quad \mathcal{S}, \qquad \mathbf{u} = \nabla u.\mathbf{a} \quad \text{on} \quad \partial C_\delta. \tag{2.2.8b}$$

The relations in (2.2.8b) represent the compatibilty condition at the phase boundary and particle velocity on ∂C_δ. We assume that the the cylinder C_δ moves with the crack tip

velocity **a**. Substituting (2.2.8) into (2.2.7), the expression for $\mathcal{D}$ takes the form

$$\mathcal{D} = \int_{\Omega_t} \nabla.\sigma.\mathbf{u} dx + \int_{\partial\Omega_t} (t_o - \sigma.\hat{m})\, ds + \lim_{\delta\to 0} \int_{\partial C_\delta} \left[\psi(\mathbf{a}.\hat{n}) + \nabla u^T \sigma.\hat{n}.\mathbf{a}\right] ds$$
$$+ \int_{\mathcal{S}} \left([[\psi]] - [[\nabla u^T.\hat{k}]]\langle\sigma.\hat{k}\rangle \right) v_n ds + \int_{\mathcal{S}} [[\sigma.\hat{k}]]\langle\mathbf{u}\rangle ds + \int_{\Gamma} [[\sigma.\hat{c}]].\mathbf{u} ds. \tag{2.2.9}$$

Note that the terms contributing to the dissipation are arranged in conjugate pairs - generalized velocity times a conjugate force. Using the arguments presented in [22], equilibrium under isothermal conditions, assuming traction free crack faces leads to

$$\nabla\cdot\sigma = 0, \quad \sigma.\hat{m} = t_o \ \text{ on } \ \partial\Omega_t \quad [[\sigma]]\hat{k} = 0 \ \text{ on } \ \mathcal{S}, \quad \sigma = \begin{cases} \mathbb{C}(\varepsilon - \varepsilon^\star) & \text{in } \Omega_\alpha \\ \mathbb{C}\varepsilon & \text{in } \Omega_\beta \end{cases}. \tag{2.2.10}$$

2.2.2 Propagation laws

The driving forces conjugate to crack propagation and phase boundary propagation are respectively

$$d_a = \lim_{\delta\to 0} \int_{\partial C_\delta} \hat{t}\cdot(\psi I - \nabla u^T\sigma).\hat{n} ds\ , \tag{2.2.11}$$
$$d_S = \hat{k}.[[\psi I - \nabla u^T\sigma]].\hat{k} = [[\psi]] - \langle\sigma\rangle : [[\varepsilon]]. \tag{2.2.12}$$

where $\hat{t}$ is the tangent to the crack at the tip. For the energy density as in (2.2.2) and for an boundary moving into the the $\beta-$phase, the expression for the driving force reduces to

$$d_S = \langle\sigma\rangle : \varepsilon^\star - \omega, \tag{2.2.13}$$

where $\langle\sigma\rangle$ represents the mean value of the stress across the phase boundary. Thus, in the absence of stress, the α phase tends to grow when ω is negative and vice-versa. The driving force on the phase boundary (2.2.12) is the jump in the widely known Eshelby energy-momentum tensor [32]. The driving force on the crack tip (2.2.11) is the celebrated J-integral [87] and is often referred to as the energy release rate G [86].

The propagation of the cracks and the interface conditions follow the kinetic relations

$$\dot{a} = f_a(d_a) \qquad v_n = f_S(d_S), \tag{2.2.14}$$

where a is the crack length and v_n is the normal velocity of the phase boundary. We assume rate-independent kinetic relations :

$$d_a \leq G_c,\ \dot{a} = 0 \text{ if } d_a < G_c, \text{ and } \dot{a} \geq 0 \text{ if } d_a = G_c\ , \tag{2.2.15}$$

$$|d_S| \leq d_c,\ v_n = 0 \text{ if } |d_S| < d_c, \text{ and } d_S v_n \geq 0 \text{ if } |d_S| = d_c,\ . \tag{2.2.16}$$

Above, G_c is the critical energy release rate and d_c is the critical driving force for interface propagation. We also restrict $\dot{a} \geq 0$ to prevent crack healing.

2.2.3 Stability of a propagating system of cracks

Consider a loading system where two cracks propagate with a smooth time history $a_1(t)$ and $a_2(t)$ such that it satisfies the condition (cf. (2.2.15))

$$d_a^1(a_1(t), a_2(t)) = d_a^2(a_1(t), a_2(t)) = G_c. \tag{2.2.17}$$

Now assume that beginning at time $t = t^\star$, we have an alternate smooth crack history $b_1(t)$ and $b_2(t)$ with $\dot{b}_i \geq 0$ consistent with the loading and propagation criterion :

$$d_a^1(b_1(t), b_2(t)) \leq G_c,\ d_a^2(b_1(t), b_2(t)) \leq G_c. \tag{2.2.18}$$

Subtracting (2.2.18) from (2.2.17) and expanding around $t = t^\star$, we find the *necessary condition for bifurcation* to be

$$\sum_{j=1}^{2} H_{ij}(\dot{a}_j(t^\star) - \dot{b}_j(t^\star)) \geq 0 \quad i = 1, 2 \quad \text{for some } \dot{b}_i \geq 0, \tag{2.2.19}$$

where

$$H_{ij} = \left.\frac{\partial d_a^i}{\partial a_j}\right|_{(a_1(t^\star),a_2(t^\star))} . \tag{2.2.20}$$

Note that this condition is somewhat subtle since we require $\dot{a}_i, \dot{b}_i$ to be non-negative. In other words, one can have a singular Hessian H, but still be stable because the criticality occurs along inadmissible crack histories.

This analysis, consistent with those in [12] and [74], assumes that the crack paths and crack trajectories are differentiable. However we note that this may not always be the case [19] for rate-independent laws.

2.3 Stress analysis

2.3.1 Stress due to a phase boundary

We begin by studying the nature of stresses that arise as a consequence of the phase transition. This depends on the elastic moduli of the two phases, the transformation strain as well as the microstructure (i.e., the geometric arrangement of the two phases). In many structural phase transitions, the microstructure that arises is the one that minimizes the free energy of the system. This in turn is dominated by the strain energy for large enough transformation strains. The problem of computing the optimal microstructure remains open in general (see for example Chenchiah and Bhattacharya [21]). However, when both phases have the same elastic modulus as assumed in this work, Kohn [57] has shown that the optimal arrangement is laminates with a specific interface normal.

If the transformation strain is a symmetrized rank-one matrix, i.e., $\varepsilon^\star = \frac{\gamma}{2}\left(\hat{n}\otimes\hat{m} + \hat{m}\otimes\hat{n}\right)$ for some scalar γ and unit vectors $\hat{n}, \hat{m}$, then the two phases can co-exist in a stress-free manner with an interface with normal $\hat{n}$ or $\hat{m}$. If, $\varepsilon^\star$ is not of this form, then Kohn [57] has shown that the the best possible interface is one that affords the best approximation of $\varepsilon^\star$ to a symmetrized rank-one matrix. Specifically, let $\hat{n}$, $\hat{m}$ solve the variational problem:

$$\gamma = \max_{\hat{n},\hat{m}} \quad \frac{\left(\hat{n}\otimes\hat{m} + \hat{m}\otimes\hat{n}\right)\cdot\mathbb{C}\varepsilon^\star}{\left(\left(\hat{n}\otimes\hat{m} + \hat{m}\otimes\hat{n}\right)\cdot\mathbb{C}\left(\hat{n}\otimes\hat{m} + \hat{m}\otimes\hat{n}\right)\right)^{1/2}}. \tag{2.3.1}$$

Then, the interface between the two phases is either $\hat{n}$ or $\hat{m}$. Further, the jump in strain across the interface is

$$[[\varepsilon]] = \frac{\gamma}{2}\left(\hat{n}\otimes\hat{m} + \hat{m}\otimes\hat{n}\right), \tag{2.3.2}$$

so that jump in stress across the interface is

$$[[\sigma]] = \mathbb{C}\left(\frac{\gamma}{2}\left(\hat{n}\otimes\hat{m} + \hat{m}\otimes\hat{n}\right) - \varepsilon^{\star}\right). \tag{2.3.3}$$

For specificity, let us assume that the interface normal is $\hat{n}$. Then, traction continuity requires that $[[\sigma]]\hat{n} = 0$. It follows that the normal to the interface is one of the principal axes of the stress jump with principal value zero. In other words, the state of stress resulting from the phase transformation is at most biaxial along two normal directions that lie on the phase boundary.

If both of these are tensile, then we expect to see a network of cracks like in basalt and if both are compressive, we may see interfacial fracture. However, if exactly one of them is tensile, we expect to see parallel cracks of the type we analyse here. This happens exactly when the product of the two principal stresses is non-positive. However, notice that this product is also the determinant of the projection of the stress to the plane of the interface. Putting this together, we conclude that we expect to see parallel cracks when

$$\hat{n}\cdot\operatorname{cof}([[\sigma]])\hat{n} \leq 0, \tag{2.3.4}$$

where cof( ) represents the cofactor, $[[\sigma]]$ is given by (2.3.3), and $\gamma, \hat{n}, \hat{m}$ are given by (2.3.1).

To illustrate this condition, let

$$\varepsilon^{\star} = \begin{bmatrix} \varepsilon_1^* & 0 & 0 \\ 0 & \varepsilon_2^* & 0 \\ 0 & 0 & \varepsilon_3^* \end{bmatrix}. \tag{2.3.5}$$

We effectively have two situations.

- Case 1: $\varepsilon_1^* < \varepsilon_2^* < \varepsilon_3^* < 0$. An example is the $\alpha - \beta$ transformation of tin, where

the metallic, white β form of tin transforms to the brittle, grey α form upon cooling below 13.2°C. The transformation strain from α to β is characterized by $\varepsilon_1^* = \varepsilon_2^* = -0.113$, $\varepsilon_3^* = -0.0204$, [84]. Let $\hat{e}_i$, $(i = 1, 2, 3)$ denote the principal directions of ε^*. In this case, the optimal normal according to (2.3.1) is any vector in the $\hat{e}_1 - \hat{e}_2$ plane. If we choose it to be $\hat{e}_1$, then the jump in stress components is

$$[[\sigma_{22}]] = -E\frac{\varepsilon_3^* + \nu\varepsilon_2^*}{1-\nu^2}, \qquad [[\sigma_{33}]] = -E\frac{\varepsilon_2^* + \nu\varepsilon_3^*}{1-\nu^2}. \tag{2.3.6}$$

Since all the strains are negative, the stress jump has two positive principal values. One would expect a network of cracks similar to mud-cracking unless we are in plane stress.

We note that the case $0 < \varepsilon_1^* < \varepsilon_2^* < \varepsilon_3^*$ is essentially the same with the roles of the two phases and the sign of the stresses reversed.

- Case 2: $\varepsilon_1^* < \varepsilon_2^* < 0 < \varepsilon_3^*$. The intercalation phase transition in $LiFePO_4$ is an example with $\varepsilon_1^* = -0.056$, $\varepsilon_2^* = -0.0434$, $\varepsilon_3^* = 0.013$ [66]. In this case, the interface normal depends on the specific details of the transformation strain and elastic modulus. For the values of the transformation and elastic moduli for $LiFePO_4$, the normal happens to be $\hat{e}_1$, and this is in agreement with observations. Further, the jump in stress is again given by (2.3.6). It is readily verified that the jumps have opposite signs. Thus, we have only one tensile principal stress, and we anticipate the formation of parallel edge cracks as seen in [118, 38]. To analyse crack formation and growth we confine the analysis to the plane perpendicular to the crack fronts.

  We note that the case $\varepsilon_1^* < 0 < \varepsilon_2^* < \varepsilon_3^*$ is essentially the same with the roles of the two phases and the signs of the stress reversed.

In summary, we expect to see an array of parallel cracks in Case 2.

Another situation in which we expect to see an array of parallel cracks is in plane stress. When the in-plane components of transformation strain ε_1^*, ε_2^* are opposite in sign, the two phases can co-exist in a stress-free manner. However, when they are of the same sign, the phase boundary is normal to the eigenvector which corresponds to the largest (in magnitude)

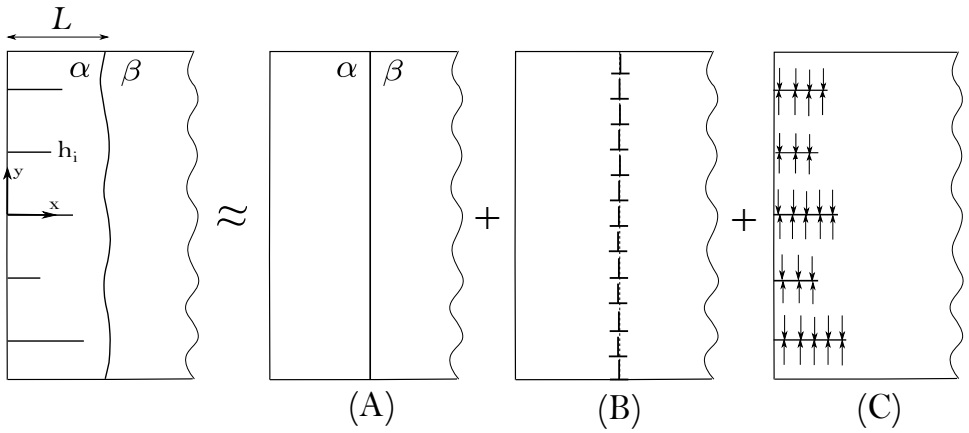

Figure 2.3: Geometry of the problem showing the phase boundary, free surface and cracks, and the partition into simpler problems used for stress analysis.

eigenvalue and the state of stress in the α phase is uniaxial. This is the situation in $LiFePO_4$ flakes often used in batteries.

2.3.2 Stress due to the interaction of cracks with a phase boundary

We now specialize to the geometry of interest and to two dimensions. We seek to address nucleation and growth of cracks when the interface is close to a free edge. This interface may represent a phase boundary as discussed in the previous section, or also a region of high gradient of temperature or concentration separating regions of uniformity. We assume that the body is stress-free far away from the free boundary (i.e., deep into the β phase). We assume that the specimen is semi-infinite, the phase boundary is broadly parallel to the free end, and a set of equi-spaced (but possible varying in length) parallel cracks run from the free edge to the phase boundary as shown in Figure 2.3. For specificity, we assume that the transformation strain is

$$\varepsilon^\star = \begin{bmatrix} -2\varepsilon_o & 0 \\ 0 & -\varepsilon_o \end{bmatrix} . \tag{2.3.7}$$

We assume for the stress analysis that the cracks are separated from the phase boundary. We further assume that the deflection of the phase boundary due to the elastic field set up by the cracks is almost straight. Under these assumptions, we can approximate the phase boundary to be straight subject to a concentrated dislocation density $B_x = -(2+\nu)\varepsilon_o f'(y)$, where ν is the Poisson's ratio, f is the normal displacement of the phase boundary from

its mean position and y is the coordinate along the mean phase boundary. We provide the details in Appendix A.1. This idea has been used before in the context of thin films [36] and has recently been proved rigorously for phase boundaries [26].

We are now able to decompose the problem into three sub-problems as shown in Figure 2.3.

A. Straight phase boundary with no cracks. For the transformation strain assumed in (2.3.7), the state of stress in a semi-infinite body which is stress-free at infinity and which contains a phase boundary at a distance L to the free edge is piecewise constant, and verified to be

$$\sigma(x) = \begin{cases} \begin{bmatrix} 0 & 0 \\ 0 & \sigma_o \end{bmatrix} & x < L \\ \\ \begin{bmatrix} 0 & 0 \\ 0 & 0 \end{bmatrix} & x > L \end{cases}, \qquad \sigma_o = \varepsilon_o E. \tag{2.3.8}$$

B. Dislocation distribution on the phase boundary. For a semi-infinite body with a concentrated dislocation density acting on a line at a distance L from the free edge, we show for the special case of a shallow cosine displacement of the phase boundary i.e. $f(y) = A\cos(\lambda y), A << \lambda$, in Appendix A.1, that the state of stress is obtained from the Airy stress potentials

$$\Phi_1 = \frac{\sigma_o A e^{-\lambda(x+L)}\{3 + \lambda L + \lambda x(5 + 2\lambda L) + e^{2\lambda x}(-3 + \lambda(x - L))\}\cos(\lambda y))}{4\lambda} \quad 0 < x < L, \tag{2.3.9a}$$

$$\Phi_2 = \frac{\sigma_o A e^{-\lambda(x+L)}\{3 + \lambda L + \lambda x(5 + 2\lambda L) - e^{2\lambda L}(3 + \lambda(x - L))\}\cos(\lambda y)}{4\lambda} \quad x > L. \tag{2.3.9b}$$

This result can be used to determine the stress field due to an arbitrary displacement $f(y)$.

C. Cracks with tractions on the crack face. Finally consider a semi-infinite body with

a number of cracks emanating from the free surface. We assume that the surface of the cracks are subjected to normal and shear tractions $\sigma(x), \tau(x)$. In order for the superposition of the three parts to provide a solution to the original problem, we take these tractions to be equal and opposite to the sum of the tractions at that location in parts A and B. Further, if we assume that the cracks are separated from the phase boundary, L is small compared to the size of the specimen and the interface displacement is shallow, we may ignore the contribution due to part B. Hence the shear is zero, and the normal traction is uniform and equal to $-\sigma_0$.

We assume that the arrangement of cracks is periodic, with n cracks in one period. The cracks are equispaced, with spacing b, but have possibly different lengths. For specificity, we specialize to the case of two cracks in one period as shown in Figure 2.4. The semi-infinite strip is subject to periodic boundary conditions on the top and bottom surfaces, the free edge is traction free, and the crack faces are subject to a normal traction $-\sigma_0$. As shown in [73], we can write the traction boundary conditions for the crack faces in terms of dislocation distributions $D_1(t)$ and $D_2(t)$ as follows:

$$\frac{\pi}{2b}\int_0^{h_1} D_1(t)G_1(t,x)dt + \frac{\pi}{2b}\int_0^{h_2} D_2(t)G_2(t,x)dt = -\sigma_o \quad 0 < x < h_1, \tag{2.3.10a}$$

$$\frac{\pi}{2b}\int_0^{h_1} D_1(t)G_2(t,x)dt + \frac{\pi}{2b}\int_0^{h_2} D_2(t)G_1(t,x)dt = -\sigma_o \quad 0 < x < h_2, \tag{2.3.10b}$$

where $G_1(x,t)$ and $G_2(t,x)$ are as follows

$$\begin{aligned} G_1(t,x) = {} & 2\coth\frac{\pi(x+t)}{2b} - \frac{\pi(x+3t)}{2b}\operatorname{cosech}^2\frac{\pi(x+t)}{2b} + \frac{xt\pi^2}{b^2}\operatorname{cosech}^2\frac{\pi(x+t)}{2b}\coth\frac{\pi(x+t)}{2b} \\ & - 2\coth\frac{\pi(x-t)}{2b} + \frac{\pi(x-t)^2}{2b}\operatorname{cosech}^2\frac{\pi(x-t)}{2b}, \end{aligned} \tag{2.3.11a}$$

$$\begin{aligned} G_2(t,x) = {} & 2\tanh\frac{\pi(x+t)}{2b} + \frac{\pi(x+3t)}{2b}\operatorname{sech}^2\frac{\pi(x+t)}{2b} - \frac{\pi^2 tx}{b^2}\operatorname{sech}^2\frac{\pi(x+t)}{2b}\tanh\frac{\pi(y+t)}{2b} \\ & - 2\tanh\frac{\pi(y-t)}{2b} - \frac{\pi(x-t)}{2b}\operatorname{sech}^2\frac{\pi(y-t)}{2b}. \end{aligned} \tag{2.3.11b}$$

Above, we have accounted for the free surface using image forces, or a distribution of climb dislocations on the free surface [35]. In order to account for the crack tip

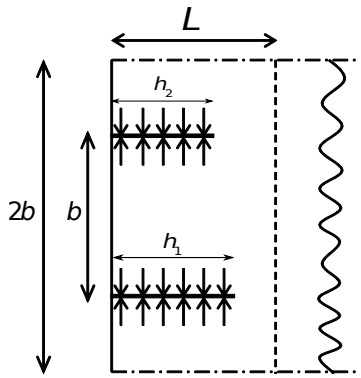

Figure 2.4: Unit cell of width $2b$ containing two cracks, chosen for the analysis

singularity we rewrite D_1 and D_2 as

$$D_1(t) = \frac{h_1}{\sqrt{h_1^2 - t^2}} C_1(t), \qquad D_2(t) = \frac{h_2}{\sqrt{h_2^2 - t^2}} C_2(t). \tag{2.3.12}$$

The integral equations are solved numerically by using Gauss-Chebyshev quadrature for C_1 and C_2. The Mode-I stress intensity factors can be expressed as

$$K_i = \lim_{x \to h_i^+} \sqrt{2\pi(x - h_i)}\sigma_{yy}(x, y = 0) = -\pi\sqrt{\pi h_i} C_i(h_i) \quad i = 1, 2. \tag{2.3.13}$$

See Appendix A.2 for further details. The values obtained were verified against those listed in literature [14].

Note that the cracks are subjected to stresses that are analogous to Mode-I loading – i.e., the stresses seek to open the crack. In this situation, the driving force d_a on the crack is related to the stress intensity factor defined in (2.3.13) as [86] :

$$d_a^i = \frac{K_i^2}{E}. \tag{2.3.14}$$

2.4 Phase boundary

In this section, we study the evolution of the phase boundary as governed by the rate independent equaton (2.2.16). We assume that we have a uniform array of equi-spaced

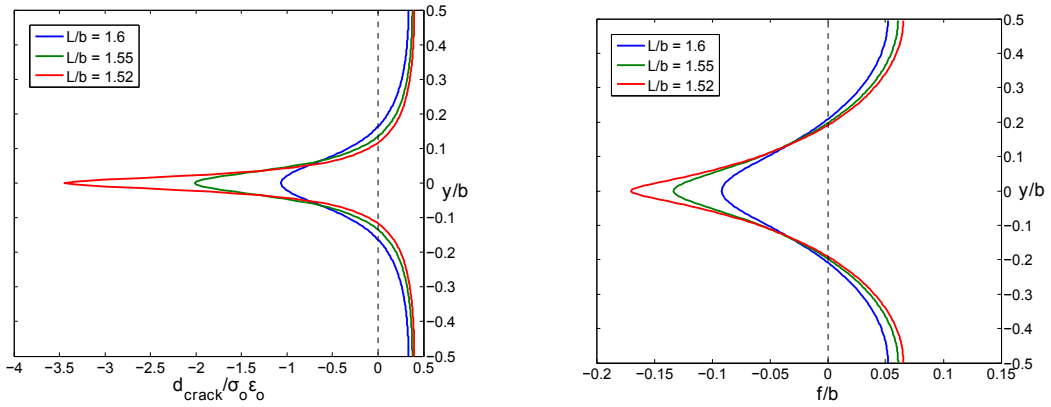

(a) (b)

Figure 2.5: (a) Normalized driving force on the phase boundary due to the presence of the cracks over one unit cell containing a single crack. Negative values indicate force towards the cracks. The mean value over one unit cell is zero. (b) The equilibrium shape of the phase boundary. In both figures, we use $b = 10mm, h = h_1 = h_2 = 15mm, L = 15.2mm, 15.5mm, 16mm$.

cracks. So we consider a unit cell containing a single crack.

We begin by examining the driving force acting on the phase boundary. This is given by (2.2.13). In light of the superposition described in Section 2.3.2, this driving force may be decomposed as

$$d_S = d_0 + d_{\text{self}} + d_{\text{crack}}, \tag{2.4.1}$$

where

$$d_0 = \left(\langle \sigma^A \rangle : \varepsilon^\star - \omega\right), \quad d_{\text{self}} = \langle \sigma^B \rangle : \varepsilon^\star, \quad d_{\text{crack}} = \sigma^C : \varepsilon^\star. \tag{2.4.2}$$

The first term is the driving force on a planar phase boundary in the absence of cracks. The second term is the driving force resulting from the non-planar nature of the phase boundary. The third is the driving forces due to the presence of cracks, and specifically due to the stress resulting from the sub-problem C. Further, since ε^* is of the form (2.3.7),

$$d_{\text{crack}} = -\varepsilon_0(2\sigma_{11}^{(C)} + \sigma_{22}^{(C)}). \tag{2.4.3}$$

Above, we omit the average symbol since the crack is distant from the phase boundary by assumption and the stress is continuous across the phase boundary. This component of the driving force is shown in Figure 2.5 (a). The crack is at $y = 0$. The phase boundary is drawn

towards the crack ahead of the crack, and pushed away from it between two cracks. This is as we expect from intuition given that the β phase is longer in the y direction compared to the α phase. We also find numerically that the mean value of this contribution to the driving force over the entire unit cell is zero. We expect from the equilibrium of the unit cell (Figure 2.4) that average value of $\sigma_{11}^{(C)}$ to be zero. We find numerically that the average of $\sigma_{22}^{(C)}$ also turns out the to be zero.

We now turn to propagation. The driving force created by the cracks tends to distort the phase boundary away from the planar shape. This leads to self-interaction which in turn depends on the shape of the phase boundary. To understand this, we study the equilibrium shape of the phase boundary under the assumption that there is no driving force on the planar boundary. In other words, we solve the equation $d_{\text{self}} + d_{\text{crack}} = 0$ for the normal distortion $x = f(y)$. A typical result is shown in Figure 2.5 (b). The driving force due to sub-problem (C) tends to distort the phase boundary while the self-energy tends to straighten it out. The overall result is a phase boundary drawn towards the crack ahead of the crack, and pushed away from it between two cracks, with mean distortion zero. Now, for an interface with this shape, $d_S = d_0$. Since d_0 is independent of shape, the driving force is uniform and according to (2.2.16), the interface propagates as long as the chemical driving force is large without any further distortion and subject to the same driving force as a straight interface.

In summary, while the cracks may potentially distort the phase boundary locally, it does not affect the overall evolution. Combined with the earlier observation that the stresses due to the distorted phase boundary decay away from it, we assume henceforth that the phase boundary propagates independent of the cracks and the cracks only see a planar phase boundary.

2.5 Crack propagation

2.5.1 Cracks with uniform spacing and length

We now turn to the cracks. We begin with a periodic arrangement of cracks of uniform spacing and uniform length. We assume that the phase boundary is at a given position L

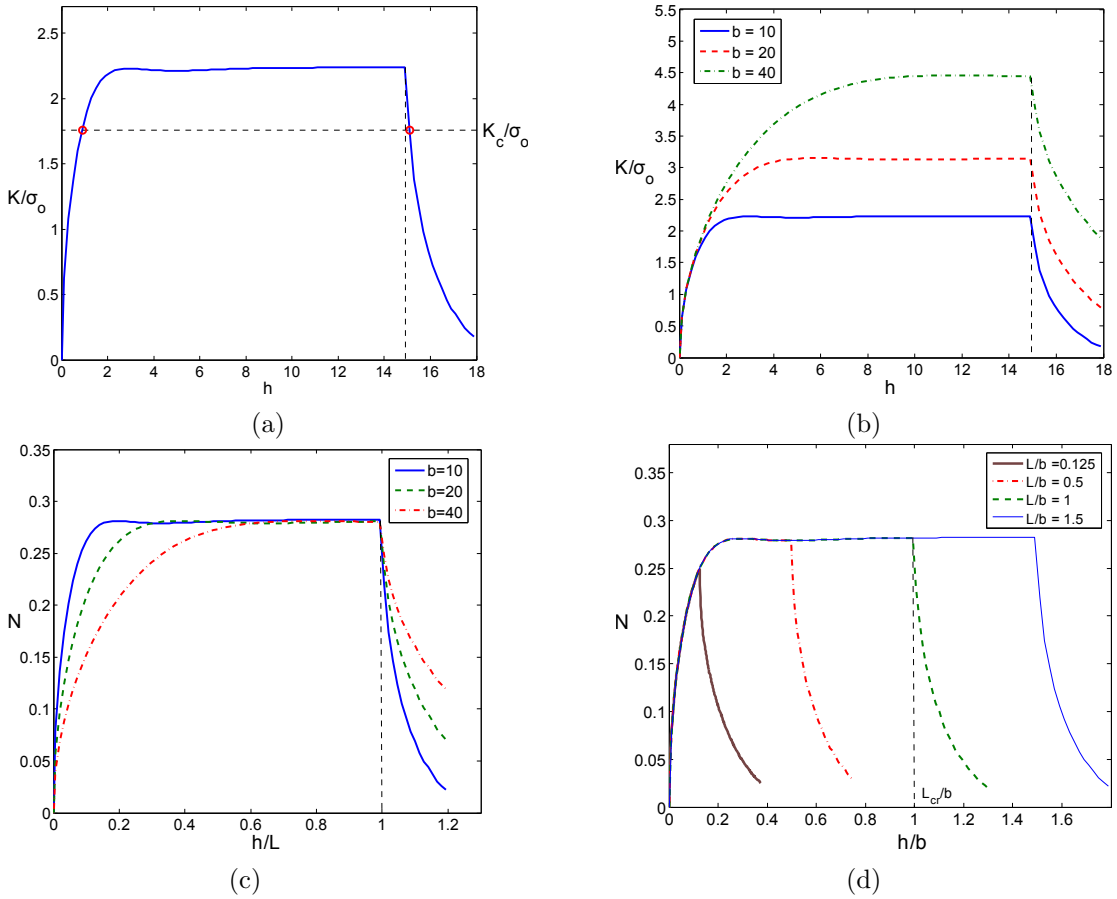

Figure 2.6: The stress intensity factor experienced by the cracks of uniform length h and spacing b due to the phase transformation. (a) The variation of the stress intensity factor with crack length. The vertical dashed line indicates the position of the phase boundary ($b = 10mm, L = 15mm$). (b) The stress intensity factor for various crack-spacings ($L = 15mm$). (c) The normalized stress intensity factor for various crack-spacings ($L = 15mm$). (d) The normalized stress intensity factor for various positions of the phase boundary ($b = 10mm$).

and examine the driving force or equivalently the stress intensity experienced by the crack. Figure 2.6(a) shows the stress intensity factor (normalized by nominal stress) as a function of crack-length for a given spacing. As anticipated, the stress intensity vanishes at zero crack length and gradually increases with crack length. The variation is similar to that of an isolated edge crack. As the crack length increases, the cracks begin to interact with each other and shield each other. So, the rate of increase of stress intensity with length decreases; eventually it peaks (at $h = 2.9mm$ with $K/\sigma_0 = 2.229\sqrt{mm}$ for $b = 10mm$). It drops slightly beyond the peak but then increases slightly again to reach a limiting value independent of crack-length ($K_\infty/\sigma_0 = 2.236\sqrt{mm}$ for $b = 10mm$). We label this the *limiting stress intensity* K_∞. We understand this limit as follows: once the cracks become long and no longer feel the presence of the free edge, they behave like a system of parallel semi-infinite cracks. The situation changes when the crack reaches the phase boundary. It drops rapidly as the state of stress changes on the other side of the phase boundary.

Figure 2.6(b) shows the stress intensity for various crack-spacing. We see that the stress intensity factor increases with increasing spacing due to reduced interaction (shielding) between the cracks. Figure 2.6(c) shows the same results in a non-dimensional fashion: $N = \frac{K}{\sigma_o\sqrt{2\pi b}}$ vs. h/L. Remarkably, note that the limiting value of the non-dimensional stress-intensity, $N_\infty = 0.282$, is independent of the crack spacing. Finally, Figure 2.6(d) shows that the (non-dimensionalized) stress-intensity vs. crack length is unaffected by the position of the phase boundary, except that it determines the point beyond which the stress intensity drops. We define the position of the phase boundary where the normalized stress intensity factor first reaches the peak value N_∞ to be L_{cr}. It occurs at $L_{\text{cr}} = b$.

Now consider a material with a fracture toughness of K_c. Our crack propagation criterion (2.2.15) is equivalent to the statement that cracks propagate when $K = K_c$. If we know the crack spacing and it is small enough, Figure 2.6(a) shows that there are two possible crack-lengths – one close to the free surface, and one slightly beyond the phase boundary*. The stability criterion (2.2.19) adopted to a single crack states that the stability is equiva-

* Note that the fact that the stress intensity has a slight peak close to the free surface means that there are possibly two additional solutions. We ignore this here since it happens for a very narrow range of toughness, these may be within the nucleation length and further, a perturbation would destabilize it. This is reinforced by our numerical simulations.

lent to requiring that the stress-intensity factor decreases with increasing crack-length (also [73]). Thus, the stable crack position is the one slightly beyond the phase boundary. Since the limiting stress intensity factor is independent of crack length and phase boundary position, we obtain a simple criterion for crack propagation with a fixed spacing: parallel cracks propagate uniformly when $K_\infty = K_c$ or equivalently $N_\infty = N_c$ where

$$N_c = \frac{K_c}{\sigma_0\sqrt{2\pi b^\star}}. \tag{2.5.1}$$

In other words, the *critical transformation strain* $\varepsilon_0^\star$ for cracks to propagate with the phase boundary at spacing b is

$$\varepsilon_0^\star = \sqrt{6.28\frac{K_c^2}{\pi E^2 b}}, \tag{2.5.2}$$

for cracks to propagate with the phase boundary at spacing b.

The previous discussion assumed a knowledge of the crack spacing. To determine this, we turn to Figure 2.6(b). Notice that the stress intensity increases with increasing crack spacing. Thus, we conclude that the critical crack spacing $b^\star$ would be the one where the peak stress intensity is exactly equal to the toughness. Since the peak is close to the limiting value, and since the normalized value of the peak stress intensity factor N_∞ is independent of b, we use the limiting value instead. So we set $N_\infty = N_c$. We conclude that the *optimal crack spacing* $b^\star$ for a material with transformation strain ε_0 is

$$b^\star = \frac{1}{2\pi}\frac{K_c^2}{\sigma_0^2 N_\infty^2} = 6.28\frac{K_c^2}{\pi E^2 \varepsilon_0^2}\ . \tag{2.5.3}$$

Importantly, since this N_∞ is independent of phase boundary position (Figure 2.6 (d)), this optimal spacing remains unchanged as the phase boundary continues to propagate. Finally, since the stress-intensity falls off beyond the phase boundary independent of the phase boundary position, the stability of a crack with a tip extending just beyond the boundary remains unchanged.

In summary, the previous discussion suggests that the cracks nucleate when the phase boundary propagates to a distance L_{cr} from the free edge. Then uniformly spaced cracks with spacing $b^\star$ nucleate with initial length slightly larger than L_{cr}. Subsequently all the

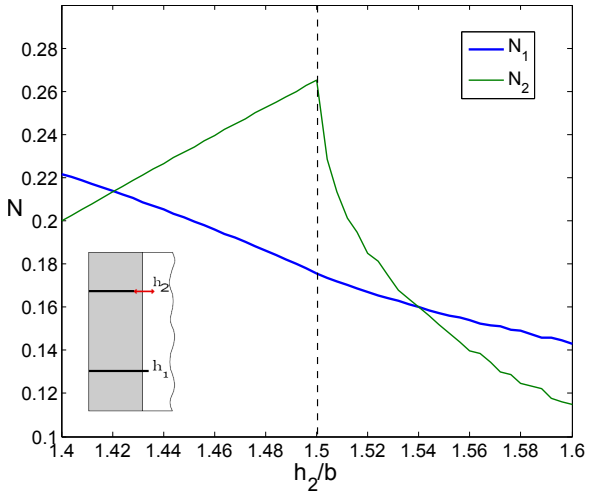

Figure 2.7: Variation of the normalized stress intensity factors ($N = K/\sigma_0\sqrt{2\pi b}$) experienced by the two cracks when the length of one is varied while the that of the other is held fixed. Here, the phase boundary position is $L = 15mm$ indicated by the dotted vertical line while the crack spacing is $b = 10mm$. Crack #1 has a length $h_1 = 15.4mm$ while crack # 2 varies in the range $[14mm, 16mm]$.

crack propagate with the propagating phase boundary in such a manner that the tips reach just beyond the phase boundary.

2.5.2 Stability against period doubling

It is known that in thermal cracks, there is period doubling instability wherein every alternate crack arrests after propagating a certain distance [12, 73]. So we study a periodic array of cracks of alternating lengths. We specifically focus on the onset of an instability where both set of cracks have grown equally in a stable fashion as described above, and then one set continues to grow and the other stops. We therefore study the situation where we have a periodic array of equally spaced cracks with alternating lengths.

Figure 2.7 shows how the normalized stress intensity factors ($N_i = K_i/\sigma_0\sqrt{2\pi b}$) experienced by the two cracks varies when the length of one crack is varied while that of the other is held fixed (see inset). Specifically, the length of the first crack is held fixed at a position slightly beyond the phase boundary representing the equilibrium crack length ($N_1 = N_c$). The length of the other crack varies from just behind the phase boundary to just ahead of it. We see that the stress intensity experienced by the first set of cracks falls monotonically as the second set of crack increases in length. The stress intensity experienced by the second

set increases with crack length till it reaches the phase boundary, and subsequently falls.

The crack propagation criterion dictates that $N_1 = N_2 = N_c$. We see from Figure 2.7 that $N_1 = N_2$ for two possible sets of crack-lengths. The first is when the second set of cracks trails the phase boundary, and the second when the two sets of crack have equal length (just beyond the phase boundary). Since $N_1 = N_2 > N_c$ for the first case, we focus on the second where $N_1 = N_2 = N_c$.

To determine the stability, we combine the definition of the Hessian (2.2.20) with the relation between the driving force and stress-intensity factor (2.3.14) to conclude that

$$H_{ij} = 2\frac{K_i}{E}\frac{\partial K_i}{\partial h_j}. \tag{2.5.4}$$

We are interested in the situation where one crack continues to propagate while the other crack arrests. In this situation, the sufficient condition for linear stability (i.e., the negation of (2.2.19)) is

$$\frac{\partial K_1}{\partial h_2} < 0, \quad \frac{\partial K_2}{\partial h_2} < 0. \tag{2.5.5}$$

(also see [11]). We see in Figure 2.7 that these conditions indeed hold. We have verified that these results hold for various phase boundary positions ranging from $L = 1.5mm$ where we see nucleation to $L = 30mm$ at which point the results converge to that of an infinite system.

We conclude that there is no period doubling instability in phase-transformation driven crack growth.

2.6 Numerical study

The theory above considered only one or two cracks in a unit cell. Further, the stability analysis was limited to linear stability. We use numerical simulations to study multiple cracks in a unit cell and the evolution problem beyond linear stability. After a brief description, we verify the method by showing that the numerical results are consistent with the analysis above and then use it to study more complex situations.

The numerical simulations were carried out using the commercial finite element package

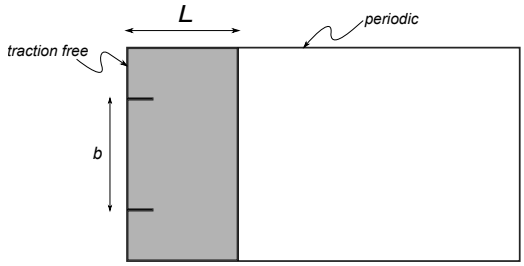

Figure 2.8: Unitcell geometry and boundary conditions.

ABAQUS [1]. We consider plane stress, and a domain that is a long strip. We apply periodic boundary conditions on top and bottom, traction-free conditions on the left and zero displacement on the right, see Figure 2.8. Phase transformation is simulated by treating the material as thermo-elastic, and imposing a temperature difference ΔT across a vertical interface representing the phase boundary.

$$T(x) - T_0 = \begin{cases} \Delta T & x \leq L \\ 0 & x > L \end{cases} \tag{2.6.1}$$

The transformation strain is $\varepsilon_0 = \alpha \Delta T$, where α is the coefficient of linear expansion. We consider both stationary phase boundaries (L = constant) as well as moving phase boundaries ($L = L(t)$). In the latter we ensure that $\dot{L}$ is small enough to ensure quasi-static crack growth.

We use cohesive elements to simulate brittle fracture [17]. We introduce pre-existing cracks or flaws with initial length $h_0 = 0.1b$ at the free edge at a spacing b, and place a series of cohesive elements along the planes ahead of them. This is reasonable because we anticipate only Mode-I cracks to propagate into the solid along horizontal planes. We also note that by introducing flaws, we do not consider nucleation. However, by providing sufficient number of flaws, we let the system choose the crack spacing since not every flaw will develop into a crack. Certain flaws may not develop into cracks, or certain cracks may stop growing thus increasing the spacing between growing cracks.

The material properties we use are as follows : isotropic Young's modulus E = 410 GPa, Poisson ratio $\nu = 0.14$, $\alpha = 4 \times 10^{-5} K^{-1}$, fracture toughness $K_c = 4.6 MPa\sqrt{m}$ and minimum flaw spacing $b = 0.1mm$. Two dimensional, plane stress, four-noded, bi-linear,

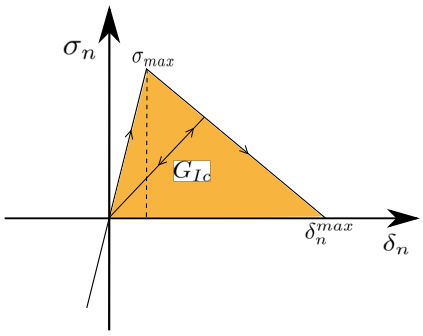

Figure 2.9: Traction-separation law with linear damage evolution.

quad elements (CPS4R) were used to discretize the bulk. Four noded, two dimensional Cohesive elements (COH2D4) were used to simulate crack propagation. The constitutive behaviour of the Cohesive elements is governed through a traction-separation law [1]. We present the important details here and describe the choice of parameters for this simulation. The traction-separation law is governed by two regimes. It consists of a linear regime corresponding to the elastic response of the material prior to initiation of damage. The second regime is the damage response - starting with the onset of damage, evolution of damage and finally suppression of the element - corresponding to deterioration of the material and finally fracture. The damage-onset is based on a criterion which could be traction or displacement based. For this simulation we choose a traction based criterion - damage is initiated once the traction exceeds a peak value. Upon initiation of damage, further loading of the element leads to evolution of the damage captured by a damage evolution law which is represented by the softening portion of the traction-separation law. It must be noted that unloading or compression does not lead to evolution of damage. Various models are available for damage evolution based on effective displacement (to account for mixed-mode loading) or energy. In this case we choose a linear damage evolution law based on effective displacement, see Figure 2.9. The crack is assumed to propagate whenever a cohesive element gets deactivated. This happens when the damage parameter attains a value 1.0 at all the material points in the cohesive element. The parameters of initial stiffness and maximum stress of the cohesive element law were chosen based on the criteria described in [111].

Few comments about the simulation procedure : The size of the cohesive elements needs to be chosen such that it is smaller than the typical cohesive zone size in order to resolve

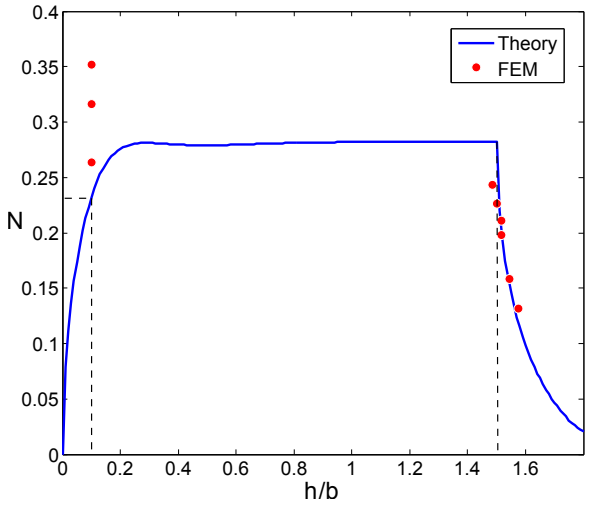

Figure 2.10: Comparison between predictions of theory and numerical simulation. The red points represent the normalized critical stress intensity N_c and final crack length for various transformation strains computed numerically. The blue curve shows the normalized stress intensity as a function of normalized crack length. Note that cracks do not grow when $N_c > N\infty$ and grow to the phase boundary when $N < N_\infty$ showing consistence between theory and numerical simulation. $(b = 0.1mm, L = 0.15mm)$. The cross-hair on the left indicates the initial flaw.

the stresses and thereby capture crack propagation accurately (see [111] and references therein). Next, the step size for phase boundary propagation should be chosen to resolve the variation of stress intensity factor seen in Figure 2.6(a). It was observed during simulations that too big a step size results in artefacts. The convergence difficulties which arise due to the softening behaviour of the cohesive elements are addressed by incorporating viscous regularization [1] and a sufficiently small increment size in the non-linear analysis.

2.7 Results

2.7.1 One flaw in a unit cell

2.7.1.1 Stationary phase boundary

We begin with a single flaw in the computational domain and a stationary phase boundary. With the periodic boundary condition on top and bottom, this corresponds to uniform crack spacing. We apply various transformation strain (i.e., various ΔT) and compute the resulting crack length. The results are shown in Figure 2.10 where the red points display

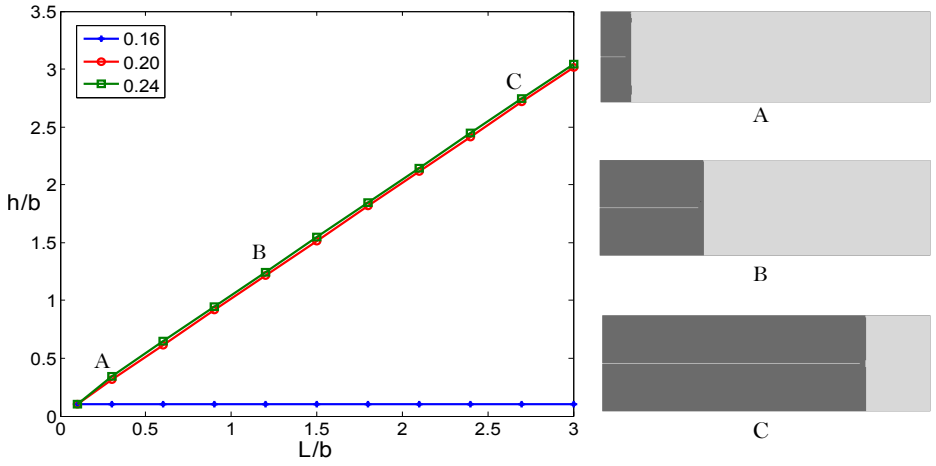

Figure 2.11: Crack growth with a moving phase boundary. Left: The crack length as a function of the phase boundary position for three different values of transformation strain (or equivalently ΔT). Right: Three snap-shots for $\varepsilon_o = 0.24\%$. ($b = 0.1mm$).

the computed normalized crack length for various normalized critical stress intensity $N_c = K_c/E\varepsilon_0\sqrt{2\pi b}$. Note that for small transformation strain or large normalized critical stress intensity, the flaw does not develop into a crack. However, above a given transformation strain (or below a given normalized critical stress intensity), the flaw develops into a crack and grows close to the phase boundary.

Figure 2.10 also shows the normalized stress intensity as a function of the normalized crack length computed using the theoretical analysis of the previous section. Notice that the transition from no crack growth to crack growth is consistent with the theoretical criterion $N_c = N_\infty$. The small discrepancy in transition is due to the following. We used a pre-existing crack of a certain length that happened to be smaller than L_{cr}; so the cracks propagated when N_c reached the value at the flaw instead of the limiting value. We get perfect agreement when we use N_{flaw} instead of N_∞ (see Figure 2.10). Further, in these situations the cracks grow till a position just beyond the phase boundary, again as predicted by the theoretical considerations earlier.

2.7.1.2 Moving phase boundary

We again consider a single flaw, but now consider a moving phase boundary. Figure 2.11 shows the crack length as a function of the phase boundary position for three different values

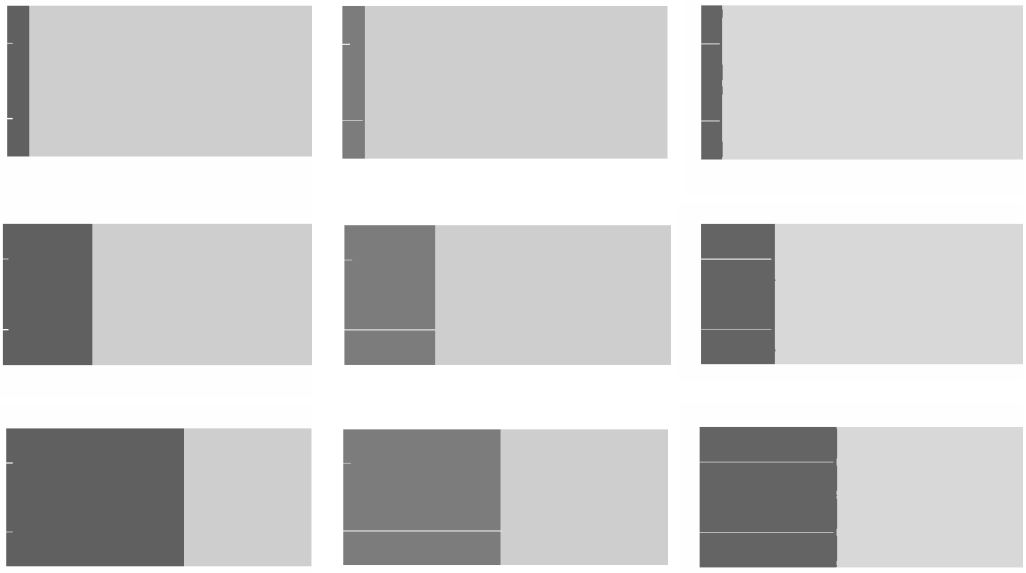

(a) (b) (c)

Figure 2.12: Crack growth with two cracks in a unit cell for varying transformation strains. (a) Three snap-shots with transformation strain of 0.16% shows neither crack grows. (b) Three snap-shots with transformation strain of 0.184% shows the one crack grows along with the phase boundary. (c) Three snap-shots with transformation strain of 0.22% shows the both cracks grow along the grows along with the phase boundary. The flaw spacing is $b = 0.1mm$ and the critical flaw spacing for crack growth at the applied strain based on N_{flaw} are: (a) ∞ (b) $0.17mm$ and (c) $0.056mm$.

of transformation strain (or equivalently ΔT). We see that the crack does not grow for the smallest transformation strain, but does for the larger transformation strains. Note that this is consistent with the theory which predicts that for the given b, the transformation strain has to exceed the critical value of $\varepsilon_o = 0.16\%$ that corresponds to ΔT of 40. Further, when this happens, the crack trip propagates close to the phase boundary, again as anticipated by the theory presented earlier.

2.7.2 Multiple flaws in a unit cell

Figure 2.12 shows the results of simulations with an unit cell containing two initial flaws for three separate values of the transformation strain: 0.16%, 0.184%, 0.22%. The flaw spacing is held at $b = 0.1mm$. The three values of transformation strain are chosen such that the critical spacing according to the (2.5.3) are (a) larger than $2b$ (∞), (b) between b

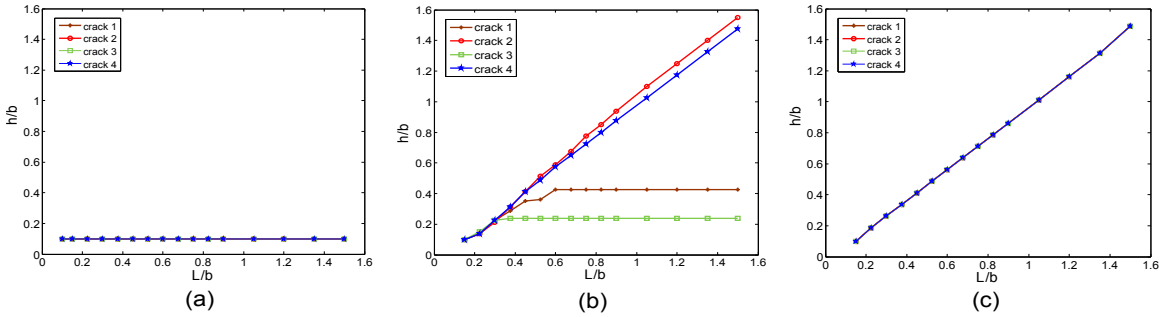

Figure 2.13: Crack growth with four cracks in a unit cell at various transformation strains. Crack length vs interface position for (a) $\varepsilon_o = 0.16\%$ (b) $\varepsilon_o = 0.184\%$ (c) $\varepsilon_o = 0.22\%$. The flaw spacing is $b = 0.1mm$.

and $2b$ ($0.17mm$) and (c) smaller than b ($0.056mm$). Thus, the theory predicts that with an imposed spacing of two cracks, we should see neither crack growing in case (a), only one of the two cracks growing in case (b) and both cracks growing in case (c). These predictions are indeed confirmed by the results of numerical simulations shown in Figure 2.12. These results also confirm the absence of period doubling instability which was concluded earlier from the linear stability analysis.

Figure 2.13 shows the results of simulations with the unit cell containing four initial flaws. The figure shows the position of each of the flaw tips with phase boundary position at three transformation strains. Through this we can examine the stability of the system to modes other than period doubling mode. The flaw spacing provided is $b = 0.1mm$. The results show that though the flaws start propagating initially, some of them stop growing and result in attaining the uniform spacing predicted by theory (see (2.5.3)) at that strain. One might argue that since half of the cracks stopped propagating in case (b) (Figure 2.13) we see a period doubling instability. However this is not the case - this is only the transient response during which a certain spacing between the cracks is established according to (2.5.3). Once uniform spacing is attained, the cracks continue to propagate without any instabilities. If indeed the system were susceptible to period doubling one would have seen one of the two propagating cracks stop at some stage which is not the case. Similarly in case (c), since the transformation strain is high enough and the optimal value of spacing (b^*) given by (2.5.3) is lower than the minimum allowed spacing (b) in the simulation, it is seen that no transient exists and all the cracks propagate at a uniform spacing without any

evidence of instabilities.

2.8 Conclusions

Phase transformations lie at the heart of a number of important technological applications. In these situations the stresses built up due to change in shape resulting from the transformation could cause cracking of the material resulting in compromising the performance of the system. In the current study we seek to understand the interaction between a phase boundary and the cracks resulting due to the phase transition. First we established a condition on the jump in stress across a coherent phase boundary due to a phase transition which gives rise to a set of parallel cracks. Next assuming uniform elastic properties we examine the growth of set of edge cracks in the wake of such a propagating phase boundary in two dimensions. We study the effect of cracks on the phase boundary and conclude that they only have the effect of distorting the phase boundary. They do not effect its overall propagation. We examined the equilibrium configurations of cracks and performed a stability analysis to understand their growth pattern. We found that cracks which nucleate at the edge grow all the way to the phase boundary with the crack tips crossing over, and continue to grow in a stable fashion as the phase boundary migrates into the interior. The mode of growth is devoid of any instabilities typically seen in other scenarios like thermal cracking or due to gradients in concentration of species like drying of paint layers and mudflats. The spacing between these cracks depends on the initial flaw distribution and the strain mismatch of the transformation with the spacing decreasing for higher values of the strain mismatch. These predictions from theory are backed by computational simulations which show that once even spacing between cracks is established they continue to progress without any further instabilities.

2.9 Future Directions

We consider the assumptions we made earlier in order to perform this analysis and discuss how relaxing any of them would make for the pursuit of very interesting problems. We

point out some of them here. Firstly, the assumption that both the phases have similar elastic and fracture properties leads to the conclusion that crack tips would grow all the way to the phase boundary and cross over it. This may no longer be true in the case of dissimilar properties as shown by some quasi-static calculations of cracks in bi-materials. In fact crack propagation in heterogeneous materials is a very active area of research with efforts being made to understand fracture in naturally occurring (nacre, bone etc.) and man-made materials(reinforced composites) and use the understanding to create novel materials with remarkably enhanced fracture properties. We assumed the overall process to be entirely quasi static and neglected the inertia of phase boundary and crack propagation. But experimental evidence suggests that both phase boundary and crack propagation are dynamic phenomena. It would be interesting to see how the inclusion of dynamic effects into the formulation would effect our conclusions. It is not intuitive that upon inclusion of dynamics the cracks would continue tracking the rapidly propagating phase boundary. Finally, though cohesive elements employed in this case to simulate crack propagation worked well we were limited to cracks propagating along straight lines and low number of cracks per unit cell. Utilising other methods available like phase field fracture, XFEM or peridynamics would help in capturing crack growth along arbitrary paths and simulating multiple cracks in a unit cell.

Chapter 3

Effect of Space Charges on Fracture in Ferroelectric Peroskites

3.1 Introduction

Ferroelectric perovskites are materials with a rich array of interesting properties. These materials attain a spontaneous polarization below their Curie temperature which can be switched through the application of electromechanical fields. In their polarized state they display the piezoelectric property and have high dielectric constants. Also, their optical properties are coupled to their polarization state. As a result these materials have found widespread application in transducing devices, dielectric capacitors, memory and optoelectronic devices. From a mechanical property standpoint commonly used ferroelectric perovskites like $BaTiO_3$, PZT are brittle in nature with low fracture toughness values ($K_{IC} \sim 1MPa\sqrt{m}$). In many of these applications these materials are designed to be used in multilayer arrangements. The electrodes embedded in the materials serve as sites for crack initiation during the poling process. The resulting cracks show sub-cyclic growth under applied electromechanical fields. A prominent issue is the growth of cracks connecting the electrode layers resulting in electric discharge and breakdown, Figure 3.1. This has motivated an effort to understand the fracture behaviour of ferrolectrics.

Efforts to understand the fracture behaviour of ferroelectrics revealed the complex nature of this area of study. Early experiments to understand the fracture behaviour of perovskites, using the indentation technique, established the anisotropic nature of crack growth in materials [112, 78, 83]. These experiments performed on poled polycrystalline

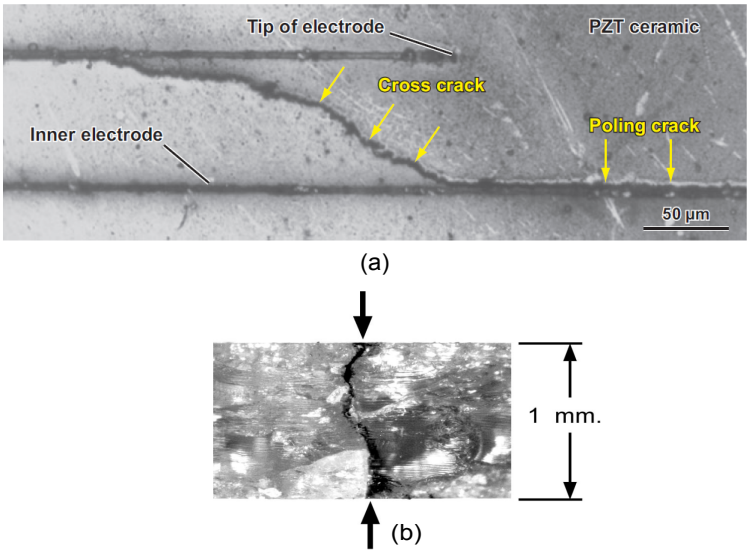

Figure 3.1: Cracks in piezoelectric actuators. (a) Multilayer actuator (b) Electric discharge

materials consistently produced longer cracks normal to the poling direction than those parallel to it at a given indentation load. Sub-critical crack growth under cyclic electric fields and crack growth under static electric fields in the absence of any applied mechanical load motivated research to establish the dependence of crack growth on the applied electric field. However the experiments undertaken to establish this did not produce consistent trends. The experiments by Mehta and Virkar[69] and Fang et.al [50] established that polarization domain switching around the crack played a significant role in crack growth under pure electrical loading and switching induced toughening of ferroelectrics.

On the modelling front, the theory of linear piezoelectric fracture was developed and applied to fracture in ferroelectrics. This theory does not take into account the non-linear phenomenon of domain switching. The predictions of this theory strongly depend on the boundary conditions assumed at the crack surface and wrongly concluded that electric fields can not induce fracture. So constitutive laws based on micromechanical models to account for domain switching were used to estimate the extent and influence of domain switching around the crack tip and its role in crack growth under the applied electric fields. Phase field models based on the Devonshire-Ginzburg-Landau (DGL) type multiwell potential were used to establish the evolution of polarization domains around the crack as seen in experiments and used to evaluate the driving force on the crack. The choice of crack surface

boundary conditions significantly effected the predictions of these models and so were an issue of much debate. So determining what the right boundary conditions are would go a long way in shaping the fracture mechanics of ferroelectrics.

Fatigue of ferroelectric perovskites and dependence of the coercive field of thin films on thickness present evidence that the defects and the semiconducting nature of these materials play an important role in their overall response. However none of the above mentioned approaches incorporate this physics while addressing the question of fracture. Models by YuXiao et.al [120, 94] and experiments by Shilo [96] have shown the accumulation of defects and electronic charge in regions of high electric potential like 90^o domain walls. Recent Kelvin Force Microscopy experiments [89, 105, 30], have showed that crack faces are regions of high electric potential and speculate that charges accumulate on the surface of these cracks and increase the permittivity of the crack gap. The electronic charge injection from the electrodes and ionization of dopants could be a source of these charges. Understanding the effect of including this new physics in studying the fracture of perovskites serves as our motivation.

In the current work we consider the problem of fracture in single crystal ferroelectric perovskites incorporating space charge arising from their semiconducting nature and ionization of defects. The model closely follows [120] with modification to account fro the crack. We perform phase field simulations of polarization around a stationary center crack in a square domain using a gradient flow model. The simulations reveal the accumulation of electronic charge at the crack tip which leads to the conclusion that crack tip becomes permeable resulting in the high permittivity of the crack gap in the experiments [30, 105]. The polarization domains that develop around the crack were found to be asymmetric when the space charge was included. There is no direct experimental evidence to support this which could be due to large length scale difference in our simulation and experiments.

We begin by considering the dissipation of a ferroelectric domain containing a crack subject to external fields. This analysis gives the equations governing the polarization distribution, mechanical equilibrium and space charge density at equilibrium, driving force acting on the crack and crack face boundary conditions. We present a rigorous derivation of

the crack driving force through the dissipation approach and highlight its salient features.

The chapter is organized as follows. First, in Section 3.2 we provide a background on the structure and properties of ferroelectric perovskites, especially $BaTiO_3$. In Section 3.3 we provide a detailed overview of literature on fracture of single crystal ferroelectrics. We provide details of important experiments, models and simulations. We note that discrepancies that exist in the variation of energy release rate with applied field and highlight that domain switching and crack face boundary conditions play an important role in predicting the fracture behavior. In Section 3.4 we introduce a few important ideas and terminology related to semiconductor physics and go on to discuss the semiconducting properties of ferroelectrics. We discuss the presence of defects in these materials which act as dopants and which play a significant role in their thin film properties like ferroelectric fatigue and size dependence of coercive field. The experiments by Shilo et.al. [96] and the simulations of Xiao et.al. [120] show the accumulation of these defects and electronic charge in regions of high electric potential. In Section 3.5 we introduce the set-up and derive the governing equations through the dissipation inequality approach. We introduce a new variable, ρ, the space charge density to account for the semiconducting nature and ionization of defects. After formulating the governing equations, we present the implementation details for the case of a $BaTiO_3$single crystal section in section(3.7). The results obtained from the implementation for different dopants are presented in section(3.8). It is seen from these simulations that there is accumulation of electronic charge around the crack surface and introducing space charge changes the polarization domains in the ferroelectric. We present a one-dimensional model along the lines of [94], to explain some of these observations in Section 3.9. Finally we develop the expression for the driving force on a crack in a ferroelectric in Section 3.10, apply it to the results and discuss the variation of J with applied field. We conclude in Section 3.11.

3.2 Ferroelectric perovskites

Perovskites are materials with the same type of crystal structure as $CaTiO_3$. This class of crystals is usually represented by the general formula ABO_3 where A is a monovalent,

divalent or trivalent metal and B a pentavalent, tetravalent or trivalent element respectively. Some of the well known perovskite materials which also exhibit ferroelectric properties are barium titanate ($BaTiO_3$), lead titanate ($PbTiO_3$), potassium niobate ($KNbO_3$). Some of the other commonly used ferroelectrics like lead zirconate titanate (PZT, $Pb[Zr_xTi_{1-x}]O_3$) and lead magnesium niobate-lead titanate PMNT are solid solutions of perovskites.

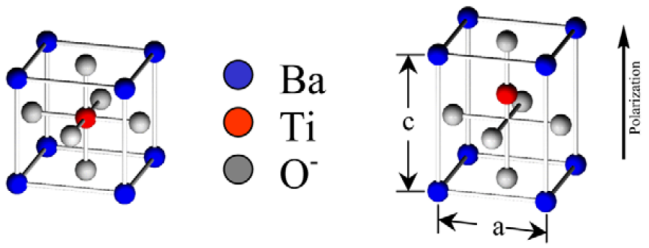

Figure 3.2: Perovskite structure of $BaTiO_3$ in the cubic and tetragonal state. Reproduced from [15].

For a more detailed discussion on ferroelectric properties, let us consider the case of barium titanate. This is also our ferroelectric material of choice for later in this study. As shown in Figure 3.2, $BaTiO_3$is a perovskite with the atoms arranged in a cubic lattice ($a = 4.01\ \mathring{A}$). Its Curie temperature is, $T_c = 120^oC$. The barium atoms occupy the corner positions of the cube, the titanium atom occupies the body-center position and the oxygen atoms are arranged at the face centres. As it is cooled the cubic lattice undergoes a transformation to a tetragonal lattice ($a = 3.992\ \mathring{A},\ c = 4.0361\ \mathring{A}$) with the barium and titanium atoms shifting upwards relative to the oxygen sites [54]. This results in lattice strains, $\varepsilon_c = 0.65\%$ and $\varepsilon_a = -0.44\%$. In the cubic state the centres of positive and negative charge are coincident and so the crystal is electrically neutral and has no net polarization. However in the tetragonal state the centres are no longer coincident resulting in a spontaneous dipole moment (density, $p_s = 0.26C/m^2$) in the crystal, see Figure 3.2.

As the unit cell transforms from the non-polar cubic state to a polar tetragonal state there is also a loss in the symmetry of the crystal. This loss of symmetry results in the formation of variants - energetically equivalent states which only differ from each other through their relative orientation with respect to the parent cubic unit cell, Figure 3.3. Note that though there are six distinct polarization states among the variants there are only three

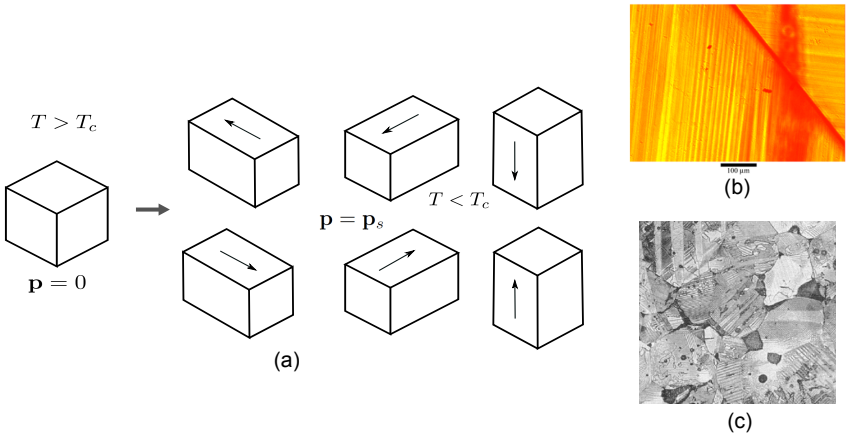

Figure 3.3: (a)Six variants of $BaTiO_3$. (b) Polarized light optical micrographs of domain patterns in $BaTiO_3$single crystal [16].(c) Domains of variants in a $BaTiO_3$crystal [48].

distinct spontaneous strains. So in any given sample of a $BaTiO_3$crystal, depending on the electromechanical boundary conditions it is subject to, the variants coexist making up regions of uniform polarization called domains. These domains coexist in a crystal separated from each other through domain walls. So a domain wall represents a discontinuity of the spontaneous polarization vector $\mathbf{p_s}$ and the spontaneous strain ε_s. A coherent domain wall has to satisfy certain compatibility conditions on the the polarization vector and the spontaneous strain [98, 15], and these are fulfilled only by 90^o and 180^o domain walls in the case of $BaTiO_3$. A 90^o domain wall separates domains with their polarization vectors oriented at right angles with respect to each other and a 180^o domain wall separates domains with polarization vectors anti-parallel to each other. The variants are energetically equivalent states and upon the application of external electromechanical fields it is possible to make one variant switch to another and back, see Figure 3.4. The switching usually takes place through the nucleation and growth of the new variant inside the original variant [126, 24]. The threshold value of the applied electric field which would cause a 180^o switching is termed the coercive field, $\mathbf{E}_c$. Typically its values are in the range of several kV/cm. When ferroelectric ceramics are poled to be used as piezoelectric ceramics, they are subject to large external fields which aligns the polarization domains along the direction of the applied field. Also macroscopic strain, resulting when a domain undergoes 90^o switching, is exploited to generate large strains in ferroelectric actuators [98]. Later we will see that

the phenomenon of switching under the influence of intense electromechanical fields around the crack plays a significant role in the fracture behaviour of ferroelectrics.

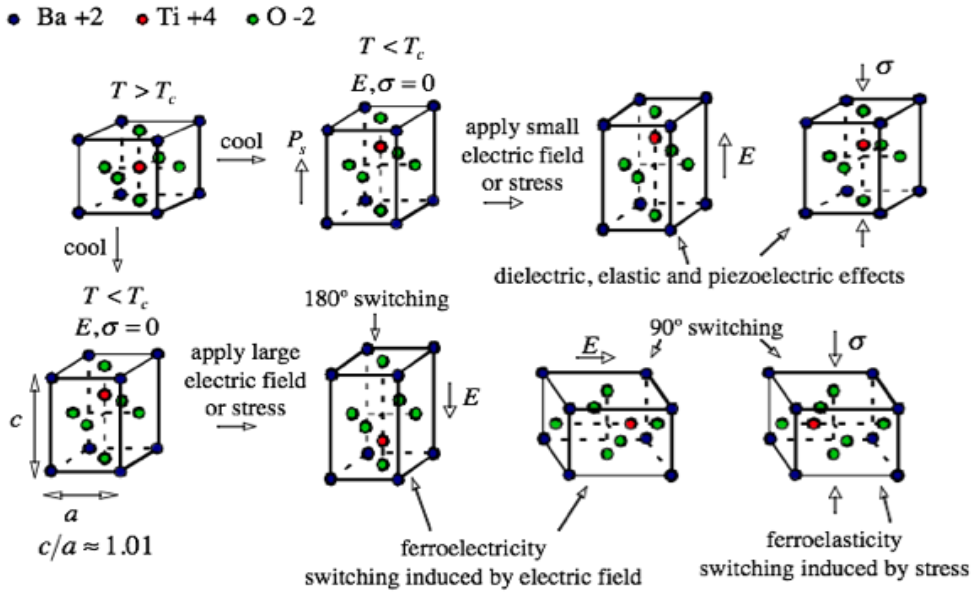

Figure 3.4: Switching of $BaTiO_3$ unitcell under electromechnaical loading. Reproduced from http://www.ae.utexas.edu/ landis/Landis/Research.html.

3.3 Fracture behaviour of ferroelectric perovskites

Ever since ferroelectric materials have been increasingly used for various applications such as electromechanical devices, microelectronics, smart composites and memory devices and since these materials are brittle in nature which make them susceptible to cracking resulting in the electrical/mechanical failure of the device they are used in, researchers have devoted much attention to understanding their fracture behaviour. Here we present a survey of the efforts to understand the fracture behaviour of ferroelectrics through experiment, modelling and theory. This is by no means comprehensive since we pay most attention to fracture of single crystal samples. For more detailed reviews one should refer to the excellent review articles on the topic by Schneider [91], Fang et.al [23] and Kuna [58]. A convention that is followed while reporting results is that when the applied field is along the poling direction it is termed positive and when anti-parallel it is termed negative. We adopt it here.

3.3.1 Experiments on fracture of ferroeletrics

Fracture of poled ceramics

We start by reviewing experimental literature. Multiple techniques and tools have been used to study crack propagation in ferroelectrics. Indentation and compact-tension(CT) specimen experiments established early on that crack growth is anisotropic in poled ferroelectric ceramics (polycrystals) and shows a toughening behavior [112, 83, 70, 27].

Indentation experiments are particularly amenable to examining the effect of applied field on cracks parallel and perpendicular to the field. Singh and Wang [112] performed Vickers indentation experiments on poled PZT ceramics in air and observed crack growth anisotropy with respect to poling direction and applied electric field. They observed that field direction did not have a significant effect on the cracks parallel to poling direction. In the case of cracks perpendicular to poling direction, positive fields arrested the growth of cracks and negative fields aided them. Fu and Zhang [37], using indentation in PZT-841 observed increasing crack lengths for positive electric fields but also an increasing crack length for negative electric fields. Indentation experiments by Tobin and Pak on PZT-8 [110], Sun and Park on PZT-4 [104] and Schneider and Heyer on $BaTiO_3$[90] show that a positive electric field perpendicular to the crack leads to an increase in crack length, whereas a negative electric field reduces it until the coercive field is reached. Mehta and Virkar [69] presented early X-ray measurements demonstrating domain switching around cracks in poled PZT ceramics.

Park and Sun [79] measured the fracture load versus the applied electric field for CT specimens of poled PZT-4 in silicone oil in which the poling and electric field directions were perpendicular to the crack orientation. The fracture load decreased monotonically from negative to positive electric fields showing positive fields aid crack growth and negative fields inhibit it. Fu and Zhang [37] conducted the same test with PZT-841 samples and measured a decreasing fracture load for positive fields but also a reduced load for a negative field.

These experiments on poled ceramics show that crack growth parallel to the poling direction has a toughening behavior and electric fields do not influence it. However there

is no consistent trend as far as the effect of electric field on crack growth perpendicular to the crack growth is concerned. Domain switching around the crack in ceramics is believed to play a significant role in influencing these trends.

Fracture in single crystals

Using in-situ polarized light microscopy (PLM), Jiang and Fang [51] captured 90^o domain switching around the crack tip in a single crystal PMNT sample poled normal to the crack subject to cyclic electric fields. They observed no 180^o switching under a negative field. Under a negative electric field they reported the appearance of extensive switching, Figure 3.5, and upon reversing the field (positive) the domains disappeared. In a subsequent article [50] they also reported the growth of cracks under a static negative electric field only. They argued that driving force for crack growth is provided by the switching. Fang et.al [33] also conducted experiments using the same technique on a single crystal $BaTiO_3$three point bend specimen with the crack parallel to poling direction. As the crack grows there is 90^o switching in the wake of the crack , see Figure 3.5, which helps in toughening the ceramic. Fang et.al [34], showed the propagation of cracks in single crystal $BaTiO_3$subject to alternating electric fields above and below the coercive field value. They also hypothesized that the crack gap could be conducting close to the tip and insulating away from it. So in the case of single crystals, negative fields promote crack growth normal to the poling direction. Also domain switching contributes to the toughening behaviour seen in crack growth along the poling direction.

Electric Potential around the crack and nature of crack gap

In a series of articles, using the techniques of atomic force microscopy (AFM) and Kelvin force microscopy (KFM), Schneider et.al [89, 30] investigated the variation of electric potential around an indentation crack in a poled PZT ceramic sample with the crack surface normal to the poling direction and subject to external electric field. From the measurements they concluded that the permittivity of the crack gap is much higher than that of vacuum, which was what was previously thought to be. They suggested that accumulation of charges

on the crack surface could be a potential reason, but rule out bulk conduction due to low conductivity of PZT. Based on this value of the permittivity they conclude that applied electric fields would have no effect on crack growth. Using similar experimental techniques Sun et.al. [105], studied the potential distribution around an indentation crack in a single crystal $BaTiO_3$sample with the crack surface almost normal to the poling direction with and without applied fields. The measured electric potential had peak values along the crack surfaces, see Figure 3.6 which was attributed to the build up of screen charges along the crack surfaces. Interestingly they observed little to no switching in the sample. The potential values increased with crack opening suggesting greater accumulation of charge away from the crack tip.

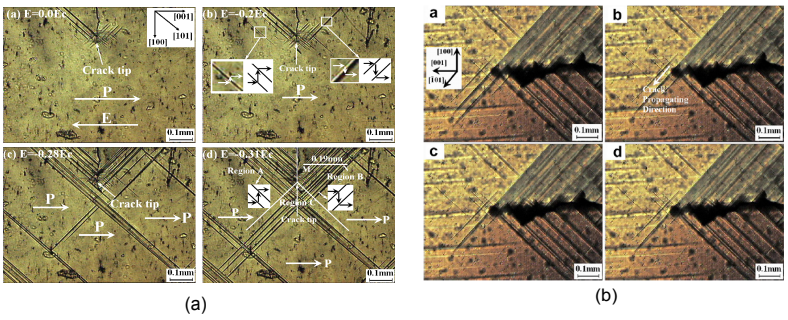

Figure 3.5: Evolution of domain switching near a crack tip in poled PMN-PT(62-38) single crystal under negative electric fields. Reproduced from Jiang et.al. [51].

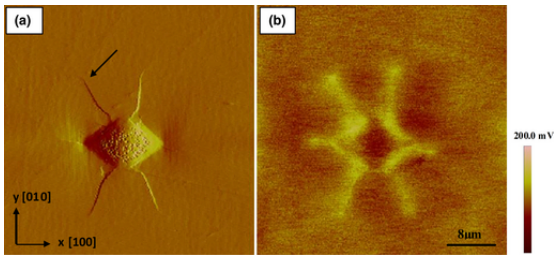

Figure 3.6: (a) Topographic image and (b) surface potential image of the indentation-pre-cracked $BaTiO_3$ single crystal. Reproduced from Sun et.al. [105].

3.3.2 Modelling and simulation

Early models of cracking in ferroelectrics treated them as linear piezoelectrics. The theory of linear piezoelectric fracture mechanics was developed through a series of contributiions [125, 75, 106, 101, 29, 76, 122, 80, 78]. The theory predicts singularity in stress and electric

fields at the crack tip in the case of impermeable cracks. Note than this theory doesn't consider the non-linearity due to domain switching around the crack. According to the theory, the predictions for fracture strongly depend on the choice of boundary conditions. For an insulating crack, with the crack normal to the poling direction, energy release rate is negative for applied electric fields in the absence of mechanical loading. For conducting cracks the applied field does not influence crack growth. For permeable cracks energy release rate is independent of the electric field if the crack is treated as a slit. If the crack opening is considered, due to the electrostatic energy stored in the gap, electric fields retard crack growth. The impermeable crack and the conducting crack are the two extreme boundary conditions. Other conditions, like semi-permeable and energetically consistent boundary conditions, lie between these extremes. The issue of the right crack face boundary conditions has remained a topic of much debate.

Phase field modeling has been employed extensively to investigate the domain switching around the crack and investigate the effect of applied fields on the crack as a result [114]. More details about phase field models are presented in the Section 3.5. Wang and Kamlah [114], using a phase field model in three dimensions, investigated the polarization switching around an impermeable notch (parallel to the poling direction) in a single crystal subject to far field stress. They established that polarization switching takes place near the notch tip if the mechanical loading exceeds a critical value. Furthermore, the simulation results show that a positive electric field increases the critical value while a negative electric field decreases it. Yang and Dayal [124] performed simulations on a surface crack in a $BaTiO_3$crystal, taking into account the stray electric fields in the full space. They studied the effect of crack surface charge compensation on the microstructure around the crack and the effect of external fields. When the crack surface was uncompensated, the was extensive switching and the effect of applied fields was minimal, where as in the fully compensated case there was no microstructure rearrangement and the external fields had a significant influence. Song et.al. [100] used a phase field model in two dimensions and assuming an insulated crack surface, simulated switching around a center crack in a square panel and a square region close to the crack tip. They concluded from the calculations that positive fields inhibit fracture and

negative fields promote fracture. Wang and Zhang [115] simulated the region around the crack tip, assuming a permeable crack with the poling direction normal to the crack. Their calculations of the J-integral concluded that the positive fields promoted the toughening of the material whereas a negative field reduced the toughness. Xu et.al. [121] used phase field modelling and configurational force balance to explore the effects of different boundary conditions and applied field. They show that the crack driving forces for additional positive electric fields are smaller than the driving force under merely mechanical loading (i.e. E = 0). On the other hand, the crack driving force for additional negative electric fields is larger than the driving force under merely mechanical loading. The phenomena hold for the four different boundary conditions. It follows from their analysis that a positive electric field tends to inhibit fracture, while a negative electric field tends to promote it.

Using a phase field for both polarization and fracture, Abdollahi and Arias [2, 3] simulated the evolution of polarization domains in a single crystal with a growing crack under different crack surface boundary conditions. Their simulations showed that a negative electric field below the coercive field perpendicular to the crack enhances the crack propagation in ferroelectrics, while a positive electric field retards it, for all crack surface conditions. A negative electric field above the coercive field perpendicular to the crack retards the crack propagation in ferroelectrics for all crack conditions due to 180^o switching.

Landis [113, 59], using an incremental constitutive law which accounted for domain switching, examined Mode-I crack growth in poled ferroelectric ceramics subjected to simultaneous electrical and mechanical loading. The results show that the toughening due to switching is greater for crack growth parallel to the poling direction than for crack growth perpendicular to the poling direction for the in-plane cases. They also concluded that a positive electric field reduces toughening and negative electric field increases toughening for polarization perpendicular to the crack. Landis [60] also surveyed the different crack surface boundary conditions and pointed out their inconsistencies. He proposed a new set which were energetically consistent.

In summary, this review reveals the complexity of the problem of fracture in ferroelectrics. Multiple phenomena like domain switching, poling state, crack face boundary

conditions, crystalline (single or polycrystal) state of the ferroelectric play a role. Motivated by the recent KFM experiments which speculate accumulation of charges on the crack faces which make the crack gap permeable, we seek to examine if the semiconducting nature and ionization of defects found in perovskites offer a mechanism to explain the build up of charge on the crack face. We do this by implementing a phase field model in two dimenions.

3.4 Semiconducting nature of Ferroelectric perovskites

3.4.1 Semiconductor physics

Before we discuss the semiconducting features and defect physics of ferroelectrics we briefly introduce a few basic ideas and terminology related to semiconductor physics which would be useful going forward. For a more rigorous discussion the reader may refer to comprehensive texts on semiconductor and solid state physics [6, 108]. To understand the conduction properties of crystalline solids one may start from the band structure obtained by solving the Schroedinger equation for one electron in a periodic potential. It is an eigenvalue problem with the eigenvalues corresponding to the energy states of the electrons an the eigenvectors corresponding to the orbitals. The energy states of electrons in crystallines solids are arranged in the form of energy bands with some gaps between the bands for certain materials. This gap is called the band-gap, E_g - measured in eV, and represents energy states which are inaccessible to electrons for occupation. The conduction behaviour of a crystalline solid is determined by the width of the band-gap - conductors do not have a band-gap, insulators have a large value for the band-gap (eg. diamond: 5.5 eV, aluminium nitride: 6.3 eV) and semi-conductors have moderate values (eg. silicon: 1.11 eV, germanium : 0.67 eV at 300K), see Figure 3.7. The energy states or orbitals below the band-gap correspond to localized states and the electrons occupying these states are immobile and bound to the nucleii. The edge of this band corresponding to the highest energy state is represented by E_v. The orbitals above the band-gap form the conduction band which are delocalized with the electrons residing in this band free to move around in the crystal. These electrons contribute to the conductivity of the solid. The edge of this

band corresponding to the lowest energy is denoted by E_c. When the orbitals are filled they start with the lowest energy states and progressively fill the higher states following the exclusion principle. In a crystalline solid the highest energy level that is filled at zero Kelvin is termed the Fermi-level, E_f, of the material. This is also equal to the chemical potential of electrons in the material since it is the energy level that an electron entering or leaving the material occupies. It also represents the work-function, ϕ_M, the work necessary to remove the electron from the solid. In a typical insulator all the electrons reside in the valence band in their ground state and so there are no electrons available for conduction. In a conductor, since there is no energy gap, there are electrons always residing in the conduction band. In a semi-conductor, depending on the temperature, electrons residing in the valence band can jump across the band gap into the conduction band and improve the conductivity in the solid. When an electron from the valence band jumps to the conduction band it creates a hole in the valence band which is conceptually treated as a positive charge carrier which assists in the conduction. The mobility of holes is typically lower than that of the electrons. In short, there are two types of charge carriers in semiconductors - electrons in the conduction band and holes in the valence band. In a pure semiconductor at any given temperature the density of holes is same as that of electrons. In this pure state the Fermi-level of the solid lies halfway between the bottom of the conduction band and the top of the valence band, $E_f = \frac{E_c+E_v}{2}$.

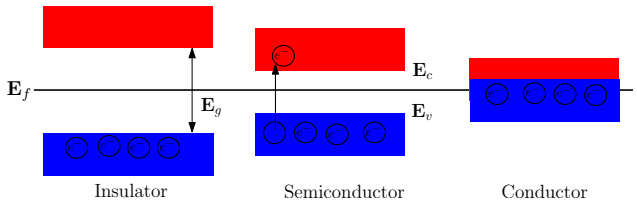

Figure 3.7: Band diagram of crystalline solids.

The description of the band structure provided above is that of an intrinsic or a pure semiconductor without any impurities. However adding certain types of impurities to semiconducting solids enhances their conductivities. The impurities or defects are classified as donors - species which donate electrons to the conduction band - and acceptors - species which accept electrons from the valence band creating holes. The typical concentrations

of these imperfections are in the range of $10^{23} - 10^{26}/m^3$. Upon doping new energy levels are created within the band gap of the intrinsic semiconductor. In the case of donor impurities (elements with excess valence electrons than required for binding) these levels - called donor levels, E_d - are created close to the edge of the conduction band. The electrons which reside in these levels have very low ionization energy ($\approx 0.01eV$) and easily jump into the conduction band enhancing the conductivity of the semiconductor, see Figure 3.8. Similarly in the case of acceptor impurities, new energy levels - acceptor levels - are created in the band gap close to the valence bad. These impurities have valence electrons lower than what is necessary for bonding and so can accept electrons from the valence bad. So when an electron from the valence band jumps into the acceptor level it leaves behind a hole which contributes to the conductivity of the semiconductor, see Figure 3.8. So the primary charge carriers in the case of semiconductors doped with donor impurities are electrons and the semiconductor is called n-type and those doped with acceptor impurities are holes and the semiconductor is called p-type. The fermi level in doped or extrinsic semiconductors no longer resides in the middle of the conduction and valence bands. In the case of p-type semiconductors it is closer to the valence band and in the case of n-type semiconductors is closer to the conduction band, see Figure 3.8.

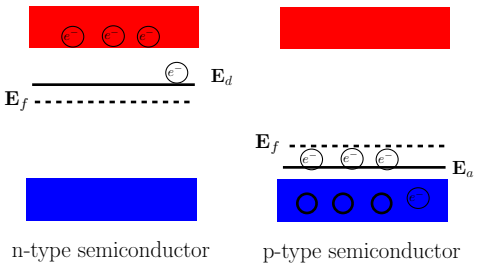

Figure 3.8: Band diagrams of extrinsic semiconductors.

Whenever a metal and semiconductor having different Fermi-levels are brought in contact with each other the electrons in the metal and the majority carriers in the semiconductor close to the interface rearrange themselves so as to attain a uniform Fermi-level in the two solids at equilibrium. This rearrangement of electrons typically results in creating a small region next to the interface in the semiconductor which is devoid of mobile carriers. This insulating region is called the depletion layer. The rearrangement of charges

creates an electric field within the depletion region. This results in shifting of the bands known as band bending, see Figure 3.9. The properties in the bulk of the semiconductor are however unaffected. The bending of bands near the interface creates what is called a built-in potential inside the semiconductor and a potential barrier between the metal and the semiconductor called the Schottky barrier.

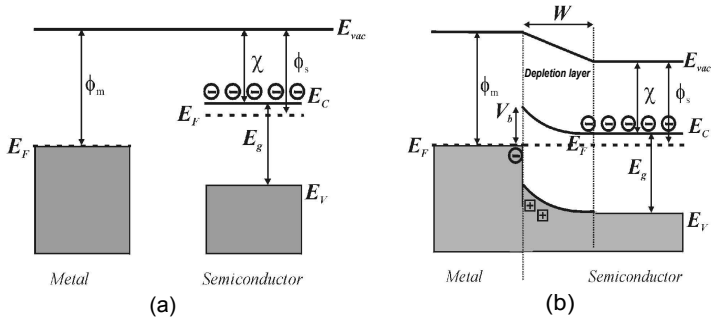

Figure 3.9: Metal, n-type Semiconductor interface. (a) Before contact. (b) After contact showing the depletion layer and band bending.

3.4.2 Defects in perovskites

Ferroelectrics have largely been modelled as polarized dielectrics while infact they are wide band-gap semiconductors. The band gap values of some of the commonly used ferroelectrics like Barium Titanate ($BaTiO_3$) and Lead Zirconate Titanate (PZT (0.4-0.6)) are 3.0 eV and 3.4 eV respectively. The relatively large values of the band-gaps of typical ferroelectrics justifies their treatment as insulators. However these materials contain a large number of defects in them which act as dopants, resulting in the semiconducting behavior of ferroelectrics. This can alter the electric fields and have a profound effect on their overall behavior [93]. Typically, if undoped, perovskites like $BaTiO_3$and PZT display the properties of p-type semiconductors [39, 93]. This is due to the presence of Pb vacancies in PZT and abundance of impurities such as Na, Al, Fe and Mg in the starting growth materials. These impurity atoms create substitutional defects in ABO_3, with Na^{+} substituting for Ba^{2+} or Pb^{2+}, Al^{3+}, Fe^{3+} or Mg^{2+} for Ti^{4+}. Oxygen vacancies are the other major defects in these materials which give them a n-type behavior. The vacancy created by a missing Oxygen atom leaves two electrons at the vacancy site. Thus an oxygen vacancy acts as donor impu-

rity with two electrons with a binding energy of 1 eV. Majority of these defects are in the ionized state at room temperature and contribute to the conductivity of the ferroelectric. Also oxygen vacancies have a significant mobility which adds to the electrical conductivity [85].

The defects in these materials and the semiconducting nature of ferroelectrics have been found to play a significant role in influencing the properties of thin films. Ferroelectric fatigue is an example. This is defined as the loss in switchable polarization with cycling. The semiconducting nature is necessary to be considered to explain the dependence of fatigue life on the choice of electrodes [92]. Several mechanisms have been proposed to explain the influence of defects on this phenomenon like electronic charge trapping and oxygen vacancy redistribution [93, 24]. Experiments by Shilo et.al [96] have shown evidence of accumulation of these defects at 90^o domain walls. So there has been an effort to include the semiconducting nature and defect diffusion in modelling ferroelectrics [116, 117, 120, 107, 71, 72]. Simulations by Xiao et.al.[120], based on a semiconducting model of the ferroelectric and accounting for diffusion of oxygen vacancies have shown that 90^o domain walls are regions of high electrostatic potential and ionized defects tend to migrate to these regions. Also simulations by Yang and Dayal [123] of closure domains near a free surface show the accumulation of electronic charge around the 90^o closure domains which are regions of high potential. Once the vacancies migrate to these regions of high potential like domain walls, they interact with them and contribute to pinning the domain wall migration as shown in [103].

All the above evidence points to the fact that ionized defects and electronic charge injected into the ferroelectric through the electrodes accumulate in regions of high potential like domain walls. Recent experiments by Sun et.al [105] suggest that the region around a crack in a ferroelectric has higher electric potential compared to the surroundings. So it is possible that there is charge accumulation though ionization and diffusion of vacancies and accumulation of electronic charge around cracks. Since the polarization and charge interact indirectly through the electric potential, the presence of space charge around the crack would influence the polarization domain formation. Also the accumulation of charge

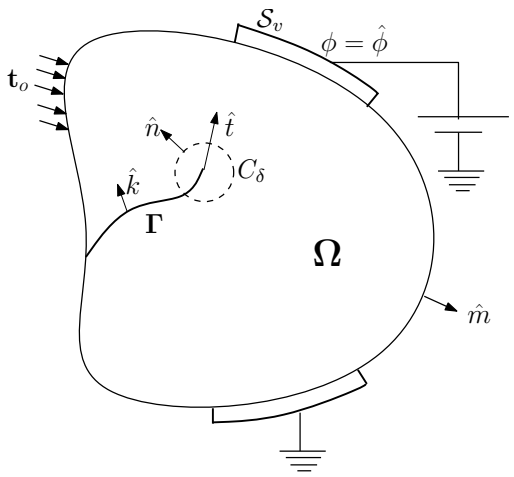

Figure 3.10: Ferroelectric domain with a crack subject to tractions and external electric field.

on the crack surface would change the electrostatic behaviour of the crack gap. These effects would influence the effect that external fields have on promoting or mitigating fracture in ferroelectrics. This hypothesis serves as the motivation for this work where we examine the effect of the semiconducting nature and presence of defects on the fracture behaviour of ferroelectrics.

3.5 Phase field model

Phase field models have been developed to study domain structures in ferroelectric materials and polarization switching under electric and/or mechanical loading [18, 20, 126, 103]. The main ingredients of the model are the Devonshire-Ginzburg-Landau type multiwell energy potential in terms of the order parameter to model the different variants, a gradient term to penalize rapid changes in the order parameter representing the energy associated with domain walls and the Maxwell's equation which governs the distribution of the electric potential. Since we are interested in including the semiconducting behaviour an additional energy term corresponding to the space charge is introduced. The order parameter - the polarization vector $\mathbf{p}$ in the case of a ferroelectric - is evolved through the gradient flow of the energy.

3.5.1 Kinematics

We derive the governing equations using the dissipation inequality following Xiao and Bhattacharya [120]. Consider a ferroelectric domain Ω containing a crack Γ, attached to electrodes $\mathcal{S}_v$ maintained at a constant potential $\hat{\phi}$ along the part of the boundary $\partial\Omega_{\mathcal{S}}$. The part of the boundary not covered by electrodes is assumed to be in contact with the surrounding insulating medium. The ferroelectric is subject to tractions $\mathbf{t}_o$ on a region $\partial\Omega_t$ of the boundary. The rest of the boundary, $\partial\Omega_u$, is subject to fixed displacement . Let $\hat{m}$ represent the outward normal to $\partial\Omega$ and $\hat{k}$ the normal to the crack surface Γ pointing from the lower crack surface to the top. We derive the equations assuming linearised kinematics. The polarization density vector is represented by $\mathbf{p}$, displacement by $\mathbf{u}$. The semiconducting nature of the ferroelectric is introduced through the variable, ρ, representing the space charge density. To account for any potential singularity of the fields at the crack tip, we remove a cylindrical domain $\mathcal{C}_\delta$ of radius δ and traversing the crack front. Let $\hat{n}$ represent the normal to $\partial\mathcal{C}_\delta$ pointing into Ω. We associate an instantaneous tangent vector $\hat{t}$ and velocity a with the crack tip representing its growth direction and velocity magnitude respectively. The domain $\mathcal{C}_\delta$ is assumed to move along with the crack tip. The jump in a quantity across a surface is denoted by $[[\ ]]$.

3.5.2 Rate of dissipation

We examine the dissipation in the ferroelectric domain Ω which would yield the equations governing the field variables, boundary conditions and driving force on the crack. Under the above assumptions, isothermal conditions, and allowing crack growth the dissipation in the specimen is given by

$$\mathcal{D} = \mathcal{F} - \frac{d\mathcal{E}}{dt}, \tag{3.5.1}$$

where $\mathcal{D}$ is the dissipation , $\mathcal{F}$ is the rate of external work, $\mathcal{E}$ is the *potential energy* of the system.

Rate of external working

The rate of external work on Ω is given by

$$\mathcal{F} = \int_{\partial\Omega_t} \mathbf{t}.\dot{\mathbf{u}} ds + \hat{\phi}\frac{d}{dt}\int_{\partial\Omega_v} \sigma ds - \int_{\partial\Omega} \mu\mathbf{J}.\hat{m} ds, \tag{3.5.2}$$

where μ represents the chemical potential of the charge species in the ferroelectric and $\mathbf{J}$ is the flux of the charge species. So the last term represents the chemical energy flux from the electrodes into Ω with $\mathbf{J}$ representing the flux at $\partial\Omega$ (so if $\mathbf{J}$ is parallel to $\hat{m}$ the ferroelectric is losing species and does work).

Using the divergence theorem (A.3.6) on the chemical flux term and conservation law, $\dot{\rho} = -\nabla.\mathbf{J}$, the rate of external work (3.5.2) can be simplified as

$$\mathcal{F} = \int_{\partial\Omega_t} \mathbf{t}.\dot{\mathbf{u}} ds + \hat{\phi}\frac{d}{dt}\int_{\partial\Omega_v} \sigma ds - \int_{\Omega_\delta} \nabla\mu.\mathbf{J} dx + \int_{\Omega_\delta} \mu\dot{\rho} dx - \int_{\partial C_\delta} \mu\mathbf{J}.\hat{n} ds + \int_{\Gamma} [[\mu\mathbf{J}]].\hat{k} ds. \tag{3.5.3}$$

Rate of change of potential energy

The total energy, $\mathcal{E}$ is given by the Helmholtz potential, $W(\nabla\mathbf{p}, \mathbf{p}, \rho, \nabla u)$ and the electrostatic energy

$$\mathcal{E} = \int_{\Omega\setminus C_\delta} W(\nabla\mathbf{p}, \mathbf{p}, \rho, \nabla u) dx + \int_{\mathbb{R}^3} \frac{1}{2}\epsilon_o |\nabla\phi|^2 dx. \tag{3.5.4}$$

Using the transport theorem (A.3.3), the rate of change of Helmholtz potential of the ferroelectric can be written as

$$\frac{d}{dt}\int_{\Omega\setminus C_\delta} W dx = \int_{\Omega\setminus C_\delta} \dot{W} dx - \int_{\partial C_\delta} W(\mathbf{v}.\hat{n}) ds, \tag{3.5.5}$$

where $\mathbf{v}$ represents the velocity of the contour ∂C_δ.

Upon using the chain rule and divergence theorem (A.3.6), (3.5.5) reduces to

$$\begin{aligned}\frac{d}{dt}\int_{\Omega\setminus C_\delta} W\,dx = &\int_{\Omega\setminus C_\delta}\left(\left\{-\nabla.\Big(\frac{\partial W}{\partial\nabla\mathbf{p}}\Big)+\frac{\partial W}{\partial\mathbf{p}}\right\}\dot{\mathbf{p}}-\nabla.\frac{\partial W}{\partial\epsilon}.\dot{\mathbf{u}}+\frac{\partial W}{\partial\rho}\dot{\rho}\right)dx\\ &+\int_{\partial\Omega}\left\{\frac{\partial W}{\partial\nabla\mathbf{p}}.\dot{\mathbf{p}}+\frac{\partial W}{\partial\epsilon}\dot{\mathbf{u}}\right\}\hat{m}ds+\int_\Gamma\left\{[[\frac{\partial W}{\partial\nabla\mathbf{p}}.\dot{\mathbf{p}}]]+[[\frac{\partial W}{\partial\epsilon}\dot{\mathbf{u}}]]\right\}\hat{k}ds\\ &-\int_{\partial C_\delta}\left\{\frac{\partial W}{\partial\nabla\mathbf{p}}.\dot{\mathbf{p}}+\frac{\partial W}{\partial\epsilon}\dot{\mathbf{u}}+Wv\right\}\hat{n}ds. \qquad (3.5.6)\end{aligned}$$

Rate of change of electrostatic energy

The electrostatic energy is a non-local quantity spread over the entire space. So its rate of change with the variation of fields inside the ferroelectric is derived in multiple steps as follows. The derivation closely follows [120] accounting for the presence of the crack.

Step-1: Using the weak form of Maxwell's equation.

The Maxwell's equation subject to boundary conditions

$$\begin{aligned}\nabla.(-\epsilon_o\nabla\phi+\mathbf{p}\chi_\Omega)&=\rho\chi_\Omega, \qquad (3.5.7)\\ \phi&=\hat{\phi}\quad\text{on}\quad\mathcal{S}_v,\\ \phi&\to 0\quad\text{as}\quad|\mathbf{x}|\to\infty,\end{aligned}$$

can be written in the weak form as

$$\begin{aligned}\int_{\mathbb{R}^3\setminus C_\delta}\epsilon_o|\nabla\phi|^2dx=&\int_{\Omega_\delta}(\mathbf{p}.\nabla\phi+\rho\phi)dx+\int_{\partial C}\phi.(-\epsilon_o\nabla\phi+\mathbf{p}).\hat{n}ds+\int_{S_v}\hat{\phi}\sigma ds+\int_{\partial C_q}\phi\sigma ds\\ &-\int_\Gamma[[\phi.(-\epsilon_o\nabla\phi+\mathbf{p})]].\hat{k}ds \qquad (3.5.8)\end{aligned}$$

where we assume that there is no crack opening under the linearized kinematics assumption.

The rate of change of (3.5.8) is given by

$$\frac{d}{dt}\int_{\mathbb{R}^3\backslash C_\delta}\epsilon_o|\nabla\phi|^2dx = \int_{\Omega_\delta}(\dot{\mathbf{p}}\nabla\phi+\mathbf{p}\dot{\nabla}\phi+\dot{\rho}\phi+\rho\dot{\phi})dx-\int_{\partial C}(\mathbf{p}.\nabla\phi+\rho\phi)v.\hat{n}ds$$
$$+\frac{d}{dt}\int_{\partial C}\phi.(-\epsilon_o\nabla\phi+\mathbf{p}).\hat{n}ds+\hat{\phi}\frac{d}{dt}\int_{S_v}\sigma ds$$
$$-\frac{d}{dt}\int_{\Gamma}[[\phi.(-\epsilon_o\nabla\phi+\mathbf{p})]].\hat{k}ds. \tag{3.5.9}$$

Note that the electric displacement is given by $\mathbf{D}=-\epsilon_o\nabla\phi+\mathbf{p}$. So all the above equations can be written in terms of $\mathbf{D}$.

Step 2: Using Reynolds transport theorem

Multiplying both sides of (3.5.7) by $\dot{\phi}$ and integrating over $\mathbb{R}^3\backslash C_\delta$ yields

$$\int_{\mathbb{R}^3\backslash\Omega_\delta}\epsilon_o\nabla\phi.\nabla\dot{\phi}dx=\int_{\Omega_\delta}\{\nabla\dot{\phi}\mathbf{p}+\rho\dot{\phi}\}dx+\int_{\partial C_q}\sigma\dot{\phi}dx+\int_{S_v}[[\dot{\phi}(-\epsilon_o\nabla\phi+\mathbf{p})]]\hat{m}ds$$
$$+\int_{\partial C}\dot{\phi}(-\epsilon_o\nabla\phi+\mathbf{p}).\hat{n}ds-\int_{\Gamma}[[\dot{\phi}(-\epsilon_o\nabla\phi+\mathbf{p})]].\hat{k}ds+\int_{S_v}[[\dot{\phi}(-\epsilon_o\nabla\phi+\mathbf{p})]]\hat{n}ds. \tag{3.5.10}$$

The rate of change of electrostatic energy

$$\frac{d}{dt}\int_{\mathbb{R}^3\backslash C_\delta}\frac{\epsilon_o}{2}|\nabla\phi|^2dx=\int_{\Omega_\delta}\{\rho\dot{\phi}+\dot{\nabla}\phi\mathbf{p}\}dx+\int_{\partial C}\dot{\phi}(-\epsilon_o\nabla\phi+\mathbf{p})ds-\int_{\Gamma}[[\dot{\phi}(-\epsilon_o\nabla\phi+\mathbf{p})]]\hat{k}ds$$
$$-\int_{\partial C}\frac{\epsilon_o}{2}|\nabla\phi|^2(\mathbf{v}.\hat{n})ds. \tag{3.5.11}$$

Subtracting (3.5.11) from (3.5.9) we have

$$\frac{d}{dt}\int_{\mathbb{R}^3\backslash C_\delta}\frac{\epsilon_o}{2}|\nabla\phi|^2dx=\int_{\Omega_\delta}(\dot{\rho}\phi+\dot{\mathbf{p}}\nabla\phi)dx-\int_{\partial C}\{(\mathbf{p}\nabla\phi+\rho\phi)v.\hat{n}+\dot{\phi}(-\epsilon_o\nabla\phi+\mathbf{p}).\hat{n}\}ds$$
$$+\frac{d}{dt}\int_{\partial C}\phi(-\epsilon_o\nabla\phi+\mathbf{p}).\hat{n}ds+\int_{\partial C}\frac{\epsilon_o}{2}|\nabla\phi|^2(v.\hat{n})ds+\hat{\phi}\frac{d}{dt}\int_{S_v}\sigma ds$$
$$-\frac{d}{dt}\int_{\Gamma}[[\phi(-\epsilon_o\nabla\phi+\mathbf{p})]].\hat{k}ds+\int_{\Gamma}[[\dot{\phi}(-\epsilon_o\nabla\phi+\mathbf{p})]].\hat{k}ds. \tag{3.5.12}$$

Thus we have the rate of change of electrostatic energy over all space.

Crack tip

We follow [42] and assume that the crack tip fields remain self-similar as the crack propagates. So the rate of change of a field quantity, say $\mathbf{A}$, along ∂C_δ is given by

$$\dot{A} = -\nabla A.\mathbf{v}, \tag{3.5.13}$$

where $\mathbf{v}$ is the velocity of the contour ∂C which in this case is the crack tip velocity, $\mathbf{v} = a\hat{t}$, as the contour ∂C_δ moves with the crack.

Substituting the expressions for the respective terms in the dissipation inequality (3.5.1) gives

$$\begin{aligned}
\mathcal{D} = &\int_{\Omega_\delta} \left(\nabla.\Big(\frac{\partial W}{\partial \nabla \mathbf{p}}\Big) - \frac{\partial W}{\partial \mathbf{p}} - \nabla\phi \right) \dot{\mathbf{p}} dx - \int_{\partial\Omega} \Big(\frac{\partial W}{\partial \nabla \mathbf{p}}\Big) \dot{\mathbf{p}} ds \\
&+ \int_{\Omega_\delta} \nabla.\Big(\frac{\partial W}{\partial \epsilon}\Big).\dot{\mathbf{u}} dx + \int_{\partial\Omega_t} \{\mathbf{t} - \frac{\partial W}{\partial \epsilon}\}.\hat{m}.\dot{\mathbf{u}} ds \\
&+ \int_{\Omega_\delta} (\mu - \frac{\partial W}{\partial \rho} - \phi)\dot{\rho} dx + \int_{\Omega_\delta} -\nabla\mu.\mathbf{J} dx \\
&+ \int_\Gamma \Big\{ [[\mu.\mathbf{J}]] - [[\frac{\partial W}{\partial \nabla \mathbf{p}}\dot{\mathbf{p}}]] - [[\frac{\partial W}{\partial \epsilon}]].\dot{\mathbf{u}} - [[\dot{\phi}(-\epsilon_o \nabla\phi + \mathbf{p})]] \Big\}.\hat{k} ds + \frac{d}{dt}\int_\Gamma [[\phi(-\epsilon_o\nabla\phi + \mathbf{p})]].\hat{k} ds \\
&+ \int_{\partial C} -\mu\mathbf{J}.\hat{n} ds - \frac{d}{dt}\int_{\partial C} \phi(-\epsilon_o\nabla\phi + \mathbf{p}).\hat{n} ds \\
&+ \int_{\partial C} \left\{ \Big(W - \frac{\epsilon_o}{2}|\nabla\phi|^2 + \mathbf{p}.\nabla\phi + \rho\phi\Big)\mathbf{v} - \frac{\partial W}{\partial \nabla \mathbf{p}}.(\nabla\mathbf{p}.\mathbf{v}) - \frac{\partial W}{\partial \epsilon}(\nabla\mathbf{u}.\mathbf{v}) - (-\epsilon_o\nabla\phi + \mathbf{p})(\nabla\phi.\mathbf{v}) \right\}.\hat{n} ds.
\end{aligned} \tag{3.5.14}$$

3.5.3 Governing equations

Based on Colemann and Noll [22] and self similarity argument, we conclude that the equations governing the equilibrium configuration of the ferroelectric are as follows

$$\nabla.\left(\frac{\partial W}{\partial \nabla \mathbf{p}}\right) - \frac{\partial W}{\partial \mathbf{p}} - \nabla\phi = 0 \quad \text{in} \quad \Omega, \tag{3.5.15}$$

$$\left(\frac{\partial W}{\partial \nabla \mathbf{p}}\right).\hat{m} = 0 \quad \text{on} \quad \partial\Omega \quad \& \quad \Gamma, \tag{3.5.16}$$

$$\nabla.\left(\frac{\partial W}{\partial \varepsilon}\right) = 0 \quad \text{in} \quad \Omega, \tag{3.5.17}$$

$$\left(\frac{\partial W}{\partial \varepsilon}\right).\hat{m} = \mathbf{t} \quad \text{on} \quad \partial\Omega_t, \tag{3.5.18}$$

$$\frac{\partial W}{\partial \rho} - \mu + \phi = 0 \quad \text{in} \quad \Omega. \tag{3.5.19}$$

The first two equation govern the polarization equilibrium and a boundary condition for polarization, the next two govern the mechanical equilibrium and the mechanical boundary condition, and the last equation governs the distribution of space charge at equilibrium. The polarizarion equation, (3.5.15) can be modified to account for the evolution of polarization. The resulting equation is of the form

$$\mu\dot{\mathbf{p}} = \nabla.\left(\frac{\partial W}{\partial \nabla \mathbf{p}}\right) - \frac{\partial W}{\partial \mathbf{p}} - \nabla\phi. \tag{3.5.20}$$

Since dissipation is semi-positive definite, we make the constitutive assumption that the flux of the space charge depends on the the chemical potential, μ, as follows

$$\mathbf{J} = -\mathbf{K}\nabla\mu, \tag{3.5.21}$$

where $\mathbf{K}$ is the diffusion constant. Typically the value of $\mathbf{K}$ would be different for different charge species. This formulation can easily be extended to that case by defining a flux term independently for each species. [107]. Note that at equilibrium the flux of space charge $\mathbf{J}$ is zero inside the specimen and on its boundary. The diffusion of space charge based on the

mass conservation statement and (3.5.21), is dictated by

$$\dot{\rho} = -\nabla.\mathbf{J} = \nabla.\Big(\mathbf{K}\nabla\mu\Big). \tag{3.5.22}$$

Using the crack tip velocity for $v = a\hat{t}$, we get the term conjugate to the crack tip velocity which represents the driving force on the crack

$$\int_{\partial C} \hat{t}.\left\{\left(W - \frac{\epsilon_o}{2}|\nabla\phi|^2 + \mathbf{p}.\nabla\phi + \rho\phi\right) - (\nabla\mathbf{p})^T.\frac{\partial W}{\partial\nabla\mathbf{p}} - (\nabla\mathbf{u})^T.\frac{\partial W}{\partial\epsilon} - \nabla\phi\otimes(-\epsilon_o\nabla\phi + \mathbf{p})\right\}.\hat{n}ds. \tag{3.5.23}$$

Note that if we neglect all the electrical quantities the above integral represents the usual mechanical form of the driving force on a crack - the J-integral. The additional terms are contributions from the polarization, space charge and electric field density set up by the polarization and the space charge. We discuss this contour integral further and make use of this expression later on to evaluate the driving force on the cracks and use it to study the effect of electric fields on the toughness of ferroelectrics.

3.5.4 Crack surface boundary conditions

The boundary conditions prescribed on the crack face have a significant influence on the domain formation around the crack and the influence of external fields on the crack driving force. The effect on driving force is clearly illustrated in the linear theory of piezoelectric fracture which has been widely discussed in the literature [125, 80, 29, 106, 67]. Here we discuss how the various boundary conditions prevalent can be naturally deduced from our dissipation inequality formulation. Consider the terms in 3.5.14 defined on the crack faces,

$$\int_\Gamma \left\{[[\mu.\mathbf{J}]] - [[\frac{\partial W}{\partial\nabla\mathbf{p}}\dot{\mathbf{p}}]] - [[\frac{\partial W}{\partial\epsilon}]].\dot{\mathbf{u}} - [[\dot{\phi}(-\epsilon_o\nabla\phi + \mathbf{p})]]\right\}.\hat{k}ds, \quad \text{and} \quad \frac{d}{dt}\int_\Gamma [[\phi(-\epsilon_o\nabla\phi + \mathbf{p})]].\hat{k}ds. \tag{3.5.24}$$

Based on our assumption that only the crack tip translates with the velocity $\mathbf{v} = a\hat{t}$ with the crack faces in the wake of the tip remaining stationary the second term in (3.5.24) goes to zero. The polarization term in the first integral is the natural boundary condition for polarization on the crack surface and can be set to zero. Next the flux term in the first

integral term represents the flux of space charges at the crack surfaces which reduces to zero if one assumes no leakage of the space charge into the crack, $\mathbf{J}.\hat{k} = 0$ on Γ.

The most frequently used boundary conditions in the literature can be deduced as follows

- *Insulating or Impermeable crack*: Proposed by Deeg [25], it assumes that he crack gap is impermeable and traction free expressed mathematically as

$$\mathbf{D}^+.\hat{k} = \mathbf{D}^-.\hat{k} = 0, \qquad \sigma^+.\hat{k} = \sigma^-.\hat{k} = 0. \tag{3.5.25}$$

  based on the above expressions all the terms in the first integral in (3.5.24) go to zero. The justification for this boundary condition is the large difference in the magnitude of permittivity between the crack gap medium and the surrounding ferroelectric.

- *Conducting or Permeable Crack*: This condition was introduced by Parton [80] based on the argument that there is no opening of crack in the linear theory and so the fields are continuous and the crack surfaces are traction free. This can be expressed as

$$\mathbf{D}^+.\hat{k} = \mathbf{D}^-.\hat{k}, \qquad \phi^+ = \phi^-, \qquad \sigma^+.\hat{k} = \sigma^-.\hat{k} = 0. \tag{3.5.26}$$

  based on the above expressions all the terms in the first integral in (3.5.24) reduce to zero.

- *Exact or Semi-Permeable conditions*: Introduced by Hao and Chen [109], this boundary condition seeks to address the fact the crack gap is actually open and the electric fields can permeate the crack gap which is assumed to have a permitivitty κ_c. The crack is assumed to be traction free. This can be expressed as

$$\mathbf{D}^+.\hat{k} = \mathbf{D}^-.\hat{k} = -\kappa_c \frac{\phi^+ - \phi^-}{u_2^+ - u_2^-}. \tag{3.5.27}$$

  Under these conditions the terms in (3.5.24) go to zero, with an additional condition on $\mathbf{D}^+.\hat{k}$ and $\mathbf{D}^+.\hat{k}$. Note that this condition makes the system of equations to be solved for non-linear. Though this condition seems physically accurate McMeeking [68] showed that the traction free condition leads to a discrepancy since in the presence

of an electric field in the open crack gap leads to a traction on the crack surface. Our formulation also reveals this if we consider crack opening and finite kinematics as we show in the next condition.

- *Energetically consistent boundary Conditions*: These conditions were introduced by Landis [60] to rectify the discrepency pointed out in the semi-permeable conditions by McMeeking [68]. The crack gap is assumed to have an electric enthalpy, $h_c(\mathbf{E}_c)$, which depends on the crack gap electric field, $\mathbf{E_c}$. The conditions on the crack are specified as

$$\mathbf{D}^+.\hat{k} = \mathbf{D}^-.\hat{k} = \frac{dh_c}{d\mathbf{E}_c}.\hat{k}, \qquad \sigma.\hat{k} = h_c\hat{k} + \mathbf{E}_c(\mathbf{D}_c.\hat{k}). \tag{3.5.28}$$

The derivation for the rate of dissipation (3.5.14) was derived assuming linearized kinematics. If that assumption is relaxed, following [120] one write

$$\int_\Gamma [[\dot{\phi}(-\epsilon_o\nabla\phi + \mathbf{p})]].\hat{k}ds = \int_\Gamma \dot{\phi}[[\mathbf{D}.\hat{k}]]ds + \int_\Gamma [[\mathbb{T}_M.\hat{k}]].\dot{\mathbf{u}}ds, \tag{3.5.29}$$

where $\mathbb{T}_M$ represents the Maxwell's stress acting on the crack surface due to the electric field in the crack gap. So the boundary conditions on the crack yield

$$[[\sigma.\hat{k}]] = -[[\mathbb{T}_M.\hat{k}]] = h_c\hat{k} + \mathbf{E}_c(\mathbf{D}_c.\hat{k}) \qquad \mathbf{D}^+.\hat{k} = \mathbf{D}^-.\hat{k} = \frac{dh_c}{d\mathbf{E}_c}.\hat{k} \tag{3.5.30}$$

In conclusion we claim that all the boundary conditions used for studying fracture in electromechanical problems can be derived naturally from our dissipation inequality approach. The analysis shows that, if crack opening is considered and a finite permittivity is assumed for the crack gap, the semi-permeable, traction free condition is inconsistent since the crack surface experiences a traction due to the electric field inside the crack gap. This is rectified in the energetically consistent boundary conditions [60], which our formulation also reveals.

3.6 Constitutive relations

We assume that the free energy density of the ferroelectric $W(\mathbf{p}, \nabla\mathbf{p}, \varepsilon, \rho)$ can be written as

$$W(\mathbf{p}, \nabla\mathbf{p}, \varepsilon, \rho) = W_d(\nabla\mathbf{p}) + W_p(\mathbf{p}, \varepsilon) + W_\rho(\rho), \tag{3.6.1}$$

where the first term represents domain wall energy which penalizes abrupt changes in polarization (domain walls) , the second term is the classical Landau-Ginzburg energy density which penalizes polarization and strain away form the the spontaneous values and the third term represents the energy density due to the space charge.

Our material of choice is $BaTiO_3$, which undergoes a transformation from a cubic to a tetragonal unitcell, has four variants in the tetragonal phase in two dimensions. Here we povide a brief descitpion of the importat material paramenets chosen for our simulations. The choice closely parallels [120] and [126]. So for greater details the reader can refer to those works. The Landau-Ginzburg energy density $W_p(\mathbf{p}, \varepsilon)$, is a fourthorder polynomial has four wells, figure (3.11), the polarization space centred around the four variant states corresponding to polarization values : $\mathbf{p}$: $(p_s, 0), (-p_s, 0), (0, p_s), (0, -p_s)$, where $p_s = 0.26 C/m^2$ is the spontaneous value of the polarization density.

$$\begin{aligned} W_p(\mathbf{p}, \varepsilon) = {} & \frac{a_1}{2}(p_1^2 + p_2^2) + \frac{a_2}{4}(p_1^4 + p_2^4) + \frac{a_3}{2}p_1^2p_2^2 + \frac{a_4}{6}(p_1^6 + p_2^6) + \frac{a_5}{4}(p_1^4p_2^4) \\ & - \frac{b_1}{2}(\varepsilon_{11}p_1^2 + \varepsilon_{22}p_2^2) - \frac{b_2}{2}(\varepsilon_{11}p_2^2 + \varepsilon_{22}p_1^2) - b_3\varepsilon_{12}p_1p_2 \\ & + \frac{c_1}{2}(\varepsilon_{11}^2 + \varepsilon_{22}^2) + c_2\varepsilon_{11}\varepsilon_{22} + \frac{c_3}{2}\varepsilon_{12}^2. \end{aligned} \tag{3.6.2}$$

The domain wall energy is assumed to be of the form

$$W_d(\nabla\mathbf{p}) = \frac{a_o}{2}|\nabla\mathbf{p}|^2 = \frac{a_o}{2}\left(p_{1,1}^2 + p_{2,2}^2 + p_{1,2}^2 + p_{2,1}^2\right). \tag{3.6.3}$$

The values of the constants involved in the above equations will be listed in a later section.

Since we are considering time scales where there is no diffusion of defects and the space charge is assumed to be always in equilibrium - steady state for the ferroelectric- the chemical potential associated with the space charge (assumed to be the same for all charged species

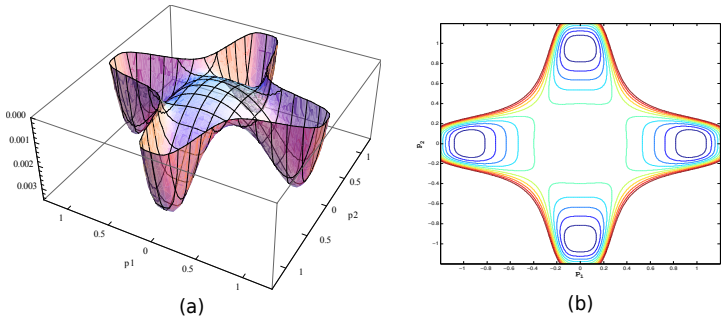

Figure 3.11: Landau-Ginzburg multiwell potential, W_p. (a) Four-well structure, (b) Contour plot of the wells.

i.e electrons holes and defects) at equilibrium is governed by

$$\nabla.(\mathbf{K}\nabla\mu) = 0 \qquad \text{in} \qquad \Omega. \tag{3.6.4}$$

This follows directly from (3.5.22) once the LHS is set to zero. If $\mathbf{K}$ is assumed to be isotropic and homogeneous the governing equation for the chemical potential reduces to

$$\nabla^2\mu = 0 \qquad \text{in} \qquad \Omega. \tag{3.6.5}$$

Since the flux of space charge on the boundary of the ferroelectric in contact with the surrounding insulating medium and the crack surface is zero we also have

$$\nabla\mu.\hat{m} = 0 \qquad \text{on} \qquad \partial\Omega/\partial\Omega_v \ \text{ and } \ \Gamma. \tag{3.6.6}$$

At equilibrium, the flux of the space charge is also zero on the part of the boundary in contact with the electrodes and the based on charge transport equations governing an metal-semiconductor interface, the chemical potential is given by

$$\mu = E_{fm} - e\hat{\phi} \ \text{ on } \ \partial\Omega_v, \tag{3.6.7}$$

where E_{fm} is the chemical potential or Fermi level of the metal electrode and $\hat{\phi}$ is the voltage the electrode is held at. In summary for a ferroelectric in contact with metal electrodes at equilibrium, the chemical potential of the space charge density is given by solving (3.6.4),

(3.6.6), (3.6.7). This is a clear departure from the methodology followed in [120], where μ was assumed to be constant over the ferroelectric domain and equal to the metal electrode fermi level, E_{fm}.

Consider the equation governing the space charge (3.5.19) at equilibrium

$$\frac{\partial W}{\partial \rho} - \mu + \phi = 0. \tag{3.6.8}$$

If μ is obtained from the procedure described above and W is assumed to be a convex function of ρ, the derivative in (3.5.19) can be inverted and ρ can be written as an explicit function of ϕ and μ. As was described in [6] , we use the typical charge density of a semiconductor at equilibrium, in contact with metal electrodes

$$\begin{aligned}\rho(\phi, N_d) = &-eN_c F_{\frac{1}{2}}\left(\frac{\mu - E_c + e\phi}{K_b T}\right) + eN_v F_{\frac{1}{2}}\left(\frac{E_v - e\phi - \mu}{K_b T}\right) \\ &+ eN_d(x)\left(1 - \frac{1}{1 + \frac{1}{2}exp(\frac{E_d - e\phi - \mu}{K_b T})}\right) \\ &- z'eN_a(x)\left(1 - \frac{1}{1 + \frac{1}{2}exp(\frac{\mu + e\phi - E_a}{K_b T})}\right),\end{aligned} \tag{3.6.9}$$

where μ is the chemical potential of the charge species,* N_c and N_v are the effective density of states of conduction and valence band respectively, E_c and E_v are the energies of the bottom of the conduction band and the top of the valence band respectively, E_a is the energy level of the acceptor dopant,E_d is the energy level of the donor dopants, K_b is the Boltzmann's constant, T is the temperature in Kelvin, $F_{\frac{1}{2}}$ is the Fermi-Dirac integral. We briefly explain the features of (3.5.19) which would help in understanding some of results we will present in the next section. Figures 3.12 and 3.13 show the plots of ρ vs ϕ. For values of $\phi < (E_v - \mu)/e$, due to the low value of ϕ, the electrons migrate out of the ferroelectric leaving behind a large density of holes in the valence band - the first term dominates. So the ferroelectric assumes a net positive charge density. For values of $\phi > (E_c - \mu)/e$, due to the large value of ϕ, electrons from the electrodes inject into the conduction band of the

*We adopt the popular convention used in solid-state physics of calling the Fermi-level the chemical potential, μ, which is uniform across the body for a species, where as the electrochemical potential, $\bar{\mu}$, is given by the chemical potential minus the local electrostatic potential, $\bar{\mu} = \mu - ez\phi$ [6]

ferroelectric resulting in a negative charge density - the second term dominates. For values of $(E_v - \mu)/e < \phi < (E_c - \mu)/e$, the space charge density is dominated by the dopants. The threshold value for the ionization of dopants is $\phi_c = (E_d - \mu)/e$. For $\phi < \phi_c$, the dopants are completely ionized, and all the electrons migrate out of the ferroelectric leaving it with a positive space charge density from the ionized dopants. In the results we are going to present though the space charge is mostly dominated by the ionized dopants, in certain regions of the ferroelectric like an insulated defect - due to the large values(in magnitude) of potential we do see the first and third term dominating. From here on we use (3.6.9) along with the Maxwell's equation, instead of (3.5.19), to determine the evolution and equilibrium state of the ferroelectric.

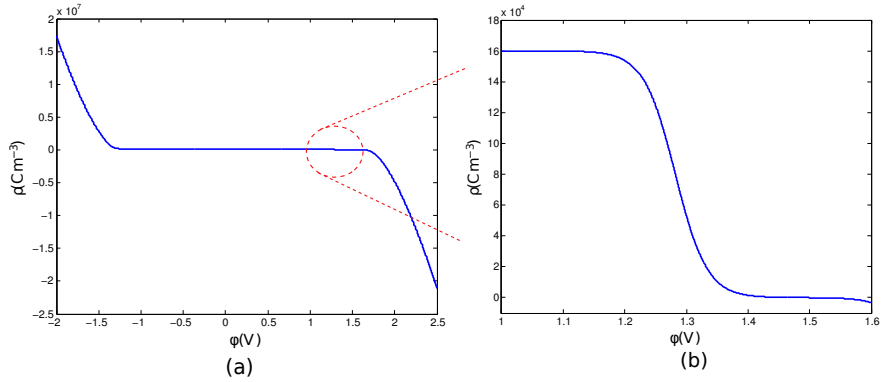

Figure 3.12: Variation of space charge density with electric potential at thermal equilibrium with n-type dopants, $T = 300K,\ N_d = 10^{24},\ N_a = 0, E_{fm} = -5.3eV$.

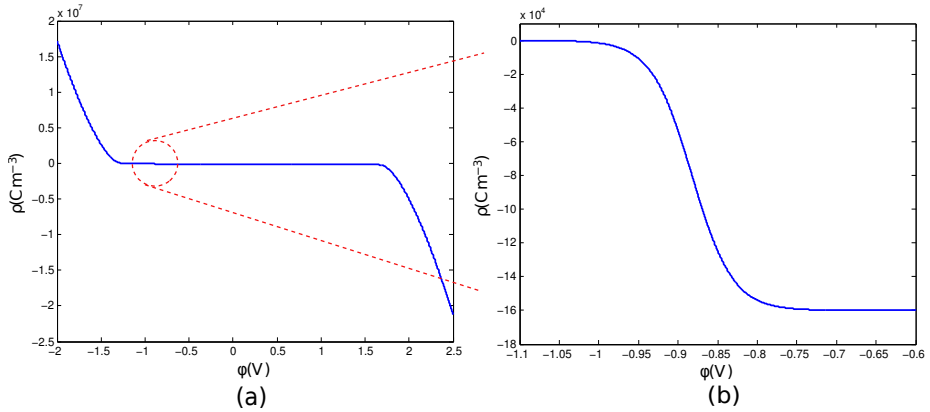

Figure 3.13: Variation of space charge density with electric potential at thermal equilibrium with p-type dopants, $T = 300K,\ N_a = 10^{24},\ N_d = 0, E_{fm} = -5.3eV$.

3.7 Implementation

We describe the procedure we adopt to solve the following set of equations which determine the evolution of polarization in a ferroelectric domain containing a crack and subject to electromechanical boundary conditions. In particular we are interested in the domain formation around the crack which plays a significant role in affecting the fracture toughness of ferroelectrics. Substituting the form of W, (3.6.1) and ρ, (3.6.9) into the equations (3.5.20),(3.5.17), (3.5.7) leads to

$$\mu\dot{\mathbf{p}} = a_o\Delta\mathbf{p} - \frac{\partial W_p}{\partial \mathbf{p}} - \nabla\phi, \tag{3.7.1}$$

$$\nabla.\left(\frac{\partial W_p}{\partial \varepsilon}\right) = 0, \tag{3.7.2}$$

$$\nabla.(-\epsilon_o\nabla\phi + \mathbf{p}) = \rho(\phi, N_d), \tag{3.7.3}$$

along with the following boundary conditions

$$\left(\frac{\partial W_p}{\partial \nabla\mathbf{p}}\right).\hat{m} = 0 \quad \text{on} \quad \partial\Omega \ \ \& \ \ \Gamma, \tag{3.7.4a}$$

$$\left(\frac{\partial W}{\partial \varepsilon}\right).\hat{m} = \mathbf{t} \quad \text{on} \quad \partial\Omega_t, \tag{3.7.4b}$$

$$\phi = \hat{\phi} \quad \text{on} \quad \partial\Omega_{\mathcal{S}}. \tag{3.7.4c}$$

We assume that the crack surfaces are traction free, $\sigma.\hat{k} = 0$ and insulated, $(-\epsilon_o\nabla\phi + \mathbf{p}).\hat{k} = 0$. The regions of the boundary where the electric potential is not specified are assumed to be free of surface charge , $(-\epsilon_o\nabla\phi + \mathbf{p}).\hat{m} = 0$. The above set of equations are non-dimensionalized using the parameters $c_o(N/m^2)$, $p_o(C/m^2)$, $L_o(m)$ representing stress or energy density, polarization density and length scale respectively. The normalized polarization density and length are $\mathbf{p}' = \frac{\mathbf{p}}{p_o}$, $\mathbf{x}' = \frac{\mathbf{x}}{L}$. Using these constants the energy

density could be expressed in non-dimensional form as

$$W'_d(\nabla \mathbf{p}) = W_d(\nabla \mathbf{p})/c_o = \frac{a'_o}{2}\left(p'^2_{1,1} + p'^2_{2,2} + p'^2_{1,2} + p'^2_{2,1}\right), \tag{3.7.5}$$

$$\begin{aligned} W'_p(\mathbf{p},\varepsilon) = W_p(\mathbf{p},\varepsilon)/c_o = {} & \frac{a'_1}{2}(p'^2_1 + p'^2_2) + \frac{a'_2}{4}(p'^4_1 + p'^4_2) + \frac{a'_3}{2}p'^2_1 p'^2_2 + \frac{a_4}{6}(p'^6_1 + p'^6_2) + \frac{a'_5}{4}(p'^4_1 p'^4_2) \\ & - \frac{b'_1}{2}(\varepsilon_{11}p'^2_1 + \varepsilon_{22}p'^2_2) - \frac{b'_2}{2}(\varepsilon_{11}p'^2_2 + \varepsilon_{22}p'^2_1) - b'_3\varepsilon_{12}p'_1 p'_2 \\ & + \frac{c'_1}{2}(\varepsilon^2_{11} + \varepsilon^2_{22}) + c'_2\varepsilon_{11}\varepsilon_{22} + \frac{c'_3}{2}\varepsilon^2_{12}, \end{aligned} \tag{3.7.6}$$

where $a'_o = a_o p_o^2/c_o L_o^2$, $a'_1 = a_1 p_o^2/c_o$, $a'_2 = a_2 p_o^4/c_o$, $a'_4 = a_4 p_o^6/c_o$, $a'_5 = a_5 p_o^8/c_o$; $b'_j = b_j p_o^2/c_o$ and $c'_j = c_j/c_o$, $j = 1, 2, 3$; $p'_{i,j} = \partial p'_i/\partial x'_j$. Since the typical elastic modulii are of the order of GPa, we choose $c_o = 1GPa$ and $L_o = p_o\sqrt{a_o/c_o}$ so that $a'_o = 1$. The parameter a_o determines the width of the domain wall. This choice of $a'_o = 1$, has the result of making the normalized classical solution (without defects) independent of the choice of a_o. We use two values of for $a_o = 10^{-9}Vm^3C^{-1}$ corresponding to $L_o = 0.26nm$and $a_o = 10^{-7}Vm^3C^{-1}$ corresponding to $L_o = 2.6nm$. This choice of parameters results in the following values for the material constants [126, 120] : $c'_1 = 185,\ c'_2 = 111,\ c'_3 = 74,\ b'_1 = 1.4282, b'_2 = -0.185, b'_3 = 0.5886, a'_1 = -0.007, a'_2 = -0.009, a'_3 = 0.003, a'_4 = 0.0261, a'_5 = 5$. For this choice of parameters the spontaneous strain corresponding to the variants can be expressed in terms of the normalized polarizations

$$\varepsilon_s = \begin{pmatrix} a'p'^2_x + b'p'^2_y \\ b'p'^2_x + a'p'^2_y \\ c'p_x{}'p'_y \end{pmatrix}, \tag{3.7.7}$$

where $a' = 0.0065,\ b' = -0.0044,\ c' = 0.0109$. Having established the normalized energy densities, we present the normalized form of 3.7.1 that will be used in the computation. Let $\phi' = \phi/\phi_o,\ \rho' = \rho/\rho_o,\ t' = t/T_o$ be the non-dimensional quantities corresponding to electric

potential, space charge density and time. The normalized equations take the form

$$\frac{\mu p_o^2}{T_o c_o}\frac{\partial \mathbf{p}'}{\partial t'} = a_o'\Delta'\mathbf{p}' - \frac{\partial W_p'}{\partial \mathbf{p}'} - \frac{\phi_o p_o}{L_o c_o}\nabla\phi, \tag{3.7.8a}$$

$$\nabla'.\left(\frac{\partial W_p'}{\partial \varepsilon}\right) = 0, \tag{3.7.8b}$$

$$\nabla'.(-\frac{\epsilon_o\phi_o}{L_o p_o}\nabla'\phi' + \mathbf{p}') = \frac{L_o\rho_o}{p_o}\rho'(\phi', N_d). \tag{3.7.8c}$$

Upon choosing $\phi_o = \frac{L_o c_o}{p_o},\ \rho_o = \frac{p_o}{L_o},\ T_o = \frac{\mu p_o^2}{c_o}$ the above equations reduce to their final form

$$\mu'\frac{\partial \mathbf{p}'}{\partial t'} = a_o'\Delta'\mathbf{p}' - \frac{\partial W_p'}{\partial \mathbf{p}'} - \nabla\phi, \tag{3.7.9a}$$

$$\nabla'.\left(\frac{\partial W_p'}{\partial \varepsilon}\right) = 0, \tag{3.7.9b}$$

$$\nabla'.(-\epsilon'\nabla'\phi' + \mathbf{p}') = \rho'(\phi', N_d), \tag{3.7.9c}$$

with $\mu' = 1$ and $\epsilon' = \frac{\epsilon_o c_o}{p_o^2}$ and

$$\begin{aligned}\rho'(\phi, N_d) = \frac{1}{\rho_o}\Big\{ &- eN_c F_{\frac{1}{2}}\left(\frac{E_{fm} - E_c + e\phi_o\phi'}{K_b T}\right) + eN_v F_{\frac{1}{2}}\left(\frac{E_v - e\phi_o\phi' - E_{fm}}{K_b T}\right) \\ &+ eN_d(x)\left(1 - \frac{1}{1 + \frac{1}{2}exp(\frac{E_d - e\phi_o\phi' - E_f m}{K_b T})}\right) \\ &- z' eN_a(x)\left(1 - \frac{1}{1 + \frac{1}{2}exp(\frac{E_{fm} + e\phi_o\phi' - E_a}{K_b T})}\right)\Big\}.\end{aligned} \tag{3.7.10}$$

For the following choice of characteristic constants

$$c_o = 1 \text{ GPa},\quad p_o = 0.26\ C/m^3,\quad a_o = 10^9\ Vm^3C^{-1}, \tag{3.7.11}$$

the dimensional constants take the values

$$L_o = p_o\sqrt{\frac{a_o}{c_o}} = 0.26\ nm,\quad \phi_o = \sqrt{a_o c_o} = 1V,\quad \rho_o = \sqrt{\frac{c_o}{a_o}} = 10^9\ C/m^3,\quad T_o = \frac{\mu p_o^2}{c_o}, \tag{3.7.12}$$

and material constants take the values

$$\mu' = 1, \quad \epsilon' = \frac{\epsilon_o c_o}{p_o^2} = 0.131. \tag{3.7.13}$$

Note the material constants, (3.7.13) are independent of value of a_o and so there is no explicit dependence of the normalized equations (3.7.9) on a_o except through length normalization and ρ'. So, as noted earlier, in charge free simulations, $\rho'(\phi') = 0$, the solution depends on the value of a_o only through L_o. In simulations including space charge however, the solution depends explicitly on a_o through ρ_o.

3.7.1 Finite element formulation

The normalized equations (3.7.9) along with the boundary conditions (3.7.4) are solved on a square domain containing a center crack using the Bubnov-Galerkin approximation method [45]. We describe the formulation of the weak form and the approximation of the solution with test functions and solution functions belonging to function space, H^1. This is because the highest order term in the weak form is first order in terms of the test and solution function. We formulate the implementation in terms of the normalized variables $\{\mathbf{p}, \mathbf{u}, \phi\}$ which are to be approximated in the calculation. Note that from here on we drop the primes (') used in the previous section to denote normalized quantities. All the equations listed from here are assumed to be in terms of non-dimensionalized quantities unless specified otherwise.

We begin by taking the inner product of the governing equation for evolution of polarization (3.7.9a) with a test function $\mathbf{q}$ giving us the weak form of (3.7.9a)

$$\int_\Omega \frac{\partial \mathbf{p}}{\partial t}.\mathbf{q}dx = -\int_\Omega \nabla \mathbf{p}.\nabla \mathbf{q}dx - \int_\Omega \frac{\partial W_p}{\partial \mathbf{p}}.\mathbf{q}dx - \int_\Omega \nabla \phi.\mathbf{q}dx, \tag{3.7.14}$$

where we used the divergence theorem. The boundary terms generated during the application of divergence theorem vanish due to the homogeneous Neumann boundary condition (3.7.4a) we adopt for p. This equation is the weak form of (3.7.9a). From the definition of weak form, the solution to this equation $\{\mathbf{p}, \phi\}$ is a function such that (3.7.15) is true

for all $\mathbf{q}$ belonging to the test fucntion space. Using an explicit scheme (Euler method) for discretizing in time [126], we get

$$\int_\Omega \frac{\mathbf{p}^{k+1}-\mathbf{p}^k}{\Delta t}.\mathbf{q}dx = -\int_\Omega \nabla \mathbf{p}^k.\nabla \mathbf{q}dx - \int_\Omega \left(\frac{\partial W_p}{\partial \mathbf{p}}\right)^k.\mathbf{q}dx - \int_\Omega \nabla \phi^k.\mathbf{q}dx. \tag{3.7.15}$$

Introducing the discretization where both the solution function and the test function are assumed to belong to the same space $\mathbf{p}^k = \sum_n \mathbf{p}_i^k N_i$, $\phi = \sum_n \phi_k N_k$, $\mathbf{q} = \sum_n \mathbf{q}_j N_j$, where $\{\mathbf{p}_i^k, \phi_k\}$ represent the nodal values of polarization and electric potential at a time t_k and N_i are the shape functions. The summation is over all the nodes. Substituting the approximations of $\mathbf{p}, \mathbf{q}, \phi$ into (3.7.15), yields the following system of equations corresponding to the two components of the polarization vector $\mathbf{p} = (p_1, p_2)$.

$$\mathbf{M}({p_i}^{(k+1)} - \mathbf{p_i}^k) = -\Delta t \left(\mathbf{K}.{p_i}^k + {b_i}^k + \mathbf{V}\phi^k\right) \qquad i = \{1,2\}, \tag{3.7.16}$$

where

$$\mathbf{M} = \int_\Omega N \otimes N dx \qquad M_{lm} = \int_\Omega N_l N_m dx, \tag{3.7.17a}$$

$$\mathbf{K} = \int_\Omega \nabla N \otimes \nabla N dx \qquad K_{lm} = \int_\Omega \nabla N_l.\nabla N_m dx, \tag{3.7.17b}$$

$${b_i}^k = \int_\Omega \frac{\partial W_p}{\partial p_i} N dx, \tag{3.7.17c}$$

$$\mathbf{V} = \int_\Omega \nabla N \otimes N dx \qquad V_{lm} = \int_\Omega \nabla N_l \otimes N_m dx, \tag{3.7.17d}$$

where $l, m = \{1,2\}$, p_i^k corresponds to the column vector of nodal values of the polarization component at time t_k, and ϕ^k is the column vector of nodal values of the electric potential at time t_k.

Following a similar procedure for the Maxwell's equation and taking an inner product with ψ and using the divergence theorem gives

$$\int_\Omega \epsilon \nabla\phi\nabla\psi dx + \int_\Omega \nabla.\mathbf{p}\psi dx - \int_\Omega \rho\psi dx = 0. \tag{3.7.18}$$

Note that the boundary conditions $(-\epsilon_o\nabla\phi + \mathbf{p}).\hat{m} = 0$ and $\phi = \hat{\phi}$ ensure that the boundary

terms go to zero. Substituting the approximations $\phi = \sum_n \phi_i N_i$, $\psi = \psi_j N_j$ and $\mathbf{p} = \sum_n \mathbf{p}_i N_i$ gives

$$\mathbf{K}.\phi + \mathbf{N}_1.p_1 + \mathbf{N}_2.p_2 - \mathbf{r} = 0, \tag{3.7.19}$$

where $\mathbf{K}$ is as defined in (3.7.17) and

$$\mathbf{N}_k = \int_\Omega N \otimes \frac{\partial N}{\partial x_1} dx \qquad [N_k]_{ij} = \int_\Omega N_i \frac{\partial N_j}{\partial x_1} dx \qquad k = 1, 2. \tag{3.7.20}$$

The mechanical equilibrium can similarly be formulated by establishing the weak form of (3.5.17)

$$\int_\Omega \nabla.\Big(\frac{\partial W_p}{\partial \epsilon}\Big).\mathbf{v} dx + \int_{\partial\Omega_t} (\mathbf{t}_o - \sigma.\hat{m}).\mathbf{v} dx = 0, \tag{3.7.21a}$$

which can be simplified further using the divergence theorem

$$-\int_\Omega \sigma \nabla \mathbf{v} dx + \int_{\partial\Omega_t} \mathbf{t}_o.\mathbf{v} dx = 0, \tag{3.7.22a}$$

where σ takes the following form

$$\begin{aligned}
\sigma_{11} &= \frac{\partial W_p}{\partial \varepsilon_{11}} = c_1\varepsilon_{11} + c_2\varepsilon_{22} - \frac{b_1}{2}p_1^2 - \frac{b_2}{2}p_2^2, \\
\sigma_{22} &= \frac{\partial W_p}{\partial \varepsilon_{22}} = c_1\varepsilon_{22} + c_2\varepsilon_{11} - \frac{b_1}{2}p_2^2 - \frac{b_2}{2}p_1^2, \\
\sigma_{12} = \sigma_{21} &= \frac{\partial W_p}{\partial \varepsilon_{12}} = c_3\varepsilon_{12} - 2b_3 p_1 p_2,
\end{aligned} \tag{3.7.23a}$$

$$\sigma = \mathbb{C}.\varepsilon - P = \begin{bmatrix} c_1 & c_2 & 0 \\ c_2 & c_1 & 0 \\ 0 & 0 & c_{12} \end{bmatrix} \begin{bmatrix} \varepsilon_{11} \\ \varepsilon_{22} \\ \varepsilon_{12} \end{bmatrix} - \begin{bmatrix} \frac{b_1}{2}p_1^2 + \frac{b_2}{2}p_2^2 \\ \frac{b_1}{2}p_2^2 + \frac{b_2}{2}p_1^2 \\ 2b_3 p_1 p_2 \end{bmatrix}. \tag{3.7.23b}$$

Substituting the approximation for $\mathbf{v} = \sum_n \mathbf{v}_i N_i$ and $\mathbf{u}_i = \sum_n \mathbf{u}_i N_i$, where $\mathbf{u}_i$ represents

the displacement vector at node i, gives

$$\mathbf{C}.\mathbf{u} - \mathbf{P} - \mathbf{T} = 0, \tag{3.7.24a}$$

$$\mathbf{C} = \int_{\Omega} B^T \mathbb{C} B \; dx \qquad \mathbf{T} = \int_{\partial\Omega_t} \mathbf{t}_o N \; ds \qquad \mathbf{P} = \int_{\Omega} B^T P dx \qquad \varepsilon = B.\mathbf{u}. \tag{3.7.24b}$$

To summarize, we have a system of equations to update the polarization, a system to find out the equilibrium electrostatic potential corresponding to the updated polarization, and a system to determine the equilibrium displacement and stress corresponding to the polarization update :

$$\mathbf{M}({p_i}^{(k+1)} - \mathbf{p_i}^k) = -\Delta t \left(\mathbf{K}.{p_i}^k + {b_i}^k + \mathbf{V}\phi^k\right) \qquad i = \{1, 2\}, \tag{3.7.25a}$$

$$\mathbf{K}.\phi^{(k+1)} + \mathbf{N}_1.p_1^{(k+1)} + \mathbf{N}_2.p_2^{(k+1)} - \mathbf{r}^{(k+1)} = 0, \tag{3.7.25b}$$

$$\mathbf{C}.\mathbf{u}^{(k+1)} - \mathbf{P}^{(k+1)} - \mathbf{T} = 0. \tag{3.7.25c}$$

A few comments. First, since we use an explicit scheme to update polarization, the time step Δt needs to be chosen so that the scheme are stable. We choose it such that it satisfies the stability condition $\Delta t \leq \frac{2}{\lambda_{max}}$, where λ_{max} is the largest eigen value of $\mathbf{M}^{-1}\mathbf{K}$. The value we use is $\Delta t = 0.05$. Second, the mesh should be fine enough to be able to resolve the crack tip stresses and the formation of domain walls. The typical width of the domain wall is of the order $\sim 5nm$ which is $\sim 20L_o$ in terms of the dimensional constant. So the mean element size is chosen such that the width of a domain wall is resolved by four elements. Third, the system of equations for electric potential (3.7.19), is a set of non-linear equations in ϕ due to the the non-linear nature of $\rho(\phi)$, (3.6.9). So we make use of a trust-region algorithm to find out the solution at each time step.

3.8 Results

The computations are carried over a square domain of size 1000×1000. The domain contains a center crack of length $l_c = 200$. The mesh and the boundary conditions used for the simulations are shown in Figure 3.14. The region around the crack tip is refined to

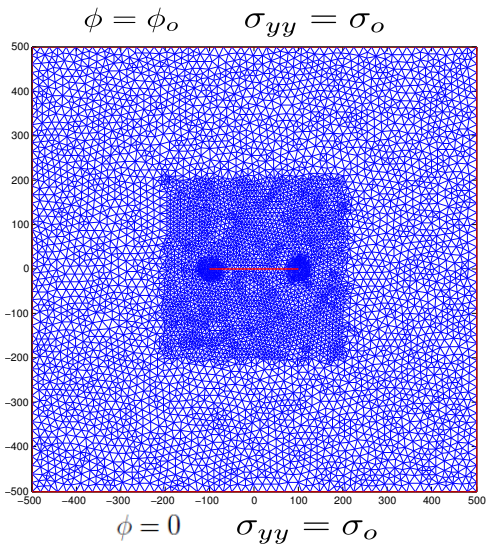

Figure 3.14: Mesh used for the simulations and boundary conditions.

resolve the stress and electric fields. The domain is in contact with electrodes on the top and bottom surfaces with the top electrode maintained at a potential ϕ_o and the bottom electrode is grounded. The rest of the boundary is assumed to be charge free, $\mathbf{D}.\hat{m} = 0$, since it is assumed to be in contact with an insulator. Tractions are applied on the top and bottom edges and the rest of the boundary is traction free. As mentioned earlier we use impermeable and traction free boundary conditions on the crack. We perform a mesh convergence study to ensure that the results presented here represent the converged solutions.

The results from the simulations are presented in this section. We have three different sets of results: (i) Simulations without any space charge. (ii) Simulations with n-type dopants. (iii) Simulations with p-type dopants. Before we begin we offer some perspective regarding some of the important parameters in the simulations.

1. Applied stress(σ_o): Typical non-dimensional value is 2.5, which corresponds to the stress which results in a stress intensity value of $2MPa\sqrt{m}$ which is the typical fracture toughness of $BaTiO_3$. We presents results for $\sigma_o = 0, 0.1$.

2. Applied potential (ϕ_o) : Typical non-dimensional value is 1.2, which corresponds to an electric field value of $3.7 \times 10^4 KV/m$ corresponding to 180^oswitching field of $BaTiO_3$.

We use values in the range $[-1 \;\; 1]$ for ϕ_o.

3. Dopant density (N_d or N_a) : Typical value is 10^{24} which corresponds to a low dopant density, see[94].

4. Specimen dimension (L_o) : In this simulation $L_o = 0.26nm$. We choose a specimen of edge size $1000L_o = 260nm$. This corresponds to a film of intermediate thickness [120].

3.8.1 No space charge, $\rho = 0$

First we present the case where we neglect the space charge density in the ferroelectric. We treat the ferroelectric as an insulator and observe the domain formation around the crack in a single crystal $BaTiO_3$, with the crack being normal to the poling direction. We start with the initial state with the polarization pointing upwards. The top electrode is maintained at $\phi = \phi_o$ and the top and bottom electrodes are subject to a tensile stress $\sigma_{yy} = \sigma_o$. We perform the simulation for $\sigma_o = 0, 0.1$ and $\phi_o = [-0.5, \;\; -0.1, \;\; 0, \;\; 0.1, \;\; 0.5]$ for each value of σ_o. Note that a positive (negative) value of ϕ_o corresponds to a nominal electric field pointing downwards(upwards) - anti-parallel(parallel) to the poling direction or known in the literature as a negative(positive) electric field.

The evolution of polarization starting from the initial uniformly poled state to the final polarization state is shown in Figure 3.15 through a series of intermediate states. These results correspond to $\phi_o = 0.1, \;\; \sigma_o = 0$. At $n = 0(t = 0)$, the initial state, the polarization in the crystal is uniform with $p_1 = 0, p_2 = 1$ and pointing upward. The crack is at the center of the square domain (not seen here). In this state the domain wall energy and the Devonshire-Ginzburg-Landau (DGL) energies are zero. However due to the insulated crack face boundary condition, this configuration is electrostatically unfavourable. So as time evolves we see the polarization vectors next to the crack surface starting to switch and become parallel to the crack surface. The 90^o switching results in formation of four symmetric domains around the crack. They start from the crack surface and evolve into the bulk. This 90^o domain formation is similar to that seen in the experiments of Jiang et.al [51],with a PMNT single crystal with a crack perpendicular to poling direction under the

influence of a negative external field, see Figure 3.5. The results for other values of ϕ_o (not displayed here) show that the 90^o domains formed are larger for a negative nominal field and the domains shrink in the case of a positive nominal field. This is anticipated since in the case of negative fields the polarization switches to a state perpendicular to applied field resulting in a lower electrostatic energy. However in the case of positive applied field the switching in undesirable since it increases the electrostatic energy compared to initial state. In the case with $\sigma_o = 0.1$ (not displayed here), the domain sizes are smaller since the tensile far field stress prefers the variant with the polarization vector aligned along the tensile stress axis.

The plots of equilibrium configurations of polarization $\mathbf{p}$, electric potential ϕ and yy-component of the stress, σ_{yy} are presented for the case where the external field is anti parallel to the poling direction $\phi_o = 0.1$ and the external tractions are zero, $\sigma_o = 0$, Figure 3.16. Note that the numerical values of all the quantities displayed in the plots are non-dimensional values. The polarization plot shows formation of four symmetrical domains due to 90^o switching as explained earlier. The stress field around the crack shows a concentration at the crack tip. Note that the specimen is free of external tractions and so the stress concentration arises purely from the switching of polarization. Finally the electric potential plot displays quite a remarkable result. It is interesting to note that the regions around the crack are the regions of highest electric potential compared to the rest of the ferroelectric - even higher than the 90^o domain walls. This in fact has also been observed in KFM experiments on a crack in single crystal $BaTiO_3$ of Sun et.al. [105], see Figure 3.6.

3.8.2 n-type dopants

Next we consider the case of ferroelectric perovskites with donor defects. Typically oxygen vacancies in perovskites act as donors. So ferroelectric crystals grown in an oxygen depleted environment act as n-type semiconductors due to the large number of oxygen vacancies. Here we consider a dopant density of $N_d = 10^{24}/m^3$. This corresponds to a low level of doping density [120, 94].

The results for the case with n-type dopants is presented in Figure 3.17. Note that

we use the same values, $\phi_o = 0.1, \sigma_o = 0$ as in the no space charge case to facilitate a comparison. The results in this case differ from those without any doping, Figure 3.16. Firstly the polarization domains around the crack are no longer symmetric, there is extensive switching above the crack with considerably less switching below it. In this case too the electric potential value in the region surrounding the crack has a value greater than in the other regions of the ferroelectric. The stress plot reveals a tensile stress concentration around the crack tip caused due to the switching. The space charge density plots reveal the build up of high space charge density around the crack. The peak value of the space charge density occurs at the crack tips, Figure 3.12. The region close to the crack tip is dominated by high space charge density of electrons and holes corresponding to the tails of the $\rho - \phi$ plot, Figure 3.12. This is due to the high values of electric potential which results in attracting electrons to regions of high positive electric potential and holes in regions of high negative potential.

3.8.3 p-type dopants

Next we present the results for the case where the dominant imperfections are p-type in nature. In perovskites positively charged cation impurities act as p-type dopants as discussed in Section 3.4. The results are presented in Figure 3.18. As in the n-type dopant case the polarization switching is no longer symmetric with extensive switching taking place below the crack. The electric potential distribution is similar to the case with n-type dopants with the region around the crack having the highest potential. Notice that even in this case the space charge density around the crack is dominated by the electron and hole contributions due to the large value of positive and negative potential around the crack tip. This value is much higher than the contribution from ionization of dopants which has a non-dimensional value $\rho_a = -1.6 \times 10^{-5}$.

3.8.4 Discussion

The peak value of the space charge density occurs at the crack tips with a positive value on the top crack surface and a negative value on the lower crack surface. This is anticipated

as the poling direction was initially pointing upwards which would have resulted in positive bound charge on the lower crack surface and a negative charge on the upper crack surface. If not compensated this would have led to an increase in the electrostatic energy of the system. In the first case where the ferroelectric is treated as an insulator, Figure 3.16, there is extensive 90^o polarization switching with the polarization orienting itself parallel to the crack surface and there by leaving the crack surface bound charge free . However in the other two cases where space charge was contributed by the semi-conducting nature of the ferroelectric, the bound charges on the crack surface are compensated by the space charge. This is the reason for limited switching in the latter two cases. It is also interesting to note that the nature of dopants does not effect the space charges around the crack.

Experiments where the electrostatic potential around the crack was measured in single crystal and poled polycrystal ferroelectrics with the poling direction normal to the crack, [105, 89, 30], speculate the accumulation of free charge along the crack surfaces. The above results from our simulations suggest that this indeed could be from space charges inside the ferroelectric which arise due to its semiconducting nature. A caveat regarding the direct comparison of these results with experiments is in order. Note that our simulation length scale is of the order of micrometers ($0.26\mu m$) where as the experiments are carried out with specimen sizes and observation scales of the order of $10\mu m$. Also note that the experiments of Schneider et.al [89] and Engert et.al [30] were done using poled polycrystals where as Sun et.al [105] used single crystal sample on the scale of millimeters. Due to this large disparity in the length scales the observations from these simulations, though qualitatively similar, shouldn't be directly compared with experiments. However we do note that these preliminary simulations reveal the accumulation of space charge due to the semiconducting nature and defect ionization around the crack which would result in increasing the permittivity of the gap. This offers a potential mechanism for the charges speculated to be build up on the crack surface. So this calls for extending these simulations to length scales comparable to those of experiments.

3.9 One-dimensional model

The results shown above in the case where the poling direction is normal to the crack orientation and the crack surface is insulated yields an equilibrium configuration where there is switching of polarization parallel to the crack and build up of space charge close to the crack surface, Figures 3.17 and 3.18. Here we present a simple 1-D model along the lines of [94] to explain these observations. We look at the region near the crack face, away from the crack tip, and the distant electrode. Let x denote the distance from the electrode held at fixed potential, $\phi = 0$ in this case and the crack surface. So this represents the bottom half of our simulation domain. The governing equations and the boundary conditions are summarized as follows:

$$a_o \frac{d^2p}{dx^2} - \frac{dW_p}{dp} - \frac{d\phi}{dx} = 0, \qquad \frac{dp}{dx} = 0 \quad \text{at} \quad x = 0, L, \tag{3.9.1}$$

$$-\epsilon \frac{d^2\phi}{dx^2} + \frac{dp}{dx} = \rho(\phi) \qquad \phi(0) = 0, \quad \Big(-\epsilon \frac{d\phi}{dx} + p \Big)\Big|_{x=L} = 0,$$

$$W_p = \frac{a}{2}(T - T_o)p^2 + \frac{b}{4}p^4 + \frac{c}{6}p^6. \tag{3.9.2}$$

with $\rho(\phi)$ being the same as (3.7.10). The constants used in the above equations are the same as in [94], corresponding to $BaTiO_3$. Like in the two dimensional case, W_p is polynomial in p having two local minima at $p = \pm 1$ and local maxima at $p = 0$ for $T < T_o$. The value $p = 0$ can be interpreted as the polarization undergoing a 90^o switch. We have not normalized the equations and so all the numbers in the solution plots, Figure 3.19, denote the actual physical values. Note that we have not included any mechanical displacement in the above formulation.

3.9.1 Results

We present the results for homogeneously doped n-type ($N_a = 0$) $BaTiO_3$ films. The above equations subject to the boundary conditions are solved using a finite difference method with a collocation formula. The results are presented for the parameters $L = 130, 200, 1000\ nm$ and $N_d = 10^{24}$ corresponding to films of different thicknesses at low doping concentration. We perform the simulations using Pt electrodes ($E_{fm} = -5.3eV$) and the temperature at T

= 300K. Since the equations we are solving involve potentials with multiple local minima, the solution we arrive at depends on the initial guess. We use the solutions presented in [94] as out initial guess.

Let us consider the case of low doping ($N_d = 10^{24}$) since that is the value we use in our two-dimensional simulations in Section 3.8. The results are shown in Figure 3.19. For thin films, we see that the film is fully depleted and all the dopants are ionized. The polarization takes a zero value at the insulated boundary, ($x = L$), and varies linearly around $p = 0.26$ in the film. This indicates that polarization undergoes switching close to the crack (insulated) surface (see Figure 3.17 for 2D case). The space charge density's variation is more interesting and contrasting from the regular case. While for most part of the film $\rho = 1.6 \times 10^{-3}$ corresponding to ionized donors, close to the insulated surface due to the negative value of ϕ it assumes a large positive value indicating a large concentration of holes in the valence band. So, close to the insulated surface the ferroelectric becomes conducting with holes being the majority carriers. Similar results are observed in the intermediate and thick film cases. Thus we have shown that such 1D models offer initial insight and capture most of the physics which can be corroborated subsequently through rigorous simulations in higher dimensions.

3.10 Driving force on the crack : The J-integral

Through the dissipation inequality approach we derived an expression for the thermodynamic quantity conjugate to crack growth - the crack driving force in the setting of a ferroelectric with space charge

$$J = \int_{\partial C} \hat{t}.\left\{\left(W - \frac{\epsilon_o}{2}|\nabla\phi|^2 + \mathbf{p}.\nabla\phi + \rho\phi\right) - (\nabla\mathbf{p})^T.\frac{\partial W}{\partial \nabla\mathbf{p}} - (\nabla\mathbf{u})^T.\frac{\partial W}{\partial \varepsilon} - \nabla\phi\otimes(-\epsilon_o\nabla\phi + \mathbf{p})\right\}.\hat{n}ds \tag{3.10.1}$$

Here we further discuss this quantity and draw a few parallels with what is popular in literature and also highlight the differences. Firstly the above contour integral can be written as

$$J = \int_{\partial C} \hat{t}.\mathbf{\Psi}.\hat{n}ds, \tag{3.10.2}$$

where

$$\begin{aligned}\boldsymbol{\Psi} &= \Big(W - \frac{\epsilon_o}{2}|\nabla\phi|^2 + \mathbf{p}.\nabla\phi + \rho\phi\Big)\mathbf{I} - (\nabla\mathbf{p})^T.\frac{\partial W}{\partial \nabla\mathbf{p}} - (\nabla\mathbf{u})^T.\frac{\partial W}{\partial \varepsilon} - \nabla\phi\otimes(-\epsilon_o\nabla\phi + \mathbf{p}) \\ &= H\mathbf{I} - (\nabla\mathbf{p})^T\frac{\partial H}{\partial \nabla\mathbf{p}} - (\nabla\mathbf{u})^T\frac{\partial H}{\partial \varepsilon} + \mathbf{E}\otimes\mathbf{D}. \qquad (3.10.3)\end{aligned}$$

We define the quantity, $\boldsymbol{\Psi}$, as the augmented material momentum tensor. It is the Eshelby energy momentum tensor with new terms to account for the polarization, space charge and electrostatics. The quantity, H, is popularly known as the electric enthalpy [103, 3] of the ferroelectric since it is defined as

$$H(\mathbf{p}, \nabla\mathbf{p}, \phi, \nabla\phi, \mathbf{u}) = W(\mathbf{p}, \nabla\mathbf{p}, \rho, \mathbf{u}) - \frac{\epsilon_o}{2}|\nabla\phi|^2 + \mathbf{p}.\nabla\phi + \rho\phi. \qquad (3.10.4)$$

If the $\nabla\mathbf{p}$ term is neglected in (3.10.3), it reduces to the material momentum tensor for electromechanics [106, 125, 77]. The material momentum tensor is a divergence free quantity in a defect free domain and so the contour integral using it becomes path independent under the impermeable and permeable crack surface boundary conditions. We later show that the augmented energy momentum tensor, due to the introduction of dependence of W on ρ, also turns out to be divergence free under equilibrium conditions. This result is an improvement to what Li and Landis [63] claim that the contour integral can not be path-independent if space charge is included even under equilibrium conditions.

Since an unstructured discretization is used around the crack, the crack driving force is not amenable for evaluation in the contour integral form. Instead we use the domain integral method to evaluate this quantity [95]. In the domain integral method the contour integral (3.10.1) is converted into an equivalent domain integral form by multiplying the integrand $\boldsymbol{\Psi}.\hat{n}$ with a weight function q which takes value 1 in an open domain surrounded by the contour Γ and a value zero on an outer contour. See Appendix A.7 for details.

The boundary conditions on the crack surfaces we use ensure that the integral terms along the crack surfaces drop out leaving just the domain integral which is evaluated using numerical quadrature.

3.10.1 Results of J-integral

Having established the formulation and methodology of computation, we evaluate the driving force on the cracks in the different scenarios we considered earlier i.e space-charge free, n-type dopant dominated specimen and p-type dominated specimen. The results are shown in Figures 3.20 and 3.21 for different levels of applied stress. Note that positive values ϕ_o correspond to a negative field and vice versa. The negative values of J are expected following the analysis of Haug and McMeeking [43] who showed that the energy release rate assumes a negative value when the remnant polarization is considered. The plots suggest that in the case with no space charge, the value of J increases with increasing strength of the negative applied field and decreases with increasing strength on positive field in the range of the values tested. The plots corresponding to cases with space charge show the inverse trend though with much weaker dependence. Also note that the value of J in the case with space charge is greater than in the case without the space charge. This is due to the screening of remnant polarization at the crack surface by the space charge. It is interesting to note that the nature of dopants does not seem to affect the trend. This is expected since much of the charge build up around the crack tip comes from the electronic charges and not the ionization of dopants.

Though the above mentioned trend in the case of with no space charge matches the trend suggested in [51], we are careful not to draw a direct parallel since the length scales are entirely different. The inclusion of the semiconducting nature certainly shows some influence on the driving force. This calls for including it in models trying to simulate crack tip zone processes in ferroelectrics and carry out a simulation at similar length scales.

3.11 Summary and conclusions

In this chapter we have considered the effect of including space charge arising from the semiconducting nature and ionization of defect dopants on fracture in ferroelectric perovskites. We do this by developing a phase field model of the ferroelectric including the space charge density. We start by invoking the dissipation of a ferroelectric domain containing a crack under the action of external fields and crack growth. This analysis results in establishing the

governing equations for the polarization, displacement and the electric potential along with the boundary conditions on the outer boundary of the ferroelectric domain. The analysis also gives a rigorous derivation for the driving force on the crack in the form of a contour integral which can be written in terms of the electric enthalpy density of the ferroelectric. We prove that the contour integral is contour independent under impermeable and permeable crack surface conditions unlike previously thought so [63] . This is a direct result of making the Helmhotz potential of the ferroelectric a function of the space charge. Also the various crack surface boundary conditions currently seen in literature can be naturally established from the dissipation analysis.

Next, adopting the phase field model to Barium Titanate we set up a finite element based simulation of polarization domain evolution around a center crack in a single crystal subject to electromechanical fields. The simulations reveal the accumulation of electronic charge at the crack surface. Recent experiments measuring the electric potential distribution around cracks in ferroelectric perovskites measure a high permittivity of the crack gap suggesting a build up of charge on the crack surface. These preliminary simulations suggest that the semiconducting nature and defect ionization could be a possible source of this charge build up. However a direct comparison with experiments at this stage is unwarranted due to the large difference in the length scales. This motivates the implementation of these simulations at length scales close to the experimental scale so a direct comparison could be made.

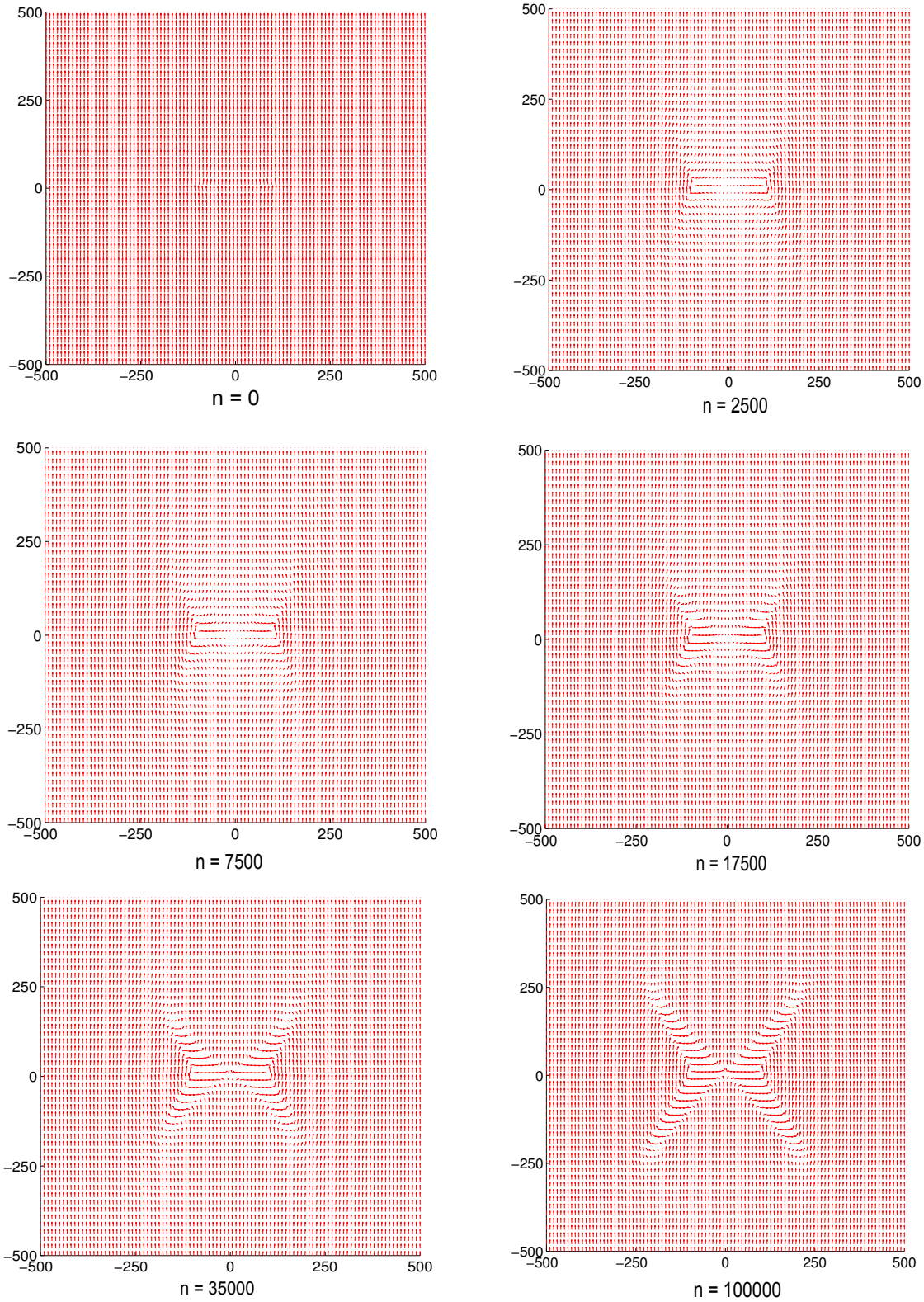

Figure 3.15: Polarization evolution for $\sigma_o = 0,\ \phi_o = 0.1$. n represents the time step.

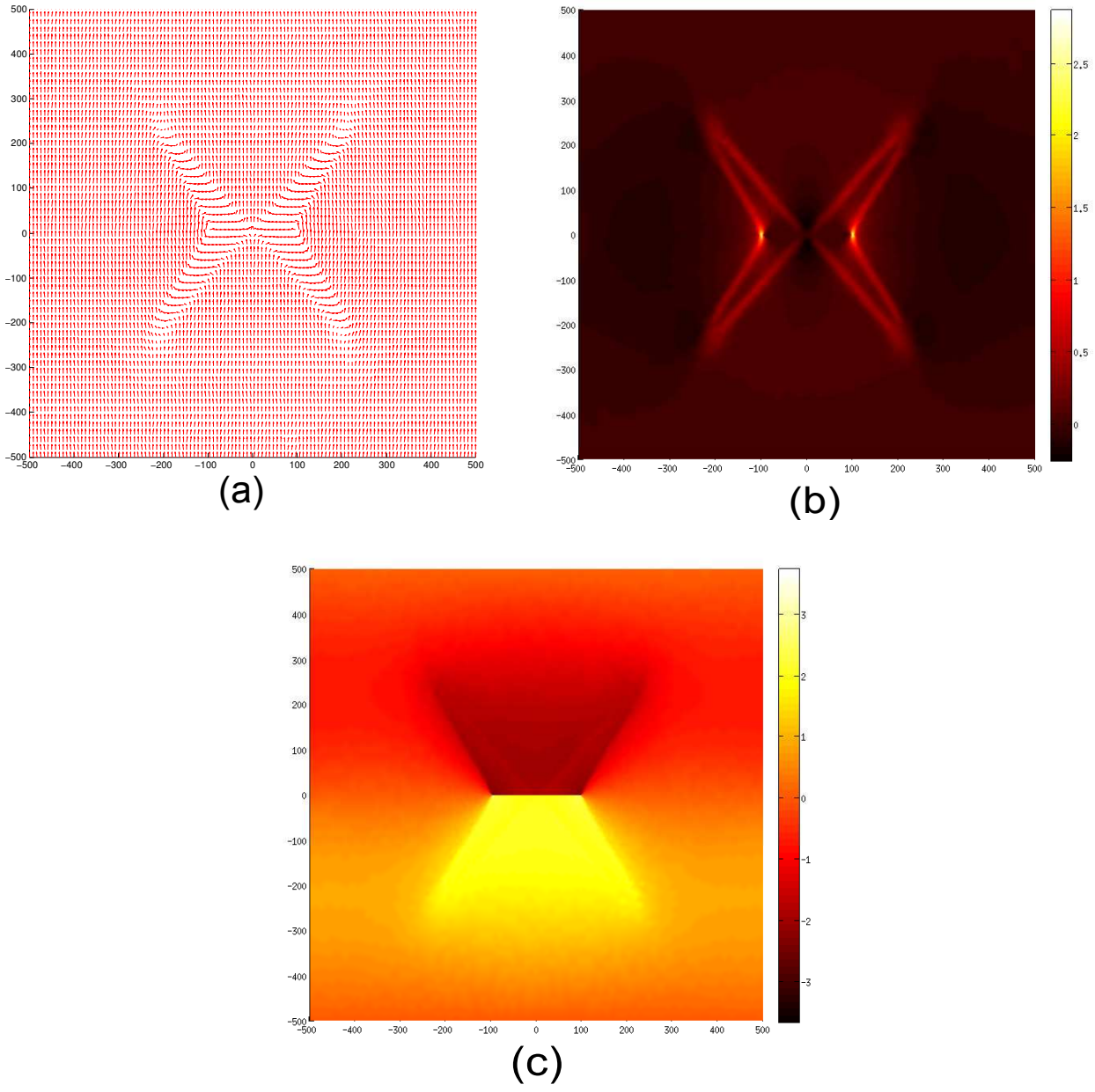

Figure 3.16: Results for $\sigma_o = 0,\ \phi_o = 0.1$. (a) Polarization domains around the crack, (b) σ_{22}, (c) Electric potential, ϕ.

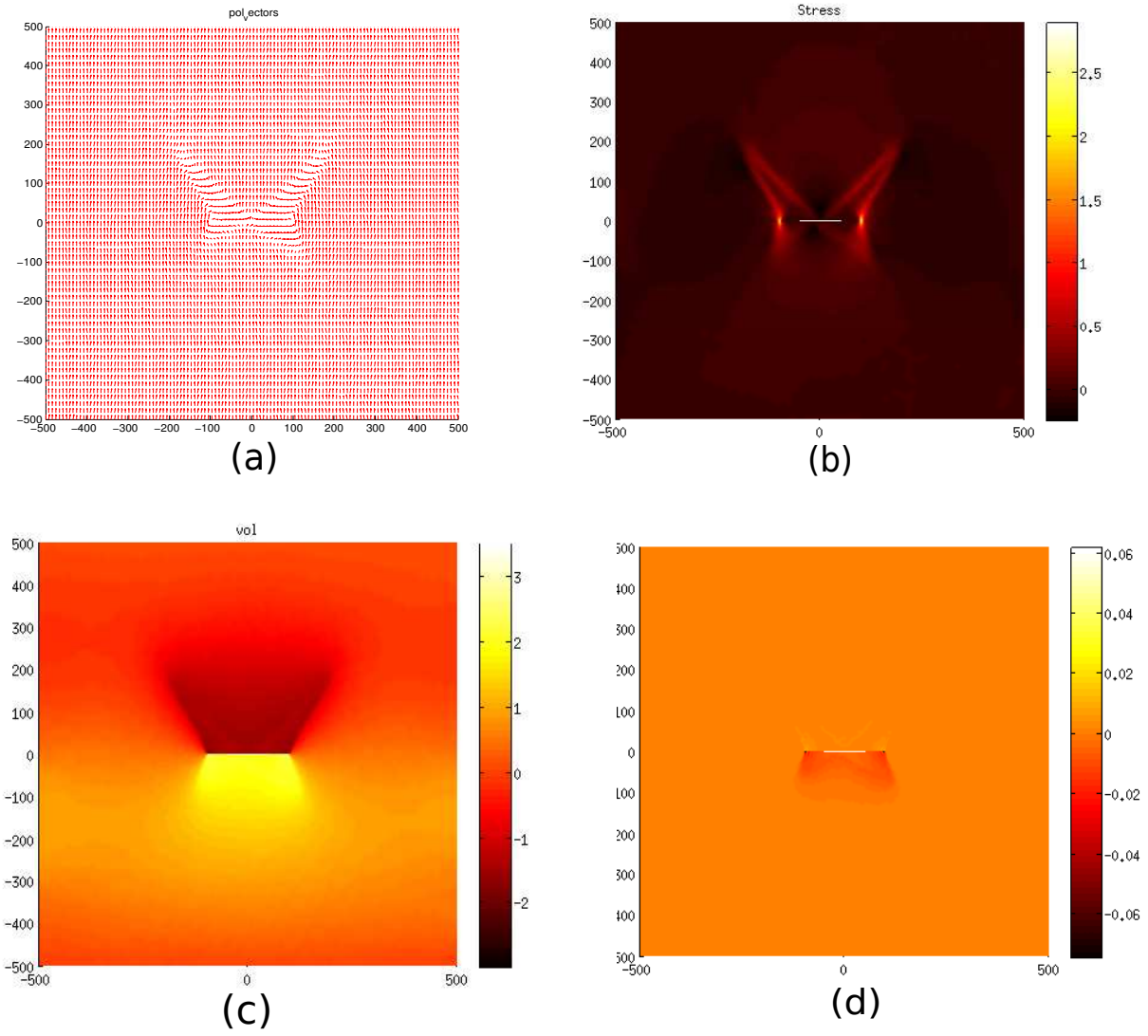

Figure 3.17: Results for n-type dopants at $\sigma_o = 0,\ \phi_o = 0.1,\ N_d = 10^{24}$ (a) Polarization domains around the crack, (b) σ_{22}, (c) Electric potential, ϕ, (d) Space Charge, ρ.

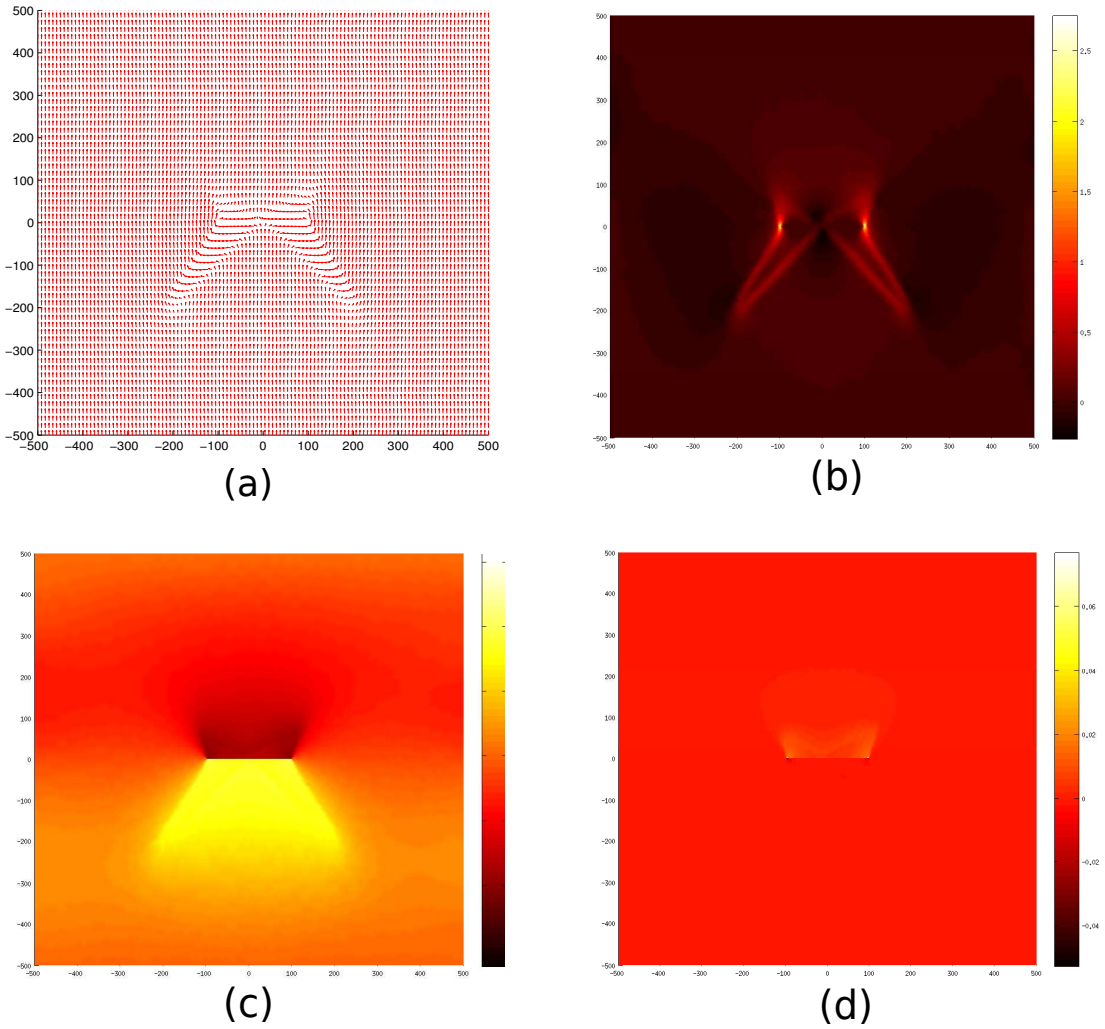

Figure 3.18: Results for p-type dopants at $\sigma_o = 0,\ \phi_o = 0.1,\ N_d = 10^{24}$. (a) Polarization domains around the crack, (b) σ_{22}, (c) electric potential, ϕ, (d) space charge, ρ.

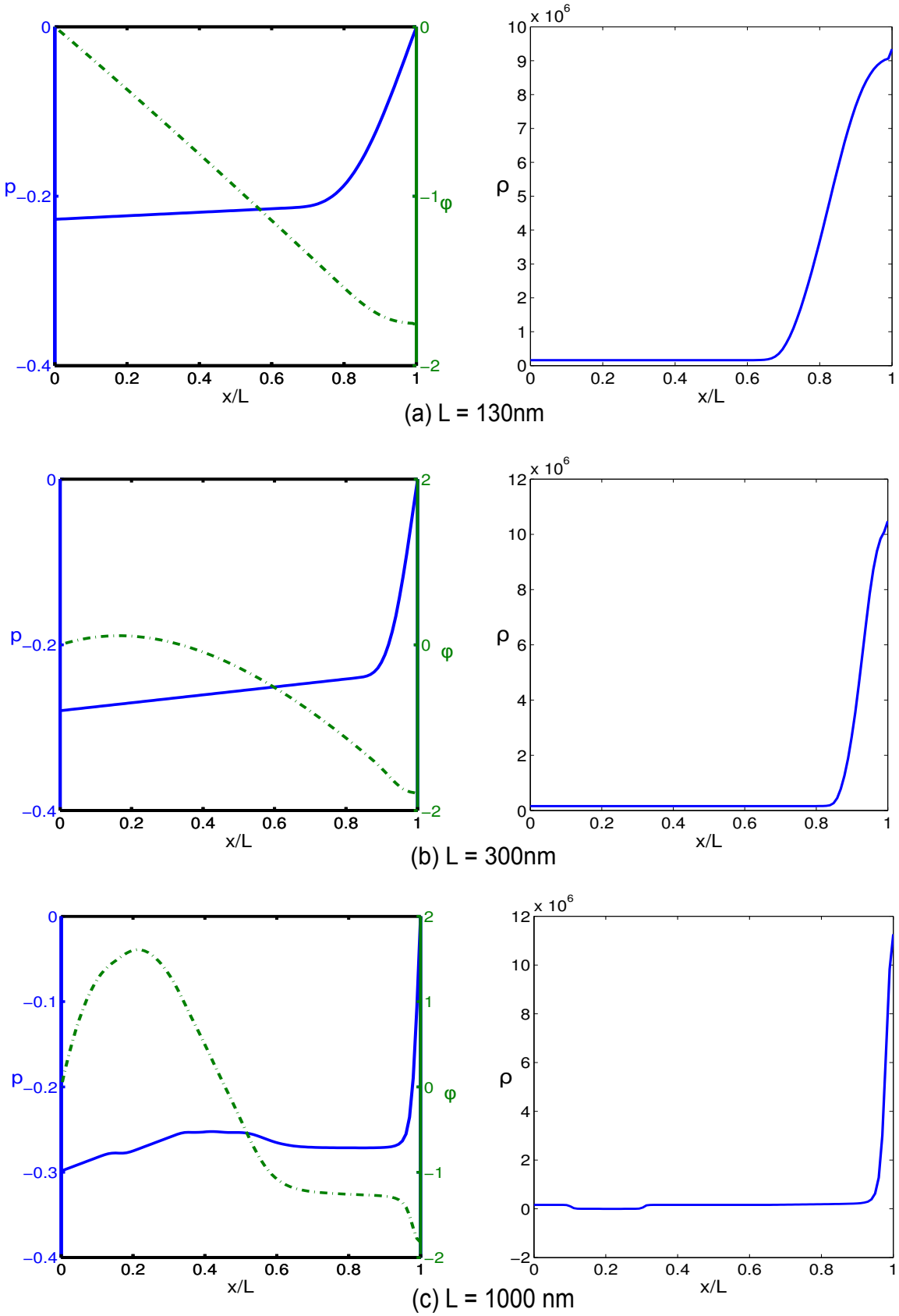

Figure 3.19: Results from the 1-D model at different L. $N_d = 10^{24}$, $N_a = 0$. Left columns shows $\mathbf{p}$ (blue) and ϕ (green). The right column shows ρ.

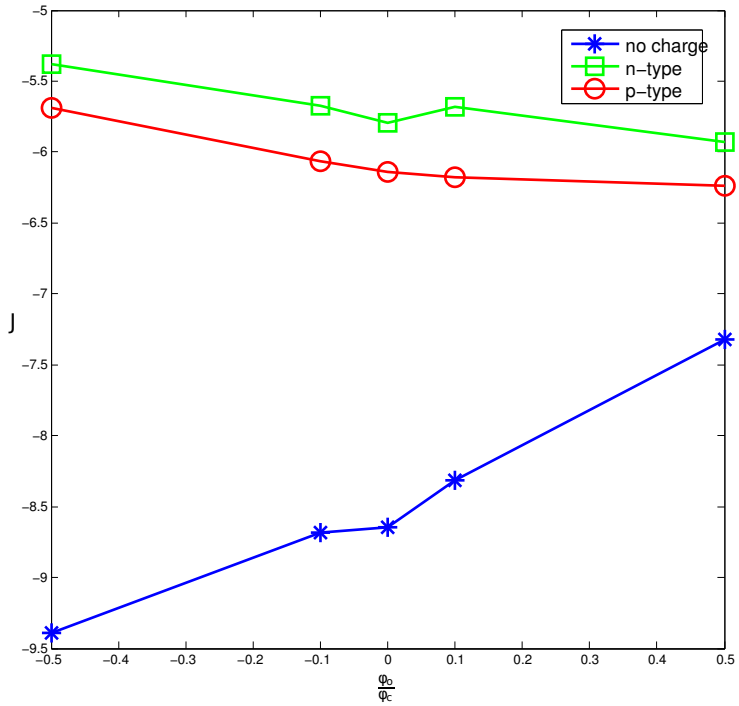

Figure 3.20: Variation of J with ϕ_o for different doping. $\sigma_o = 0$.

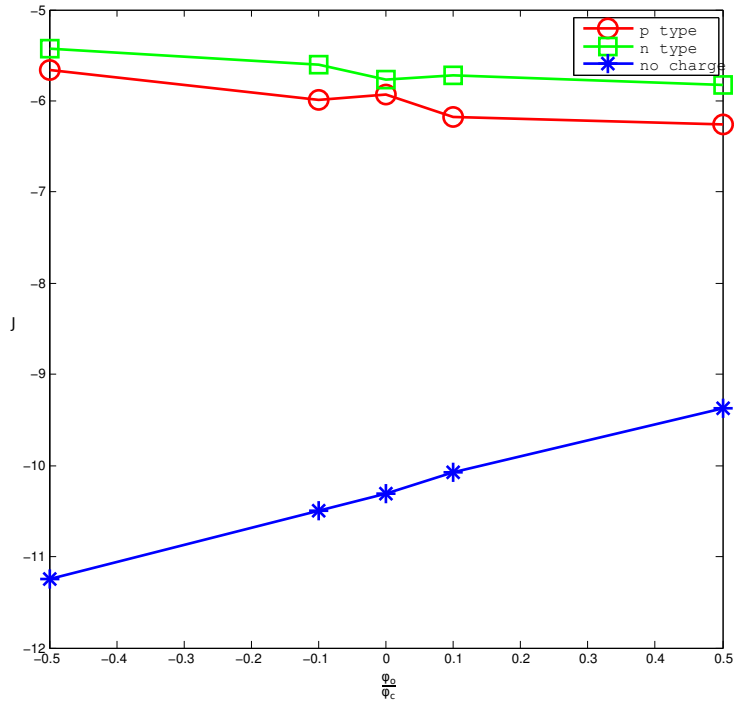

Figure 3.21: Variation of J with ϕ_o for different doping. $\sigma_o = 0.1$.

Appendix A

Appendices

A.1 Stress field of a shallow phase boundary

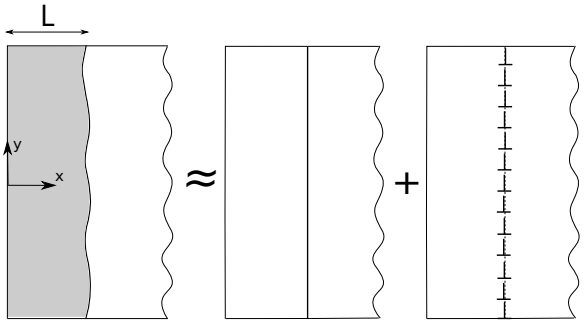

Figure A.1: Geometry of perturbed interface and the sub-problems for superposition.

Evaluating the stress field due to a deflected phase boundary close to a free edge is a non-trivial procedure and we outline the methodology here. Note that the elastic moduli are identical for the two phases. Since we are considering the 2-dimensional set up we use the classical Airy stress function method to evaluate the fields. First we derive the stress field due to a deflection of the form $f(y) = A\cos(\lambda y)$ and use the result to evaluate the stress field and driving force due to an arbitrary deflection. We assume that the perturbation is shallow i.e $A << \lambda$. Let the interface be positioned at $x = L$. We denote the initial stress created due to a straight interface by σ_o. The Airy stress function for the half space can be written as

$$\Phi^{(1)}(x,y) = \Phi^o(x,y) + \Phi_1(x,y) \quad 0 < x < L, \qquad \Phi^{(2)}(x,y) = \Phi_2(x,y) \quad x > L. \quad \text{(A.1.1)}$$

where Φ^o represents the Airy function of the straight interface and Φ_1, Φ_2 represent the perturbations due to the deflection. The effect of the deflection is equivalent to the presence of shear tractions $t_{sh} = -\sigma_o A\lambda \sin(\lambda y)$ and a dislocation distribution of density $B_x = (2+\nu)A\varepsilon_o\lambda \sin(\lambda y)$ at the interface. The fields created due to these distributions represent the perturbed fields. Following Sneddon [99], we start out with the following Φ_1, Φ_2, obtained as solutions to the biharmonic equation after taking the Fourier transform along y-direction:

$$\Phi_1(x,k) = (A_1 + B_1 x)e^{-|k|(x-L)} + (C_1 + D_1 x)e^{|k|(x-L)} \qquad 0 < x < L, \tag{A.1.2a}$$

$$\Phi_2(x,k) = (A_2 + B_2 x)e^{-|k|(x-L)} \qquad x > L. \tag{A.1.2b}$$

The boundary conditions that these functions need to satisfy are a) the traction free condition at $x = 0$, b) traction and displacement jumps at $x = L$. The first condition gives the following equations

$$-k^2\Phi_1(0,k) = 0, \tag{A.1.3a}$$

$$-ik\frac{\partial \Phi_1}{\partial x}(0,k) = 0. \tag{A.1.3b}$$

The traction conditions reduce to

$$-k^2(\Phi_1 - \Phi_2)(L,k) = 0, \tag{A.1.4a}$$

$$ik\Big(\frac{\partial \Phi_1}{\partial x} - \frac{\partial \Phi_2}{\partial x}\Big)(L,k) = -\sigma_o\lambda\mathcal{F}\{A\sin(\lambda y)\}, \tag{A.1.4b}$$

The displacement conditions yield

$$[[\frac{\partial^2 \Phi}{\partial x^2} + \nu k^2 \Phi]](L,k) = 0, \tag{A.1.5a}$$

$$[[\frac{1}{k^2}\frac{\partial^3 \Phi}{\partial x^3} - (2+\nu)\frac{\partial \Phi}{\partial x}]](L,k) = (2+\nu)\sigma_o\mathcal{F}\{A\cos(\lambda y)\}. \tag{A.1.5b}$$

In the above equations $\mathcal{F}$ represents the Fourier Transform with respect to y. We solve for the unknowns in (A.1.2) using the above equations. Then we obtain the Airy stress

functions in real space by applying the Inverse Fourier transform with respect to k giving us

$$\Phi_1(x,y) = \frac{\sigma_o A e^{-\lambda(x+L)}\{3+\lambda L+\lambda x(5+2\lambda L)+e^{2\lambda x}(-3+\lambda(x-L))\}\cos(\lambda y))}{4\lambda}, \tag{A.1.6a}$$

$$\Phi_2(x,y) = \frac{\sigma_o A e^{-\lambda(x+L)}\{3+\lambda L+\lambda x(5+2\lambda L)-e^{2\lambda L}(3+\lambda(x-L))\}\cos(\lambda y)}{4\lambda}. \tag{A.1.6b}$$

The expressions for stress components can be computed by using the standard formulae relating the stress components and Airy stress function. The results were checked by adopting them to the special cases of $L = 0$ and $L \to \infty$ (after an appropriate change of coordinates) and comparing them to those listed in literature [102]. Using the expression for driving force, (2.2.13), the driving force on a deflected interface of the form $f(y) = A\cos(\lambda y)$ turns out to be

$$d_{per} = -\frac{\sigma_o \varepsilon_o}{4} A\lambda e^{-2\lambda L}\left\{13 - 5e^{2\lambda L} + 2\lambda L(5+\lambda L)\right\}\cos(\lambda x). \tag{A.1.7}$$

Using (A.1.6), we can express the the stress field and driving force on an arbitrary symmetric deflection in terms of its Fourier Cosine components.

A.2 Solution to the integral equations

We normalize the intervals to solve the equations numerically:

$$s = \frac{t}{h_1} \quad z = \frac{x}{h_1} \qquad 0 < t, x < h_1, \tag{A.2.1a}$$

$$s = \frac{t}{h_2} \quad z = \frac{x}{h_2} \qquad 0 < t, x < h_2, \tag{A.2.1b}$$

$$C_1(h_1 s) = B_1(s) \qquad C_2(h_2 s) = B_2(s), \tag{A.2.1c}$$

and in order to make the the numerical procedure more amenable we extend the interval of integration from $[0,1]$ to $[-1,1]$ through the following even extension:

$$B_1(-s) = B_1(s), \quad B_2(-s) = B_2(s) \qquad -1 < s < 1. \tag{A.2.2}$$

So the equations needed to solve for $B_1(s)$ and $B_2(s)$ are

$$\frac{1}{2}\int_{-1}^{1}\frac{B_1(s)}{\sqrt{1-s^2}}\frac{\pi h_1}{2b}G_1(|h_1 s|,h_1 z)ds+\frac{1}{2}\int_{-1}^{1}\frac{B_2(s)}{\sqrt{1-s^2}}\frac{\pi h_2}{2b}G_2(|h_2 s|,h_1 z)ds=-\sigma_o \quad 0<z<1, \tag{A.2.3a}$$

$$\frac{1}{2}\int_{-1}^{1}\frac{B_1(s)}{\sqrt{1-s^2}}\frac{\pi h_1}{2b}G_2(|h_1 s|,h_2 z)ds+\frac{1}{2}\int_{-1}^{1}\frac{B_2(s)}{\sqrt{1-s^2}}\frac{\pi h_2}{2b}G_1(|h_2 s|,h_2 z)ds=-\sigma_o \quad 0<z<1. \tag{A.2.3b}$$

Due to the the weight function $\frac{1}{\sqrt{1-s^2}}$, we use the Gauss-Chebyshev integration scheme as described in Erdogan et.al. in [31]. Making use of the scheme and noting that G_1 and G_2 vanish at $s=0$

$$\sum_{i=1}^{n_1}\frac{\pi}{2n_1+1}B_1(s_i)\frac{\pi h_1}{2b}G_1(|h_1 s_i|,h_1 z_k)+\sum_{j=1}^{n_2}\frac{\pi}{2n_2+1}B_2(s_j)\frac{\pi h_1}{2b}G_2(|h_2 s_j|,h_1 z_k)=-\sigma_o$$
$$k=1,2,...,n_1, \tag{A.2.4a}$$

$$\sum_{i=1}^{n_1}\frac{\pi}{2n_1+1}B_1(s_i)\frac{\pi h_1}{2b}G_2(|h_1 s_i|,h_2 z_l)+\sum_{j=1}^{n_2}\frac{\pi}{2n_2+1}B_2(s_j)\frac{\pi h_2}{2b}G_1(|h_2 s_j|,h_2 z_l)=-\sigma_o$$
$$l=1,2,...,n_2, \tag{A.2.4b}$$

where

$$s_i=\cos\left(\frac{2i-1}{4n_1+2}\pi\right) \qquad z_k=\cos\left(\frac{k\pi}{2n_1+1}\right), \tag{A.2.5a}$$

$$s_j=\cos\left(\frac{2j-1}{4n_2+2}\pi\right) \qquad z_l=\cos\left(\frac{l\pi}{2n_2+1}\right). \tag{A.2.5b}$$

Introducing new variables

$$a_1=\frac{h_1}{b},\quad a_2=\frac{h_2}{b},\quad t_{1i}=\frac{\pi a_1}{2}s_i,\quad t_{2j}=\frac{\pi a_2}{2}s_j,\quad y_{1k}=\frac{\pi a_1}{2}z_k,\quad y_{2l}=\frac{\pi a_2}{2}z_l$$
$$A_1(s_i)=-\frac{\pi}{2n_1+1}\frac{B_1(s_i)}{\sigma_o}\quad i=1,2,....,n_1, \qquad A_2(s_j)=-\frac{\pi}{2n_2+1}\frac{B_2(s_j)}{\sigma_o}\quad j=1,2,....,n_2. \tag{A.2.6a}$$

The equations (A.2.4) reduce to the following set of linear algebraic equations which can be solved to get $A_1(s_i)$ and $A_2(s_j)$

$$\sum_{i=1}^{n_1} A_1(s_i)H_1(t_{1i}, y_{1k}; a_1) + \sum_{j=1}^{n_2} A_2(s_j)H_2(t_{2j}, y_{1k}; a_1) = 1 \qquad k = 1, 2, ...n_1,$$
$$\sum_{i=1}^{n_1} A_1(s_i)H_2(t_{1i}, y_{2l}; a_1) + \sum_{j=1}^{n_2} A_2(s_j)H_1(t_{2j}, y_{2l}; a_2) = 1 \qquad l = 1, 2, ...n_2, \quad \text{(A.2.7a)}$$

where

$$H_1(t, y; a) = \frac{\pi a}{2}(2\coth(y+t) - (y+3t)\text{cosech}^2(y+t) + 4ty\coth(y+t)\text{cosech}^2(y+t)$$
$$- 2\coth(y-t) + (y-t)\text{cosech}^2(y-t)), \quad \text{(A.2.8a)}$$
$$H_2(t, y; a) = \frac{\pi a}{2}(4t + 2\tanh(y+t) - (y+3t)\tanh^2(y+3t) - 4ty\tanh(y+t)(1-\tanh^2(y+t))$$
$$- 2\tanh(y-t) + (y-t)\tanh^2(y-t). \quad \text{(A.2.8b)}$$

The non-dimensionalized stress intensity factor is given by:

$$N_i = \frac{K_i}{\sigma_o\sqrt{2\pi b}} = -\pi\sqrt{\frac{a_i}{2}}\frac{C_i(h_i)}{\sigma_o} = (2n_i + 1)\sqrt{\frac{a_i}{2}}A_i(1). \quad \text{(A.2.9)}$$

This formulation is validated by comparing values of SIF obtained through this method for different geometries with those available in literature. First we look the case of a single edge crack. By choosing values $h_1 = h_2 = h$ and $h/b << 1$ we obtain the following values for N.

$\frac{h}{b}$	h	$\frac{K}{\sigma_o}$	$\frac{K}{\sigma_o} = 1.12\sqrt{\pi h}$ [14]
0.0025	0.025	0.3141	0.314
0.005	0.05	0.4442	0.444
0.01	0.1	0.6278	0.627
0.02	0.2	0.886	0.887

Table A.1: Table comparing the N value for a single edge crack.

Table A.1 shows that the values obtained from our formulation agree well with the closed

form solution.

Next we validate the procedure by comparing the N values of a periodic array of uniformly spaced edge cracks of equal size.

$\frac{h}{b}$	h	$\frac{K}{\sigma_o}$	$\frac{K}{\sigma_o}$ [14]
0.65	0.104	1.474	1.472
1.23	0.195	1.729	1.729
1.49	0.237	1.757	1.752
3.64	0.578	1.758	1.758
4.88	0.776	1.766	1.762

Table A.2: Table comparing N values for a uniform array of parallel edge cracks.

Table A.2 shows that once again the values compare very well. This validates our numerical scheme.

A.3 Integral identities

Consider an evolving domain $\Omega(t)$ containing a discontinuity like a phase boundary $\mathcal{S}$ and a crack Γ. To avoid the singularity of the fields at the crack tip we remove a cylindrical region C_δ around the crack tip. The integral of field quantities is interpreted in the following sense

$$\int_{\Omega(t)} \psi dx = \lim_{\delta \to 0} \int_{\Omega(t)\setminus C_\delta} \psi dx. \tag{A.3.1}$$

Using the classical transport identities, the transport theorem for a scalar quantity on an evolving domain can be written as [41]:

$$\begin{aligned} \frac{d}{dt}\int_{\Omega\setminus C_\delta} \psi dx &= \frac{d}{dt}\int_{\Omega_\alpha\setminus C_\delta} \psi dx + \frac{d}{dt}\int_{\Omega_\beta} \psi dx \\ &= \int_{\Omega\setminus C_\delta} \dot{\psi} dx + \int_{\partial\Omega(t)} \psi(\mathbf{u}.\hat{m}) ds - \int_{\partial C_\delta} \psi(\mathbf{a}.\hat{n}) ds \\ &\quad - \int_{\mathcal{S}} [[\psi]] v_n ds. \end{aligned} \tag{A.3.2}$$

Assuming the smoothness of the fields the integration and limit $\delta \to 0$ can be switched which leads to

$$\frac{d}{dt}\int_{\Omega(t)} \psi dx = \int_{\Omega\setminus C_\delta} \dot{\psi} dx + \int_{\partial\Omega(t)} \psi(\mathbf{u}.\hat{m}) ds - \lim_{\delta\to 0}\int_{\partial C_\delta} \psi(\mathbf{a}.\hat{n}) ds - \int_{\mathcal{S}} [[\psi]] v_n ds, \tag{A.3.3}$$

which represents the transport theorem for a domain containing a moving phase boundary and a growing crack. Similarly the we can derive the divergence theorem on a domain containing a crack and a discontinuity like a phase boundary. Assuming a smooth tensor field $\mathbf{A}$

$$\int_\Omega \nabla.\mathbf{A} dx = \lim_{\delta\to 0}\int_{\Omega\setminus C_\delta} \nabla.\mathbf{A} dx. \tag{A.3.4}$$

Using the classical divergence theorem

$$\begin{aligned}\int_{\Omega\setminus C_\delta} \nabla.\mathbf{A} dx &= \int_{\Omega_\alpha\setminus C_\delta} \nabla.\mathbf{A} dx + \int_{\Omega_\beta} \nabla.\mathbf{A} dx \\ &= \int_{\partial\Omega} \mathbf{A}.\hat{m} ds - \int_{\partial C_\delta} \mathbf{A}.\hat{n} ds - \int_{\mathcal{S}} [[\mathbf{A}]].\hat{k} ds - \int_\Gamma [[A]].\hat{c} ds.\end{aligned} \tag{A.3.5}$$

So divergence theorem for a smooth tensor field over Ω is

$$\int_\Omega \nabla.\mathbf{A} = \int_{\partial\Omega} \mathbf{A}.\hat{m} ds - \lim_{\delta\to 0}\int_{\partial C_\delta} \mathbf{A}.\hat{n} ds - \int_{\mathcal{S}} [[\mathbf{A}]].\hat{k} ds - \int_\Gamma [[A]].\hat{c} ds. \tag{A.3.6}$$

A.4 Optimal orientation of phase boundary

We present here briefly the analysis to determine the optimal orientation of the normal $\hat{n}$ in the simple case where the transformation strain is diagonal. Once $\hat{n}$ is established using (2.3.3) and (2.3.4) one can determine the morphology of the defects which could arise due to the transformation. Following Kohn[57], in the case of an isotropic elastic material with material constants κ (bulk modulus) and μ (shear modulus), and with $\mathbb{C}$ assuming the form $\mathbb{C} = \kappa\delta_{ij}\delta_{kl} + \mu(\delta_{ik}\delta_{jl} + \delta_{il}\delta_{jk} - \frac{2}{3}\delta_{ij}\delta_{kl})$, the optimization problem (2.3.1) can be rewritten

as

$$\gamma/\mu = \max_{|m|=1} \left\{ 4(|\varepsilon^* m|^2 - \langle \varepsilon^* m, m\rangle^2) + \frac{1}{2+\alpha}(\alpha\ tr\varepsilon^* + 2\langle \varepsilon^* m, m\rangle)^2 \right\}, \tag{A.4.1}$$

where $\alpha = \frac{\kappa n - 2\mu}{n\mu}$, and n is the dimension of the space. Analysis through the use of method of Lagrange multipliers leads to two possibilities : (a) m is one of the eigenvectors of ε^*, (b) m is a combination of two eigenvectors of ε^*. In case (a) the RHS of (A.4.1) reduces to

$$\gamma/\mu = \max_{\varepsilon_i} \frac{1}{2+\alpha}(\alpha tr\varepsilon^* + 2\varepsilon_i)^2. \tag{A.4.2}$$

In case (b), if we assume that the normal is given by the combination of eigenvectors corresponding to eigenvalues ε_i and ε_j the analysis leads to a necessary condition on the eigenvalues

$$\varepsilon_i < \frac{2+\alpha}{2(1+\alpha)} \left(\varepsilon_i + \varepsilon_j + \frac{\alpha}{2+\alpha} tr\varepsilon^* \right) < \varepsilon_j. \tag{A.4.3}$$

So there exist different scenarios depending on the eigenvalues of ε^* and the case which maximizes (A.4.1) is the optimal normal. Consider the case of a diagonal transformation strain, $\varepsilon^* = diag(\varepsilon_1 \quad \varepsilon_2 \quad \varepsilon_3)$, with $\varepsilon_1 > \varepsilon_2 > \varepsilon_3 > 0$. In three dimensions ($n = 3$), $\alpha = (\frac{\kappa}{\mu} - \frac{2}{3}) = \frac{2\nu}{1-2\nu}$, where ν is the Poisson's ratio. Let us start with case (b) and assume that the normal is a combination of two eigenvectors corresponding to eigenvalues, say ε_1 and ε_2. The expression in the middle of condition (A.4.3) reduces to $\varepsilon_1 + \varepsilon_2 + \nu\varepsilon_3$. It can be immediately understood that the condition (A.4.3) cannot be satisfied by ε_1 and ε_2 or any two of the three positive eigenvalues of the transformation strain. So in this case the only possible regime is case (a) where the optimal normal is given by the eigenvector which maximizes the RHS of (A.4.2). Right away one can conclude that in this case the eigenvalue with the greatest magnitude maximizes (A.4.2). So in this case the optimal normal of the phase boundary is given by the eigenvector corresponding to the eigenvalue of largest magnitude. A similar conclusion applies to the case $\varepsilon_1 < \varepsilon_2 < \varepsilon_3 < 0$.

A.5 Driving force on a phase boundary

Consider a phase boundary separating two phases α and β with elastic energy density given by (2.2.2). The two phases are assumed to have identical elastic moduli. The expression for driving force acting on the phase boundary (2.2.12) can be simplified using the following identity.

$$A : B = (A.\hat{k}).(B.\hat{k}) \quad \text{when} \quad B.\hat{l} = 0 \quad \hat{k}.\hat{l} = 0. \tag{A.5.1}$$

The traction continuity and displacement compatibility at the phase boundary dictate that

$$[[\sigma]].\hat{k} = 0, \qquad [[\nabla u]].\hat{l} = 0, \tag{A.5.2}$$

where $\hat{k}$ is the normal and $\hat{t}$ is the tangent vector to the phase boundary. Using this identity

$$\hat{k}.[[\psi - \nabla u^T.\sigma]].\hat{k} = [[\psi]] - [[\sigma.\nabla u]] = [[\psi]] - \langle\sigma\rangle[[\varepsilon]], \tag{A.5.3}$$

where the traction continuity and the symmetry of the stress tensor are used to establish the second equality. Substituting (2.2.2) into (A.5.3) yeilds

$$\begin{aligned} d_S &= \frac{1}{2}\sigma^\alpha\varepsilon^* - \frac{1}{2}\sigma^\alpha\varepsilon^\beta + \frac{1}{2}\sigma^\beta\varepsilon^\alpha - \omega = \frac{1}{2}\varepsilon^*.\mathbb{C}.(\varepsilon^\alpha - \varepsilon^*) + \frac{1}{2}\varepsilon^*.\mathbb{C}.\varepsilon^\beta - \omega \\ &= \frac{(\sigma^\alpha + \sigma^\beta)}{2}.\varepsilon^* - \omega = \langle\sigma\rangle : \varepsilon^* - \omega. \end{aligned} \tag{A.5.4}$$

A.6 Divergence free property of augmented energy momentum tensor

The augmented energy momentum tensor, $\mathbf{\Psi}$, is a divergence-free quantity at equilibrium. We prove this using the equations governing the equilibrium state of the ferroelectric written

in terms of the electric enthalpy, H,

$$\nabla.\Big(\frac{\partial H}{\partial \nabla \mathbf{p}}\Big) - \frac{\partial H}{\partial \mathbf{p}} - \nabla\phi = 0, \tag{A.6.1}$$

$$\nabla.\Big(\frac{\partial H}{\partial \varepsilon}\Big) = 0, \tag{A.6.2}$$

$$\nabla.\Big(\frac{\partial H}{\partial \nabla \phi}\Big) - \frac{\partial H}{\partial \phi} = 0. \tag{A.6.3}$$

Note that the above three equations represent the Euler-Lagrange equations of the corresponding energy minimum principle. The first equations represents the equilibrium of polarization, second is the mechanical equilibrium equation in linearized kinematics and the third is the Maxwell's equation. The divergence of the augmented energy momentum tensor $\mathbf{\Psi}$ is

$$\begin{aligned}\nabla.\mathbf{\Psi} &= \nabla.\Big(H\mathbf{I} - (\nabla\mathbf{p})^T\frac{\partial H}{\partial \nabla \mathbf{p}} - (\nabla\mathbf{u})^T\frac{\partial H}{\partial \varepsilon} + \mathbf{E}\otimes\mathbf{D}\Big)\\ &= \nabla H - \nabla.\Big(\frac{\partial H}{\partial \nabla \mathbf{p}}\Big).\nabla\mathbf{p} - \frac{\partial H}{\partial \nabla \mathbf{p}}\nabla\nabla\mathbf{p} - \nabla.\Big(\frac{\partial H}{\partial \varepsilon}\Big).\nabla\mathbf{u} - \frac{\partial H}{\partial \nabla \varepsilon}\nabla\nabla\mathbf{u}\\ &\quad - (\nabla.\mathbf{D})\nabla\phi - (\nabla\nabla\phi)\mathbf{D}.\end{aligned} \tag{A.6.4}$$

Since the electric enthalpy H is defined as

$$H = H(\mathbf{p}, \nabla\mathbf{p}, \phi, \nabla\phi, \mathbf{u}) = W(\mathbf{p}, \nabla\mathbf{p}, \rho, \mathbf{u}) - \frac{\epsilon_o}{2}|\nabla\phi|^2 + \mathbf{p}.\nabla\phi + \rho\phi, \tag{A.6.5}$$

its derivatives can be written as follows

$$\begin{aligned}&\frac{\partial H}{\partial \varepsilon} = \frac{\partial W}{\partial \varepsilon} = \sigma, \qquad \frac{\partial H}{\partial \mathbf{p}} = \frac{\partial W}{\partial \mathbf{p}} + \nabla\phi, \qquad \frac{\partial H}{\partial \nabla \mathbf{p}} = \frac{\partial W}{\partial \nabla \mathbf{p}}, \qquad \frac{\partial H}{\partial \phi} = \rho,\\ &\frac{\partial H}{\partial \nabla \phi} = -\epsilon_o\nabla\phi + \mathbf{p} = \mathbf{D}.\end{aligned} \tag{A.6.6}$$

Now the gradient of H can be expanded as

$$\nabla H = \frac{\partial H}{\partial \mathbf{p}}(\nabla\mathbf{p})^T + \frac{\partial H}{\partial \nabla \mathbf{p}}.\nabla\nabla\mathbf{p} + \frac{\partial H}{\partial \phi}\nabla\phi + \frac{\partial H}{\partial \nabla \phi}\nabla\nabla\phi. \tag{A.6.7}$$

Substituting (A.6.6) into the expansion for ∇H (A.6.7) and further substituting this in

(A.6.4) and using the governing equations, (A.6.1), yeilds the result $\nabla.\mathbf{\Psi} = 0$.

A.7 Domain integral for evaluating driving force, J

The driving force on a crack in a ferroelectric is given by

$$J = \int_{C_1} \hat{t}.\mathbf{\Psi}.\hat{n}ds, \qquad \mathbf{\Psi} = H\mathbf{I} - (\nabla\mathbf{p})^T \frac{\partial H}{\partial \nabla\mathbf{p}} - (\nabla\mathbf{u})^T \frac{\partial H}{\partial \varepsilon} + \mathbf{E}\otimes\mathbf{D}. \tag{A.7.1}$$

where C_1 is a contour enclosing the crack tip with a normal $\hat{n}$. For a crack growing along the x-axis $\hat{t} = \hat{e}_1$. Consider a weight function, q, which assumes the value 1 over an open domain containing the contour C_1 and assumes a value zero over a contour C_2 enclosing the domain, see Figure A.2. Multiplying the integrand in (A.7.1) with q, the driving force on a crack growing along the x-axis can be written as

$$J_1 = \int_C \hat{e}_1.\mathbf{\Psi}q.\hat{n}ds + \int_{\Gamma_+} \hat{e}_1\mathbf{\Psi}q.\hat{e}_2 ds - \int_{\Gamma_-} \hat{e}_1\mathbf{\Psi}q.\hat{e}_2 ds, \tag{A.7.2}$$

where $C = C_1 + C_2 + \Gamma_+ + \Gamma_-$, is the contour enclosing a domain A, and $\hat{e}_2$ is the normal to the crack surfaces for a crack along the x-axis. Using the divergence theorem the driving force can be recast as a domain integral

$$J_1 = \int_A \hat{e}_1.\nabla.(\mathbf{\Psi}q)da + \int_{\Gamma_+} \hat{e}_1\mathbf{\Psi}q.\hat{e}_2 ds - \int_{\Gamma_-} \hat{e}_1\mathbf{\Psi}q.\hat{e}_2 ds. \tag{A.7.3}$$

The boundary conditions along the crack surface are as follows

$$\frac{\partial H}{\partial \nabla\mathbf{p}}.\hat{e}_2 = 0, \qquad \frac{\partial H}{\partial \nabla\varepsilon}.\hat{e}_2 = 0, \qquad \mathbf{D}.\hat{e}_2 = 0, \tag{A.7.4}$$

which reduces the integral along the crack surfaces to zero. So we are left with

$$J_1 = \int_A \hat{e}_1.\nabla.(\mathbf{\Psi}q)da = \int_A \hat{e}_1\mathbf{\Psi}.\nabla q da. \tag{A.7.5}$$

The second equality above results form the fact that $\mathbf{\Psi}$ is divergence free.

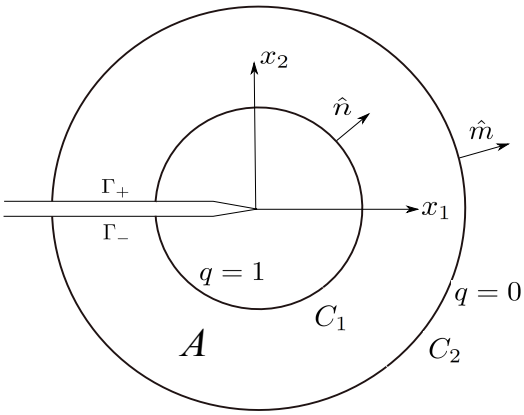

Figure A.2: Notation for domain integral formulation to evaluate the driving force on a crack

Bibliography

[1] *ABAQUS/CAE User's manual : version 6.9.* Dassault Systèmes Simulia Corp., Providence, RI, USA., 2009.

[2] A. Abdollahi and I. Arias. Phase-field modeling of the coupled microstructure and fracture evolution in ferroelectric single crystals. *Acta Materialia*, 59:4733–4746, 2011.

[3] A. Abdollahi and I. Arias. Phase-field modeling of crack propagation in piezoelectric and ferroelectric materials with different electromechanical crack conditions. *Journal of the Mechanics and Physics of Solids*, 60:2100–2126, 2012.

[4] R. Abeyaratne and J.K. Knowles. On the driving traction acting on a surface of strain discontinuity in a continuum. *Journal of the Mechanics and Physics of Solids*, 38:345–360, 1990.

[5] C. Allain and L. Limat. Regular patterns of cracks formed by directional drying of a collodial suspension. *Physical Review Letters*, 74:2981–2984, 1995.

[6] N.W. Ashcroft and N.D. Mermin. *Solid state physics.* Science: Physics. Saunders College, 1976.

[7] H.A. Bahr, U. Bahr, and A. Petzold. 1-d deterministic crack pattern formation as a growth process with restrictions. *EPL (Europhysics Letters)*, 19:485,1992.

[8] H.A. Bahr, G. Fischer, and H.J. Weiss. Thermal-shock crack patterns explained by single and multiple crack propagation. *Journal of Materials Science*, 21:2716–2720, 1986.

[9] H.A. Bahr, H.J. Weiss, H.G. Maschke, and F. Meissner. Multiple crack propagation in a strip caused by thermal shock. *Theoretical and Applied Fracture Mechanics*, 10:219–226, 1988.

[10] H.A. Bahr, H.J. Weiss, U. Bahr, M. Hofmann, G. Fischer, S. Lampenscherf, and H. Balke. Scaling behavior of thermal shock crack patterns and tunneling cracks driven by cooling or drying. *Journal of the Mechanics and Physics of Solids*, 58:1411–1421, 2010.

[11] Z.P. Bazant and H. Ohtsubo. Stability conditions for propagation of a system of cracks in a brittle solid. *Mechanics Research Communications*, 4:353–366, 1977.

[12] Z.P. Bazant, H. Ohtsubo, and K. Aoh. Stability and post-critical growth of a system of cooling or shrinkage cracks. *International Journal of Fracture*, 15:443–456, 1979.

[13] Z.P. Bazant and A.B. Wahab. Instability and spacing of cooling or shrinkage cracks. *Journal of the Engineering Mechanics Division, ASCE*, 105:873–889, 1979.

[14] J.P. Benthem and W.T. Koiter. Aymptotic approximations to crack problems. In G.C. Sih, editor, *Methods of analysis and solutions of crack problems: Recent developments in fracture mechanics*, Mechanics of Fracture. Noordhoff International Pub., 1973.

[15] K. Bhattacharya and G. Ravichandran. Ferroelectric perovskites for electromechanical actuation. *Acta Materialia*, 51:5941–5960, 2003.

[16] E.N. Burcsu. *Investigation of large strain actuation in barium titanate*. PhD thesis, California Institute of Technology, 2001.

[17] G.T. Camacho and M. Ortiz. Computational modelling of impact damage in brittle materials. *International Journal of Solids and Structures*, 33:2899–2938, 1996.

[18] W. Cao and L. E. Cross. Theory of tetragonal twin structures in ferroelectric perovskites with a first-order phase transition. *Physical Review B*, 44:5, 1991.

[19] A. Chambolle, G.A Francfort, and J.J. Marigo. When and how do cracks propagate ? *Journal of the Mechanics and Physics of Solids*, 57:1614–1622, 2009.

[20] L.Q. Chen. Phase-field method of phase transitions/domain structures in ferroelectric thin films: A review. *Journal of the American Ceramic Society*, 91:1835–1844, 2008.

[21] I. Chenchiah and K. Bhattacharya. The relaxation of two-well energies with possibly unequal moduli. *Archive for Rational Mechanics and Analysis*, 187:409–479, 2008.

[22] B.D. Coleman and W. Noll. The thermodynamics of elastic materials with heat conduction and viscosity. *Archive for Rational Mechanics and Analysis*, 13:167–178, 1963.

[23] D. Fang, S. Ai, and J. Liu. Electromechanical deformation and fracture of piezoelectric/ferroelectric materials. *Acta Mechanica Sinica*, 17(3):193–213, 2001.

[24] D. Damjanovic. Ferroelectric, dielectric and piezoelectric properties of ferroelectric thin films and ceramics. *Reports on Progress in Physics*, 61:1267, 1998.

[25] W.F.J. Deeg. *The analysis of dislocation, crack, and inclusion problems in piezoelectric solids*. PhD thesis, Stanford Univ., CA., 1980.

[26] P.W. Dondl and K. Bhattacharya. Effective behavior of an interface propagating through a periodic elastic medium. *In preparation*, 2012.

[27] S.L. dos Santos e Lucato, D.C. Lupascu, and J. Rödel. Effect of poling direction on r-curve behavior in lead zirconate titanate. *Journal of the American Ceramic Society*, 83:424–426, 2000.

[28] P.M. Duff. *Holmes' Principles of Physical Geology*. Nelson Thornes Limited, 1993.

[29] M.L. Dunn. The effects of crack face boundary conditions on the fracture mechanics of piezoelectric solids. *Engineering Fracture Mechanics*, 48:25–39, 1994.

[30] A. R. Engert, F. Felten, H. Jelitto, and G. A. Schneider. What do we know about surface charges on cracks in ferroelectric ceramics?, *IUTAM Symposium on Multiscale Modelling of Fatigue, Damage and Fracture in Smart Materials*, 24:9–20, 2011.

[31] F. Erdogan, G.D. Gupta, and T.S. Cook. Numerical solution of singular integral equations. In G.C. Sih, editor, *Methods of analysis and solutions of crack problems: Recent*

developments in fracture mechanics, Mechanics of fracture. Noordhoff International Pub., 1973.

[32] J.D. Eshelby. The continuum theory of lattice defects. In *Solid State Physics*, volume 3, pages 79 – 144. Academic Press, 1956.

[33] D. Fang, Y. Jiang, S. Li, and C.T. Sun. Interactions between domain switching and crack propagation in poled $BaTiO_3$ single crystal under mechanical loading. *Acta Materialia*, 55:5758–5767, 2007.

[34] F. Fang, W. Yang, F.C. Zhang, and H.S. Luo. Fatigue crack growth for batio3 ferroelectric single crystals under cyclic electric loading. *Journal of the American Ceramic Society*, 88:2491–2497, 2005.

[35] L.B. Freund. The mechanics of dislocations in strained-layer semiconductor materials. In *Advances in Applied Mechanics*, 30:1–66. Elsevier, 1993.

[36] L.B. Freund and S. Suresh. *Thin Film Materials*. Cambridge University Press, 2003.

[37] R. Fu and T.Y. Zhang. Effects of an electric field on the fracture toughness of poled lead zirconate titanate ceramics. *Journal of the American Ceramic Society*, 83:1215–1218, 2000.

[38] H. Gabrisch, J. Wilcox, and M.M. Doeff. TEM study of fracturing in spherical and plate-like $LiFePO_4$ particles. *Electrochemical and Solid-State Letters*, 11:A25–A29, 2008.

[39] R. Gerson and H. Jaffe. Electrical conductivity in lead titanate zirconate ceramics. *Journal of Physics and Chemistry of Solids*, 24:979–984, 1963.

[40] J.F. Geyer and S. Nemat-Nasser. Experimental investigation of thermally induced interacting cracks in brittle solids. *International Journal of Solids and Structures*, 18:349–356, 1982.

[41] M.E. Gurtin. *Configurational Forces As Basic Concepts of Continuum Physics*. Springer, 2000.

[42] M.E. Gurtin and P. Podio-Guidugli. Configurational forces and the basic laws for crack propagation. *Journal of the Mechanics and Physics of Solids*, 44:905–927, 1996.

[43] A. Haug and R. McMeeking. Cracks with surface charge in poled ferroelectrics. *European Journal of Mechanics - A/Solids*, 25:24–41, 2006.

[44] Y. Hayakawa. Pattern selection of multicrack propagation in quenched crystals. *Physical Review E*, 50:1748–1751, 1994.

[45] T.J.R. Hughes. *The Finite Element Method: Linear Static and Dynamic Finite Element Analysis*. Dover Publications, Incorporated, 2012.

[46] D. Hull and B.D. Caddock. Simulation of prismatic cracking of cooling basalt lava flows by the drying of sol-gels. *Journal of Materials Science*, 34:5707–5720, 1999.

[47] J.W Hutchinson and Z. Suo. Mixed mode cracking in layered materials. *Advances in applied mechanics*, 29:191, 1992.

[48] B. Jaffe, W.R. Cook, and H.L. Jaffe. *Piezoelectric ceramics*. Non-metallic solids. Academic Press, 1971.

[49] E.A. Jagla. Stable propagation of an ordered array of cracks during directional drying. *Physical Review E*, 65:046147, 2002.

[50] Y. Jiang, Y. Zhang, B. Liu, and D. Fang. Study on crack propagation in ferroelectric single crystal under electric loading. *Acta Materialia*, 57:1630–1638, Mar 2009.

[51] Y. Jiang, D. Fang, and F. Li. In situ observation of electric-field-induced domain switching near a crack tip in poled PMNT single crystal. *Applied Physics Letters*, 90:222907–222907–3, 2007.

[52] Z.H. Jin and C.T. Sun. On J-integral and potential energy variation. *International Journal of Fracture*, 126:L19–L24, 2004.

[53] W.C. Johnson and J.I.D. Alexander. Interfacial conditions for thermomechanical equilibrium in two phase crystals. *Journal of Applied Physics*, 59:2735–2746, 1986.

[54] F. Jona and G. Shirane. *Ferroelectric crystals*. International series of monographs on solid state physics. Pergamon Press, 1962.

[55] L.M. Keer, S. Nemat-Nasser, and A. Oranratnachai. Unstable growth of thermally induced interacting cracks in brittle solids: Further results. *International Journal of Solids and Structures*, 15:111–126, 1979.

[56] B. Kilic and E. Madenci. Prediction of crack paths in a quenched glass plate by using peridynamic theory. *International journal of fracture*, 156:165–177, 2009.

[57] R.V. Kohn. The relaxation of a double-well energy. *Continuum Mechanics and Thermodynamics*, 3:193–236, 1991.

[58] M. Kuna. Fracture mechanics of piezoelectric materials – where are we right now? *Engineering Fracture Mechanics*, 77:309–326, 2010.

[59] C.M. Landis. Fully coupled, multi-axial, symmetric constitutive laws for polycrystalline ferroelectric ceramics. *Journal of the Mechanics and Physics of Solids*, 50:127–152, 2002.

[60] C.M. Landis. Energetically consistent boundary conditions for electromechanical fracture. *International Journal of Solids and Structures*, 41:6291–6315, 2004.

[61] F.C. Larche and J.W. Cahn. Thermochemical equilibrium of multiphase solids under stress. *Acta Metallurgica*, 26:1579–1589, 1978.

[62] A. León Baldelli, B. Bourdin, J.J. Marigo, and C. Maurini. Fracture and debonding of a thin film on a stiff substrate: analytical and numerical solutions of a one-dimensional variational model. *Continuum Mechanics and Thermodynamics*, 25:243-268, 2013

[63] W. Li and C.M. Landis. Nucleation and growth of domains near crack tips in single crystal ferroelectrics. *Engineering Fracture Mechanics*, 78:1505–1513, 2011.

[64] A. Lisotti, V. De Renzi, C.A. Rozzi, E. Villa, F. Albertini, and G. Goldoni. Educational pathways through nanoscience: nitinol as a paradigmatic smart material. *Physics Education*, 48:298, 2013.

[65] M.W. Louie. *Electrocatalysis in solid acid fuel cells*. PhD thesis, California Institute of Technology, 2011.

[66] T. Maxisch and G. Ceder. Elastic properties of olivine Li_xFePO_4 from first principles. *Physical Review B*, 73:174112, 2006.

[67] R.M. McMeeking. Towards a fracture mechanics for brittle piezoelectric and dielectric materials. *International Journal of Fracture*, 108:25–41, 2001.

[68] R.M. McMeeking. The energy release rate for a griffith crack in a piezoelectric material. *Engineering Fracture Mechanics*, 71:1149–1163, 2004.

[69] K. Mehta and A.V. Virkar. Fracture mechanisms in ferroelectric-ferroelastic lead zirconate titanate (Zr:Ti=0.54:0.46) ceramics. *Journal of the American Ceramic Society*, 73:567–574, 1990.

[70] F. Meschke, A. Kolleck, and G.A. Schneider. R-curve behaviour of $BaTiO_3$ due to stress-induced ferroelastic domain switching. *Journal of the European Ceramic Society*, 17:1143–1149, 1997.

[71] A.N. Morozovska and E.A. Eliseev. Modelling of dielectric hysteresis loops in ferroelectric semiconductors with charged defects. *Journal of Physics: Condensed Matter*, 16:8937, 2004.

[72] A.N. Morozovska and E.A. Eliseev. Phenomenological description of polarization switching in ferroelectric semiconductors with charged defects. *physica status solidi (b)*, 242:947–961, 2005.

[73] S. Nemat-Nasser, L.M. Keer, and K.S. Parihar. Unstable growth of thermally induced interacting cracks in brittle solids. *International Journal of Solids and Structures*, 14:409 – 430, 1978.

[74] Q.S. Nguyen. *Stability and Nonlinear Solid Mechanics*. John Wiley, 2000.

[75] Y.E. Pak. Linear electro-elastic fracture mechanics of piezoelectric materials. *International Journal of Fracture*, 54:79–100, 1992.

[76] Y.E. Pak. Crack extension force in a piezoelectric material. *Journal of Applied Mechanics*, 57:647–653, 1990.

[77] Y.E. Pak and G. Herrmann. Conservation laws and the material momentum tensor for the elastic dielectric. *International Journal of Engineering Science*, 24:1365–1374, 1986.

[78] S.B. Park and C.T. Sun. Effect of electric field on fracture of piezoelectric ceramics. *International Journal of Fracture*, 70:203–216, 1993.

[79] S. Park and C.T. Sun. Fracture criteria for piezoelectric ceramics. *Journal of the American Ceramic Society*, 78:1475–1480, 1995.

[80] V.Z. Parton and B.A. Kudryavtsev. *Electromagnetoelasticity: Piezoelectrics and Electrically Conductive Solids*. Gordon and Breach Science Publishers, 1988.

[81] L. Pauchard, M. Adda-Bedia, C. Allain, and Y. Couder. Morphologies resulting from the directional propagation of fractures. *Physical Review E*, 67:027103, 2003.

[82] L. Pauchard, M. Adda-Bedia, C. Allain, and Y. Couder. Morphologies resulting from the directional propagation of fractures. *Physical Review E*, 67:027103, 2003.

[83] G.G. Pisarenko, V.M. Chushko, and S.P. Kovalev. Anisotropy of fracture toughness of piezoelectric ceramics. *Journal of the American Ceramic Society*, 68:259–265, 1985.

[84] K.J. Puttlitz and K.A. Stalter. *Handbook of Lead-Free Solder Technology for Microelectronic Assemblies*. Mechanical Engineering. Marcel Dekker, 2004.

[85] M.V. Raymond and D.M. Smyth. Defects and charge transport in perovskite ferroelectrics. *Journal of Physics and Chemistry of Solids*, 57:1507–1511, 1996.

[86] J.R. Rice. Mathematical analysis in the mechanics of fracture. In H. Liebowitz, editor, *Fracture: An Advanced Treatise. Mathematical fundamentals*, 2:191–311. Academic Press, 1968.

[87] J.R. Rice. A path independent integral and the approximate analysis of strain concentration by notches and cracks. *Journal of Applied Mechanics*, 35:379–386, 1968.

[88] O. Ronsin and B. Perrin. Multi-fracture propagation in a directional crack growth experiment. *Europhysics Letters*, 38:435, 1997.

[89] G.A. Schneider, F. Felten, and R.M. McMeeking. The electrical potential difference across cracks in pzt measured by kelvin probe microscopy and the implications for fracture. *Acta Materialia*, 51:2235–2241, 2003.

[90] G.A. Schneider and V. Heyer. Influence of the electric field on vickers indentation crack growth in batio3. *Journal of the European Ceramic Society*, 19(6–7):1299–1306, Jun 1999.

[91] G.A. Schneider. Influence of electric field and mechanical stresses on the fracture of ferroelectrics. *Annual Review of Materials Research*, 37:491–538, 2007.

[92] J.F. Scott and C.A. Paz de Araujo. Ferroelectric memories. *Science*, 246:1400–1405, 1989.

[93] J.F. Scott. *Ferroelectric Memories*. Advanced Microelectronics, 3. Springer, 2000.

[94] V.B. Shenoy, Y. Xiao, and K. Bhattacharya. Effect of doping on polarization profiles and switching in semiconducting ferroelectric thin films. *Journal of Applied Physics*, 111:084105–084105–14, 2012.

[95] C.F. Shih, B. Moran, and T. Nakamura. Energy release rate along a three-dimensional crack front in a thermally stressed body. *International Journal of Fracture*, 30:79–102, 1986.

[96] D. Shilo, G. Ravichandran, and K. Bhattacharya. Investigation of twin-wall structure at the nanometre scale using atomic force microscopy. *Nature Materials*, 3:453–457, 2004.

[97] K.A. Shorlin, J.R. de Bruyn, M. Graham, and S.W. Morris. Development and geometry of isotropic and directional shrinkage-crack patterns. *Physical Review E*, 61:6950–6957, 2000.

[98] Y.C. Shu and K.Bhattacharya. Domain patterns and macroscopic behaviour of ferroelectric materials. *Philosophical Magazine B*, 81:2021–2054, 2001.

[99] I.N. Sneddon. *Fourier transforms*. International series in pure and applied mathematics. McGraw-Hill, 1951.

[100] Y.C. Song, A.K. Soh, and Y. Ni. Phase field simulation of crack tip domain switching in ferroelectrics. *Journal of Physics D: Applied Physics*, 40:1175–1182, 2007.

[101] H. Sosa. Plane problems in piezoelectric media with defects. *International Journal of Solids and Structures*, 28:491–505, 1991.

[102] D.J. Srolovitz. On the stability of surfaces of stressed solids. *Acta Metallurgica*, 37:621–625, 1989.

[103] Y. Su and C.M. Landis. Continuum thermodynamics of ferroelectric domain evolution: Theory, finite element implementation, and application to domain wall pinning. *Journal of the Mechanics and Physics of Solids*, 55:280–305, 2007.

[104] C.T. Sun and S. Park. Determination of fracture toughness of piezoceramics under the influence of electric field using Vickers indentation. 213–222, 1995.

[105] X. Sun, Y.J. Su, K.W. Gao, L.Q. Guo, L.J. Qiao, W.Y. Chu, and T.Y Zhang. Surface potential distribution in an indentation-pre-cracked $BaTiO_3$ single crystal. *Journal of the American Ceramic Society*, 94:4299–4304, 2011.

[106] Z. Suo, C.M. Kuo, D.M. Barnett, and J.R. Willis. Fracture mechanics for piezoelectric ceramics. *Journal of the Mechanics and Physics of Solids*, 40:739–765, 1992.

[107] P. Suryanarayana and K. Bhattacharya. Evolution of polarization and space charges in semiconducting ferroelectrics. *Journal of Applied Physics*, 111:034109–034109–11, 2012.

[108] S.M. Sze and K.K. Ng. *Physics of Semiconductor Devices*. Wiley, 2006.

[109] T.H. Hao and Z.Y. Shen A new electric boundary condition of electric fracture mechanics and its applications. *Engineering Fracture Mechanics*, 47:793–802, 1994.

[110] A.G. Tobin and Y.E. Pak. *Effect of electric fields on fracture behavior of PZT ceramics*, 1916:78–86. 1993.

[111] A. Turon, C.G. Davila, P.P. Camanho, and J. Costa. An engineering solution for mesh size effects in the simulation of delamination using cohesive zone models. *Engineering Fracture Mechanics*, 74:1665–1682, 2007.

[112] H. Wang and R.N. Singh. Crack propagation in piezoelectric ceramics: Effects of applied electric fields. *Journal of Applied Physics*, 81:7471–7479, 1997.

[113] J. Wang and C.M. Landis. Effects of in-plane electric fields on the toughening behaviour of ferroelectric ceramics. *Journal of Mechanics of Materials and Structures*, 1:1075–1095, 2006.

[114] J. Wang and Marc Kamlah. Three-dimensional finite element modeling of polarization switching in a ferroelectric single domain with an impermeable notch. *Smart Materials and Structures*, 18:104008, 2009.

[115] J. Wang and T.Y. Zhang. Phase field simulations of polarization switching-induced toughening in ferroelectric ceramics. *Acta Materialia*, 55:2465–2477, 2007.

[116] Y. Watanabe. Theoretical stability of the polarization in a thin semiconducting ferroelectric. *Physical Review B*, 57:789–804, 1998.

[117] Y. Watanabe. Theoretical stability of the polarization in insulating ferroelectric/semiconductor structures. *Journal of Applied Physics*, 83:2179–2193, 1998.

[118] K. Weichert, W. Sigle, P.A. van Aken, J. Jamnik, C. Zhu, R. Amin, T. Acarturk, U. Starke, and J. Maier. Phase boundary propagation in large $LiFePO_4$ single crystals on delithiation. *Journal of the American Chemical Society*, 134:2988–2992, 2012.

[119] K. Weichert, W. Sigle, P.A. van Aken, J. Jamnik, C. Zhu, R. Amin, T. Acartürk, U. Starke, and J. Maier. Phase boundary propagation in large $LiFePO_4$ single crystals on delithiation. *Journal of the American Chemical Society*, 134:2988–2992, 2012.

[120] Y. Xiao and K. Bhattacharya. A continuum theory of deformable, semiconducting ferroelectrics. *Archive for Rational Mechanics and Analysis*, 189:59–95, 2008.

[121] B.X. Xu, D. Schrade, D. Gross, and R. Mueller. Phase field simulation of domain structures in cracked ferroelectrics. *International Journal of Fracture*, 165:163–173, 2010.

[122] X.L. Xu and R.K.N.D. Rajapakse. Analytical solution for an arbitrarily oriented void/crack and fracture of piezoceramics. *Acta Materialia*, 47:1735–1747, 1999.

[123] L. Yang and K. Dayal. Influence of strain on space-charge distribution at ferroelectric thin-film free surfaces. *Acta Materialia*, 60:6457–6463, 2012.

[124] L. Yang and K. Dayal. Microstructure and stray electric fields at surface cracks in ferroelectrics. *International journal of fracture*, 174:17–27, 2012.

[125] T.Y. Zhang, C.F. Qian, and P. Tong. Linear electro-elastic analysis of a cavity or a crack in a piezoelectric material. *International Journal of Solids and Structures*, 35:2121–2149, 1998.

[126] W. Zhang and K. Bhattacharya. A computational model of ferroelectric domains. part i: model formulation and domain switching. *Acta Materialia*, 53:185–198, 2005.